



De la cristallographie exotique à la réflectométrie innovatrice

A. van Der Lee

► To cite this version:

A. van Der Lee. De la cristallographie exotique à la réflectométrie innovatrice. Chimie. Université de montpellier, 2001. tel-01681029

HAL Id: tel-01681029

<https://hal.umontpellier.fr/tel-01681029>

Submitted on 11 Jan 2018

HAL is a multi-disciplinary open access archive for the deposit and dissemination of scientific research documents, whether they are published or not. The documents may come from teaching and research institutions in France or abroad, or from public or private research centers.

L'archive ouverte pluridisciplinaire **HAL**, est destinée au dépôt et à la diffusion de documents scientifiques de niveau recherche, publiés ou non, émanant des établissements d'enseignement et de recherche français ou étrangers, des laboratoires publics ou privés.

UNIVERSITE MONTPELLIER II
Institut Européen des Membranes
UMR CNRS 5635

HABILITATION A DIRIGER DES RECHERCHES

présentée le 2 février 2001

DE LA CRISTALLOGRAPHIE EXOTIQUE A LA REFLECTOMETRIE INNOVATRICE

par

Arie VAN DER LEE
Ingénieur de recherche

JURY

M. J. BOUIX, Professeur, LMI - Université Lyon I	Rapporteur
M. A. GIBAUD, Professeur, LPEC - Université des Sciences du Maine	Rapporteur
M. A. ROUSSET, Professeur, LCMI - Université Toulouse III	Rapporteur
M. S. BANERJEE, Professeur, Institute of Nuclear Physics - Calcutta, Inde	Examinateur
M. R. CORRIU, Professeur, LCMOS - Université Montpellier II	Examinateur
M. L. COT, Professeur, IEM - Université Montpellier II	Examinateur
M. J. DURAND, Directeur de Recherche, IEM - Université Montpellier II	Examinateur

Exposé scientifique de

A. van der Lee

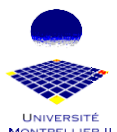
IR-2 au CNRS

En vue de l'obtention du diplôme:

Habilitation à Diriger des Recherches

Novembre 2000

IEM / UMII – Place Eugène Bataillon – Case Courrier 047 – 34095 Montpellier Cedex 5, France
Tél : (33) 04.67.14.91.35 - Fax : (33) 04.67.14.91.19 – avderlee@crit1.univ-montp2.fr



Curriculum Vitae

Personal Info

Nom de famille	Van der Lee
Prénom	Arie
Sexe	Male
Date et lieu de naissance	Le 8 décembre 1964 à Almelo (Pays-Bas)
	Marié, deux enfants
Adresse	18 Rue Bacchus 34170 Castelnau-le-Lez (France)
Adresse de travail	Institut Européen des Membranes UM-II cc047 Place E. Bataillon 34095 Montpellier Cedex 5 (France)
Téléphone, e-mail	00-33-4-67-14-91-35; avderlee@crit1.univ-montp2.fr

Formation

1983-1987	Maîtrise et DEA en Physique Expérimentale de l'Etat Solide ; Laboratorium voor Vaste Stof Fysica, Universiteit van Groningen (Pays-Bas) Sujet: Polarisation de clusters dans $\text{Sr}_{1-x}\text{Ce}_x\text{F}_{2+x}$ Supervisor: H. W. den Hartog
1987-1991	Doctorat (3-1-1992) en Sciences ; Laboratorium voor Anorganische Chimie, Universiteit van Groningen (Pays-Bas) Sujet: Ordre et désordre d'Ag dans des chalcogénures Directeurs de thèse: G. A. Wiegers and C. Haas <i>La thèse a été attribuée le Prix triannuel de Cristallographie par de Koninklijke Nederlandse Chemie Vereniging (Association Néerlandaise Royale de Chimie)</i>

Expérience Professionnelle

1992	Chauffeur de camion dans l'Armée de Terre Néerlandaise
1993-1994	Chercheur associé à l'Institut des Matériaux de Nantes Sujet: Tellurures modulées Groupe: M. Evain
1995	Chercheur associé au Laboratorium voor Kristallografie de l'Universiteit van Amsterdam (Pays-Bas) Sujet: Développement d'un logiciel pour le traitement des données pour des phase modulées Groupe: H. Schenk
1996-	Ingénieur de Recherche (CNRS) au Laboratoire des Matériaux et Procédés Membranaires à Montpellier Sujet: Diffraction de poudres, mono-cristaux, de couches minces ; réflectivité ; méthodologie d'analyse des données de

	réflectivité
--	--------------

Cours, stages (les plus importants)

1990	Diffusion inélastique de neutrons (IRI-Universiteit van Delft)
1993	Structures commensurables et incommensurables (Institute of Physics, Prague)
1996	Initiation à la réflectivité spéculaire (Laboratoire de Cristallographie, Grenoble)
1998	Radioprotection (Lyon)

Enseignement et encadrement

1990-1991	Travaux dirigés en chimie quantique : Universiteit van Groningen
1990-1991	Travaux pratiques en cristallographie et diffraction : Universiteit van Groningen
1989-1991	Travaux pratiques chimie physique : Universiteit van Groningen
1990-1991	Encadrement du travail de DEA R. van de Belt : synthèse et cristallographie des phases AgLnS_2 ($\text{Ln}=\text{Sm - Yb}$) : Laboratorium voor Anorganische Chemie, Universiteit van Groningen
1996-2000	Encadrement de la partie rayons-X du travail de thèse M. Klotz, L. Dalmazio, C. Bouzon, Ph. Baldet, S. Kallus et S. Roualdes
1997-2000	Cours Réflectivité et applications : Ecole Nationale Supérieure de Chimie de Montpellier
2000	Workshop CNRS : «Réflectivité de couches minces en incidence rasante». Organisation et animation
2000	Encadrement d'un étudiant Erasmus J. Sykora (République Tchèque) Diffraction de rayons-X sur plusieurs mono-cristaux et détermination des bruits de fonds en réflectométrie

List of Publications

1988

1. P. Dorenbos, **A. van der Lee**, and H.W. den Hartog: Cluster Polarization in $\text{Sr}_{1-x}\text{Ce}_x\text{F}_{2+x}$; Hopping Transport in Fractal Structures, *Phys. Rev. B* **37**, 10312-10318 (1988)

1989

2. **A. van der Lee** and G.A. Wiegers: Anharmonic Thermal Motion of Ag in AgCrSe_2 : a High-temperature Single Crystal Diffraction Study, *J. Solid State Chem.* **82**, 216-224 (1989)

1990

3. **A. van der Lee**, G.A. Wiegers, R.J. Haange, and J.L. de Boer: Structure of $\text{Ag}_{0.6}\text{NbS}_2$, *Acta Crystallogr. C* **46**, 976-979 (1990)
4. **A. van der Lee** and G.A. Wiegers: Single Crystal X-ray Study of SnTaS_2 at 295 and 425 K, *Mater. Res. Bull.* **25**, 1011-1018 (1990)
5. A. Meetsma, **A. van der Lee**, A.P. Jekel, J.C. van de Grampel, and K. Brandt: Structure of the Tetrabutylammonium salt of 2,4,4,6,6-Pentachloro-1,3,5,2¹,4¹,6¹-triazatriphosphorine 2-Oxide, *Acta Crystallogr. C* **46**, 909-911 (1990)
6. T. Chivers, M. Edwards, P.N. Kapoor, A. Meetsma, **A. van der Lee**, and J.C. van de Grampel: A Novel Coordination Mode for Dithiatetrazocines; Preparation, X-ray Structure and Fluxional Behavior of $[\text{Pt}(\text{PPh}_3)_{1.5}-\text{Ph}_4\text{P}_2\text{N}_4\text{S}_2]_2$, *Inorg. Chem.* **29**, 3068-3069 (1990)
7. T. Chivers, S.S. Kumaravel, A. Meetsma, J.C. van de Grampel, and **A. van der Lee**: Novel Approach to the Synthesis of Ring Systems containing Phosphorus, Nitrogen, and Sulfur or Selenium, *Inorg. Chem.* **29**, 4591-4592 (1990)

1991

8. **A. van der Lee** and G.A. Wiegers: Disorder and Thermal Motion of Ag in $\text{Ag}_{0.6}\text{NbS}_2$ at High Temperatures, *Acta Crystallogr. A* **46**, C306 (1991)
9. **A. van der Lee** and G.A. Wiegers: Disorder and Thermal Motion of Ag in $\text{Ag}_{0.6}\text{NbS}_2$, *Solid State Ionics* **44**, 287-292 (1991)
10. **A. van der Lee**, S. van Smaalen, G.A. Wiegers, and J.L. de Boer: Order-Disorder Transition in Silver Intercalated Niobium Disulfide Compounds. I. Structural Determination of $\text{Ag}_{0.6}\text{NbS}_2$, *Phys. Rev. B* **43**, 9420-9430 (1991)
11. H.J.M. Bouwmeester, **A. van der Lee**, S. van Smaalen, and G.A. Wiegers: Order-Disorder Transition in Silver Intercalated Niobium sulfide Compounds. II. Magnetic and Electrical Properties of Ag_xNbS_2 , *Phys. Rev. B* **43**, 9431-9435 (1991)

1992

12. **A. van der Lee**, R. van de Belt, and G.A. Wiegers: Synthesis and Structures of AgLnS_2 ($\text{Ln}=\text{Sm-Yb}$) compounds, *J. Alloys and Compounds* **178**, 57-70 (1992)
13. **A. van der Lee**, G.A. Wiegers, and C. Haas: Probability Density and Effective One-Particle Potential of Octahedral Ag in the fast Ion Conductor $\text{Ag}_{0.39}\text{TiS}_2$, *Solid State Ionics* **50**, 147-158 (1992)
14. T. Chivers, M. Edwards, A. Meetsma, J.C. van de Grampel, and **A. van der Lee**: Preparation and ³¹P NMR Investigations of 1,5-Diphophadi-thiatetrazocines; X-ray Structure of $\text{Pt}(\text{PPh}_3)_2(1,5-\text{Ph}_4\text{P}_2\text{N}_4\text{S}_2).\text{CH}_2\text{Cl}_2$, *Inorg. Chem.* **31**, 2156-2161 (1992)
15. T. Chivers, M. Edwards, P.N. Kapoor, A. Meetsma, J.C. van de Grampel, and **A. van der Lee**: Metal Complexes of Dithiatetrazocines, *Phosphorus, Sulfur, and Silicon* **65**, 135-138 (1992)

1993

16. **A. van der Lee**, F. Boucher, M. Evain, and R. Brec: Temperature Dependence of the Silver Distribution in $\text{Ag}_2\text{MnP}_2\text{S}_6$ by Single Crystal X-ray Diffraction. *Z. Kristallogr.* **203**, 247-264 (1993)
17. **A. van der Lee** and J.L. de Boer: Redetermination of the Structure of Hessite, $\text{Ag}_2\text{Te-III}$, *Acta Crystallogr. C* **46**, 1444-1446 (1993)

1994

18. **A. van der Lee**, M. Evain, L. Monconduit, R. Brec, J. Rouxel, and V. Petříček: The Interface-modulated Structure of $\text{TaSi}_{0.360}\text{Te}_2$, *Acta Crystallogr. B* **50**, 119-128 (1994)
19. **A. van der Lee**, M. Evain, L. Monconduit, R. Brec, and S. van Smaalen: A Superspace Approach to the Modulated Structures of $MA_x\text{Te}_2$ ($M=\text{Si, Ge, A=Ta, Nb, } 1/3 \leq x \leq 1/2$), exemplified by $\text{NbGe}_{3/7}\text{Te}_2$, *J. Phys.: Cond. Matter* **6**, 933-944 (1994)
20. **A. van der Lee**, M. Evain, M. Mansuetto, L. Monconduit, R. Brec, and J. Rouxel: Determination of the Commensurately Modulated Structure of $\text{NbGe}_{2/5}\text{Te}_2$ from Twinned-Crystal Data. *J. Solid State Chem.* **111**, 75-82 (1994)
21. **A. van der Lee**, M. Evain, L. Monconduit, R. Brec, and V. Petříček: 11-fold Superstructure of $\text{TaGe}_{4/11}\text{Te}_2$; a Novel Response to Charge Transfer in the $MA_x\text{Te}_2$ Series ($M=\text{Si, Ge, A=Ta, Nb, } 1/3 \leq x \leq 1/2$). *Inorg. Chem.* **33**, 3032-3037 (1994)
22. M. Evain, L. Monconduit, **A. van der Lee**, R. Brec, and E. Canadell: Synthesis and Electronic Structure of Ta_3SiTe_6 . *New J. Chem.* **18**, 215-222 (1994)
23. M. Evain, **A. van der Lee**, L. Monconduit, and V. Petříček: Modulated Structure of $\text{TaSi}_{0.41}\text{Te}_2$; Sandwich stacking in the $MA_x\text{Te}_2$ ($M=\text{Si, Ge; A=Ta, Nb, } 1/3 \leq x \leq 1/2$) Series. *Chem. Mater.* **6**, 1776-1783 (1994)
24. R. Roesky, A. Meerschaut, **A. van der Lee**, and J. Rouxel: Structural Study of $(\text{Nb}_{1-x}\text{La}_x\text{S})\text{NbS}_2$ ($x \approx 0.3$) - The first "Self-Misfit" Compound. *Mater. Res. Bull.* **29**, 1149-1155 (1994)

1995

25. V. Petříček, **A. van der Lee**, and M. Evain: On the Use of Crenel Functions for Occupationally Modulated Structures. *Acta Crystallogr. A* **51**, 529-535 (1995)
26. **A. van der Lee** and M. Evain. The Interface-Modulated Structures of the $MA_x\text{Te}_2$ ($M=\text{Si, Ge, A=Ta, Nb, } 1/3 \leq x \leq 1/2$) Phases. Aperiodic '94; G. Chapuis, W. Paciorek, Eds.; World Scientific Publishing; pp. 440-444 (1995)
27. S.H. Elder, **A. van der Lee**, R. Brec, and E. Canadell: KNiPS_4 ; a New Thiophosphate with One and Two-Dimensional Structural Arrangements. *J. Solid State Chem.* **116**, 107-112 (1995)

1996

28. L. Cariot, A. Lafond, **A. van der Lee**, and A. Meerschaut: Incommensurate Structure of a Lillianite-type Samarium Chromium Sulfide. *J. Solid State Chem.* **127**, 295-301 (1996).

1997

29. **A. van der Lee**, L.M. Hoistad, M. Evain, B. Foran, and S. Lee: Resolution of the 66-fold Superstructure of $\text{Dy}_{11}\text{Se}_{20}$ by Single-Crystal X-ray Diffraction and Second-moment Scaled Hückel Calculations. *Chem. Mater.* **9**, 218-226 (1997).
30. C. Vallée, A. Goulet, A. Granier, C. Marlière, **A. van der Lee**, J. Durand, P. Raynaud, and J.P. Deville: Characterisation of PECVD SiOCH Films by Ellipsometry and X-ray Reflectometry. *Le Vide* **53**, 326-329 (1997).

1999

31. M. Klotz, A. Ayral, **A. van der Lee**, C. Guizard, C. Menager, and V. Cabuil: Synthesis and Texture of Mesophase Templatied Silica Layers Seeded with Nanoparticles. *Mat. Res. Soc. Symp. Proc.* **576**, 247-253 (1999).
32. C. Boissière, **A. van der Lee**, A. El Mansouri, A. Larbot, and E. Prouzet: A double step synthesis of mesoporous micrometric spherical MSU-X silica particles. *Chem. Comm.* **20**, 2047-2048 (1999).
33. S. Roualdes, **A. van der Lee**, R. Berjoan, J. Sanchez, and J. Durand: Gas Separation properties of Plasma Polymerized Membranes from Organosilicon Monomers. *AICHE J.* **45**, 1566-1575 (1999).
34. **A. van der Lee**, J. Durand, D. Cot, and L. Vázquez: Study of the Growth Mechanism of CVD Silicon Films on Silica by X-ray Reflectivity, Atomic Force Microscopy, and Scanning Electron Microscopy. *J. Phys. IV France* **9**-Pr8 157-164 (1999).
35. S. Roualdes, N. Hovnanian, **A. van der Lee**, J. Sanchez, and J. Durand: Hybrid Plasma Polymerized Membranes from Organosilicon Precursors for Gas Separation. *J. Phys. IV France* **9**-Pr8 1147-1154 (1999).
36. S. Roualdes, N. Hovnanian, **A. van der Lee**, R. Berjoan, and J. Durand: Organic/Inorganic Thin Films Deposited from Diethoxydimethylsilane by Plasma Enhanced Chemical Vapor Deposition. *J. Non-Cryst. Sol.* **248**, 235-246 (1999).
37. B. Caussat, J. P. Couderc, L. Vázquez, A. Figueras, **A. van der Lee**, J. Durand, A. Dollet, R. Berjoan, E. Scheid, P. temple, S. Schamm, B. de Mauduit, V. Paillard, A. Vila, and J. R. Morante: Correlations entre conditions d'élaboration et microstructure de dépôts LPCVD. Partie 3: Dépôt de silicium pur à partir de silane: résultats expérimentaux. (French). *Entropie* **22**, 2-13 (1999).
38. **A. van der Lee**: Het fasaprobleem in de röntgen- en neutronenreflectometrie (Dutch), *Nieuwsblad voor Kristallografen* **21**, 11-15 (1999).

2000

39. **A. van der Lee**: Experimental Feasibility of Phaseless Inverse Scattering Methods for Specular Reflectivity. *Eur. Phys. J. B* **13**, 755-763 (2000).
40. **A. van der Lee**: Practical Aspects of Inverse Scattering Methods Applied to Specular Reflectivity Data. *Physica B* **283**, 273-277 (2000).
41. **A. van der Lee**: Grazing Incidence Specular Reflectivity: Theory, Experiment, and Applications. *Solid State Sciences* **2**, 257-278 (2000).
42. C. Vallée, A. Goulet, A. Granier, J.P. Deville, **A. van der Lee**, J. Durand, and C. Marlière: Structural Changes in Thin films Deposited in O₂/TEOS Plasma: the Transition Between the Organic and Inorganic phase. Accepted *J. Non-Cryst. Sol.* (2000).
43. M. Klotz, P.-A. Albouy, A. Ayral, C. Ménager, D. Gross, **A. van der Lee**, F. Babonneau, V. Cabuil, and C. Guizard. The True Structure of Hexagonal Mesophase-Templated Silica films as Revealed by X-ray scattering: Effects of Thermal Treatments and of Nanoparticle Seeding. *Chem. Mater.* **12**, 1721-1728 (2000).
44. C. Boissière, A. Larbot, **A. van der Lee**, P.J. Kooyman, and E. Prouzet: A New Synthesis of Mesoporous MSU-X Silica Controlled by a Two-Step Pathway. Accepted *Chem. Mater.* (2000).
45. **A. van der Lee**, S. Roualdes, R. Berjoan, and J. Durand: Mass Density Determination of Thin Organosilicon Films by X-ray Reflectometry. Submitted to *Appl. Surf. Sci.* (2000).

1. Présentation générale

Bien que le document de synthèse soit un récit de la recherche après la soutenance de thèse, il est incontournable de débuter ce texte avant cette date, puisqu'il y a des liens direct entre la période que j'ai effectué en tant que thésard au *Laboratorium voor Anorganische Chemie* (Laboratoire de Chimie Inorganique) à Groningen aux Pays-Bas et la période post-doc à l'*Institut des Matériaux de Nantes* (IMN, actuellement Institut des Matériaux Jean Rouxel). En effet, la démarche scientifique que j'emploie actuellement à l'*Institut Européen des Membranes* (IMM) à Montpellier pour de nouveaux projets est toujours dictée par cette période d'apprentissage à Groningen.

Une autre raison pour faire débuter ce document dans la période néerlandaise est que mon premier encadrement d'un 'jeune chercheur' s'y est déroulé pendant ma période de thèse. Contrairement à la situation en France, il est coutume aux Pays-Bas que chaque thésard encadre au moins un étudiant de type 'DEA'.

Ce document se concentre par conséquent sur trois axes : la période néerlandaise (1987-1991) sera abordé en premier, brièvement car elle est proprement dite hors la période qui doit être couverte par le diplôme HDR, mais elle est importante pour des raisons indiquées ci-dessus. La deuxième période qui sera décrite est la période à Nantes (1993-1994) et la troisième celle à Montpellier (1996-2000).

Le fil conducteur qui traverse toute la période du début de la thèse jusqu'aux travaux actuels est l'application des méthodes d'analyse non-standard pour les problèmes rencontrés dans le domaine de la diffusion de rayons-X, quel qu'il soit la diffraction ou la réflectivité. Mon activité dans ces types d'analyse a débuté dans le groupe de cristallographie 'exotique' (parole d'après J. L. de Boer). Pendant les dernières années cette façon de travailler a la tendance de se diriger vers le développement de nouvelles méthodes.

Le domaine de diffraction de rayons-X connaît déjà une longue histoire qui date des années dix et vingt de la dernière siècle lorsque Bragg and Von Laue ont construit les fondements de la diffractométrie expérimentale et théorique. Depuis cette époque les avancements n'ont pas cessé ; au contraire, il n'est pas prétentieux de postuler que la diffraction de rayons-X peut être située parmi les techniques de l'analyse les plus quantitatives pour l'état solide. Elle permet de quantifier - avec facilité - des mesures (liaisons entre atomes et ions) de l'ordre d'un angström et avec une précision bien au-dessous d'un angström. La compréhension des propriétés physiques et chimiques de la matière cristalline n'est jamais possible sans une connaissance de la structure atomique, déterminé par l'outil par excellence : la diffraction de rayons-X. Malgré la maturité du domaine déjà atteinte dans les années soixante de la dernière siècle et grâce à la progression sur le plan technique, on a pu utiliser la diffraction de rayons-X pour observer et décrire des phénomènes qui dépassent la description classique de l'interaction de rayons-X avec la matière cristalline.

Groningen : Ordre et désordre d'argent dans les chalcogénures

Le premier phénomène qui a joué un rôle important pour les travaux de ma thèse et qui a initié mon départ à Nantes est la non-harmonicité de la vibration d'un atome dans un réseau cristallin. Bien que cette vibration soit correctement décrite par le mouvement d'un oscillateur harmonique pour la plupart d'atomes, il existent des atomes dont la vibration est notoirement non-harmonique, comme l'argent et le cuivre. En effet, ces atomes ont également la tendance de se désordonner quand la température baisse, ce qui peut provoquer des transitions d'une phase désordonnée à une phase ordonnée. Dans la phase désordonnée le sous-réseau de l'argent ou du cuivre peuvent former à haute température des phases quasi-liquides au milieu d'un réseau condensé. On parle dans ces cas des conducteurs ioniques. Ces phénomènes peuvent être observés et suivis par diffraction de rayons-X, normalement en fonction de la température. Il est nécessaire d'adapter le formalisme existant de la vibration harmonique de l'atome afin de modéliser correctement les intensités observées pour de tels systèmes. Il s'avère nécessaire de différencier entre désordre statique et désordre dynamique dans ces composés. C'est autour de ces thèmes d'ordre et désordre que sera présenté la première partie de cette synthèse. C'est également ici que sera abordé le travail de R. van de Belt, le premier étudiant faisant de la recherche dans le cadre de ma thèse.

Nantes : structures modulées

Le deuxième axe de ma recherche a également commencé à Groningen, lors de la résolution structurale de la phase ordonnée de $\text{Ag}_{0.6}\text{NbS}_2$. Il s'est avéré que la période de cette phase était incommensurable avec la période de la phase désordonnée. La résolution de l'arrangement ordonné du sous-réseau d'Ag a nécessité l'utilisation des méthodes d'analyse non-standard. Mon déplacement vers Nantes était stimulé par cette connaissance des méthodes avancées pour la résolution des structures 'difficiles'. En effet, deux groupes de recherche à l'IMN venaient de trouver des phases (in)commensurablement modulées, les phases dites 'misfit' dans le groupe d'A. Meerschaut et toute une série de tellurures ($MA_x\text{Te}_2$, $M=\text{Nb}, \text{Ta}$; $A=\text{Si}, \text{Ge}$; $1/3 \leq x \leq 1/2$) dans le groupe de M. Evain. C'est dans le groupe du dernier que j'ai effectué ma période 'post-doc'. Les résolutions structurales ont été encadré dans le travail d'une thésarde, L. Monconduit, qui a fait toutes les synthèses et a pris pour son compte toute une série d'analyses et analyses structurales. Il est à noter que les années 1992-1993 marquent également le début d'une période dans laquelle l'IMN a vu sortir de nombreuses publications concernant les affinements structurales non-harmoniques ou modulées. Cette période ne s'est d'ailleurs pas achevée.

Montpellier : reflectométrie innovatrice

La mutation vers Montpellier, après un court intermède au *Laboratorium voor Kristallografie* (Laboratoire de Cristallographie) à Amsterdam, était dictée par l'expérience acquise à Groningen et Nantes. Les tâches au *Laboratoire des Matériaux et Procédés Membranaires* (LMPM, actuellement IMM) se sont diversifiées : les résolutions structurales sur monocristaux se sont fortement diminuées, tandis que la diffraction sur poudres et surtout la réflectométrie en incidence rasante de couches minces dominent en ce moment ma recherche. C'est surtout la réflectométrie qui donne de nouvelles voies pour la recherche. Bien que la réflectométrie de rayons-X de couches minces soit connue depuis une cinquantaine d'années, sa méthodologie – c'est à dire l'exploitation des données afin d'obtenir un modèle compatible aux données expérimentales – est sous-développé par rapport à ce qui est connu dans le domaine de la cristallographie. La réflectométrie de rayons-X peut être considérée comme une technique vraiment unidimensionnelle, contrairement à la diffraction sur monocristaux, qui est une technique vraiment trois-dimensionnelle, tandis que la diffraction de poudres est également intrinsèquement trois-dimensionnelle, mais exploitée uni-dimensionnellement. En dépit de sa simplicité apparente, l'exploitation des données de réflectométrie n'est évident qu'en cas très simple. Il est autour de ce problème que s'est dirigée ma recherche à Montpellier : comment peut-on faciliter l'analyse des données et surtout comment peut-on extraire des enregistrements le maximum d'information sur le système sous étude ?

2. Principaux résultats

Les résultats sont parus dans des revues internationales dans la période 1988-2000. Les principal coauteur de la période néerlandaise est G. A. Wiegers, directeur de thèse. Ceux de la période nantaise sont M. Evain et L. Monconduit. La période montPELLIÉRaine ne connaît pas de coauteur principal, dû à la nature de ma fonction au sein du laboratoire.

2.1. Groningen : Ordre et désordre d'argent dans les chalcogénures

Je souhaite aborder ici surtout l'étude qui a initié les futurs travaux à l'IMN à Nantes, celle sur la détermination structurale de la phase basse-température d' $\text{Ag}_{0.6}\text{NbS}_2$. Ensuite l'étude menée avec l'étudiant R. van de Belt sera brièvement éclairée.

2.1.1 $\text{Ag}_{0.6}\text{NbS}_2$: une étude structurale entre 100 K et 695 K

L'étude menée ici succède une longue série d'études dans le Laboratorium voor Anorganische Chemie sur les phases d'intercalation. Cette structure s'est avérée très intéressante à la fois à haute température, grâce à une mobilité très élevée des ions d'Ag, mais également à basse température quand ces ions se rangent de façon

incommensurable sur un réseau de rayon (Van der Lee *et al.* (1990, 1991a,b), Bouwmeester *et al.* (1991)) . La Figure x montre des clichés de diffraction électronique à différentes températures. On s'aperçoit qu'en baissant la température les halos d'intensité diffuse se condensent à 100 K en satellites bien définis autour des taches principales. Les positions des satellites ne peuvent indexées par trois nombres entiers, comme est requis par la cristallographie classique. Il est en revanche nécessaire d'employer un système d'indexation de 5 nombres entiers selon le formalisme développé par De Wolff (1974), Janner et Jansen (1977). La cristallographie de ce système se décrit ainsi dans une espace (3+2)-dimensionnelle. Les résultats (3+2)-dimensionnels se laissent simplement traduire dans des arrangements d'Ag sur le réseau de rayon (Fig. X). Ceci semble à première vue très désordonnée, mais correspond en effet à un arrangement parfaitement ordonné, comme peut être prouvé par une transformation de Fourier de cet image. En montant la température l'argent s'arrange au-delà de 135 K aléatoirement sur le sites du réseau de rayon. En montant encore plus, le sous réseau d'Ag à la tendance de se liquéfier, comme montre le map de la densité électronique à 595 K (Fig. X).

2.1.2 Les structures des composées AgLnS_2 ($\text{Ln}=\text{Sm} - \text{Yb}$)

Bien que la résolution structurale de ces composées aie suivi des méthodes classiques, cette étude mérite d'être mentionné ici, car elle est le résultat d'une longue série de synthèses et analyses par R. van de Belt faisant ses 9 mois de travaux expérimentaux au sein d'un groupe de recherche à la fin de la première phase de la formation universitaire néerlandaise. L'étude a été initiée car il a été rapporté que ces phases devraient être des conducteurs ioniques à haute température. La structure était deviné a partir des diagrammes de poudres. Van de Belt a réussi de faire croître des monocristaux en utilisant deux méthodes différentes (Van der Lee *et al.* (1992)).

L'affinement structural s'est avéré très fastidieux du à une distorsion monoclinaire par rapport à une maille quadratique. En effet, la maille unitaire est géométriquement quadratique, mais son contenu atomique est monoclinaire. Après avoir trouvé une structure approximative par des méthodes directes, l'affinement structural a échoué de converger. Une inspection détaillée de la liste des facteurs de structure a révélé que les réflexions qui doivent être absentes par raisons de symétrie dans la structure parentale quadratique, mais qui peuvent être présente dans la maille réciproque monoclinaire, étaient systématiquement calculées trop fortes. L'affinement n'a pu converger qu'après inclusion de toutes les réflexions, même celles avec une intensité négligeable. Ceci montre que le coutume pratique de supprimer les réflexions de faible intensité dans les affinements structuraux pourrait aboutir à une structure incorrecte.

Les atomes d'Ag se trouvent dans un environnement octaédrique très tordu. En effet, vu des distances, on peut considérer qu'ils se trouvent dans un environnement linéaire de S. Les facteurs de Debye-Waller sont très élevés (de l'ordre de 10 Å). La suggestion que les facteurs de Debye-Waller élevés pour les ions d¹⁰ dans des environnements octaédriques peuvent être attribués à un effet de Jahn-Teller de second ordre, donnant un désordre statique autour du site central et par conséquent un facteur de Debye-Waller apparent qui est élevé (Lee *et al.* (1988)), ne peut être justifiée à base de ces résultats. Dans la structure actuelle l'environnement d'Ag est presque linéaire, donc il n'y a pas un éventuel effet de Jahn-Teller, mais les facteurs 'thermiques' sont quand même élevés. On a pu montrer que les structures ne sont pas de conducteurs ioniques.

2.2. Nantes : structures modulées

La période nantaise est marquée par des activités intensives sur de difficiles structures modulées. A part de la collaboration étroite avec L. Monconduit et son directeur de thèse M. Evain, des contacts intensifs avec V. Petricek se sont établis qui ont culminé dans une visite d'un mois à l'*Institute of Physics* à Prague. Quelques études ont été faites avec R. Brec et S. Elder d'un côté et A. Lafond et A. Meerschaut de l'autre côté.

2.2.1. Modulations commensurables et incommensurables dans les composées MA_xTe_2 ($M=Nb, Ta ; A=Si, Ge ; 1/3 \leq x \leq 1/2$)

Les études sur les phases MA_xTe_2 ($M=Nb, Ta ; A=Si, Ge ; 1/3 \leq x \leq 1/2$) ont bien montré l'intérêt d'une approche (3+1)dimensionnelle pour unifier la description structurale de (presque) toute une série de composées (Van der Lee *et al.* (1994a,b,c), Evain *et al.* (1994a,b)). Un autre avantage de l'approche (3+1)D est davantage numérique : le nombre des paramètres dans l'affinement est réduit et les corrélations entre les paramètres concernant les atomes de même type, mais dans une maille unitaire différente sont réduites. L'affinement de cette série de ces composés a néanmoins montré que des corrélations fortes, notamment pour les paramètres des modulations déplacives, peuvent exister qui sont liées à l'existence de la modulation occupationnelle. La raison est que la fonction déplacive n'est pas proprement définie quand la fonction occupationnelle prend la valeur 0.00 ou est proche de zéro. Mathématiquement cela veut dire que les harmoniques distinctes de la fonction displacive ne sont plus orthogonales. La remédie est la ré-orthogonalisation de ces harmoniques. Ces observations ont conduit à une technique d'affinement améliorée pour des structures possédant une modulation occupationnelle (Pétrisse *et al.*, 1995). La technique en consiste en utilisant des fonctions de créneau pour la modulation occupationnelle qui prennent uniquement les valeurs 1.00 ou 0.00. L'amplitude de la fonction dispacive correspondante est ensuite supprimée quand elle n'est pas proche de l'orthogonalité par rapport aux fonctions déjà sélectionnées. Les fonctions résultantes sont finalement orthogonalisées. Ceci est très efficace en réduisant les corrélations. Cette méthode a aidé à trouver et affiner les structures de la série MA_xTe_2 .

L'originalité des phases MA_xTe_2 est l'environnement carré planair de l'atome A et bien évidemment la ségrégation unidimensionnelle des unités MTe_2 , conduisant à une modulation occupationnelle/déplacive des atomes de la maille unitaire. La stabilité de l'atome A dans son environnement carré planair peut être expliquée par des liaisons covalentes A -Te, complétées par quatre interactions attractives A - M (Boucher *et al.* 1996). Ces dernières interactions sont également responsables pour la stabilisation des cations solitaires M dans une coordinence prismatique de Te pour les phases $x < 1/2$.

Fig. X montre une couche de la structure de $MA_{1/3}Te_2$. Elle montre les atomes A dans leur environnement carré planair de Te et des paires formées des atomes A - A dans un environnement prismatique de Te. Finalement il y a des atomes A solitaires dans des environnements prismatiques formant des rubans perpendiculairement à la direction de la modulation. Il est à noter que c'est uniquement l'autre membre terminal,

$MA_{1/3}Te_2$, qui ne connaît pas des rubans d'atomes solitaires. Les couches de tous les autres membres de la série peuvent être comprises comme des combinaisons d'un certain nombre de modules $MA_{1/3}Te_2$ plus un certain nombre de modules de $MA_{1/2}Te_2$. Ceci est schématiquement montré dans la Fig. X. On peut ainsi former un nombre infini de structures modulées. On a pu trouver les phases $Nb_{1/3}SiTe_2$, $Nb_{1/3}GeTe_2$, $Ta_{1/3}SiTe_2$, $Nb_{2/5}GeTe_2$, $Nb_{3/7}GeTe_2$, $Ta_{4/11}GeTe_2$, $Ta_{0.360}SiTe_2$, and $Ta_{0.41}SiTe_2$, and $NbSi_{1/2}Te_2$.

Un deuxième aspect structural qui mérite d'être abordé brièvement est le polytypisme (Evain *et al.* (1994b)). Malgré le fait que les couches sont simplement bâties des modules $MA_{1/3}Te_2$ et $MA_{1/2}Te_2$, les structures connaissent un facteur complice : l'empilement mutuel des couches. L'empilement varie d'un composé à un autre, de (AA)(BB) à (AA)(BB)(CC). Ceci fait qu'il n'y a pas un groupe de superespace parental pour toutes les structures de la série. Il est vrai que l'approche multidimensionnelle a aidé à résoudre et affiner les structures, mais il n'était pas possible d'unifier toute la famille.

2.2.2. Résolution structurale de la 66-multiple surstructure de $DySe_{1.84}$ par diffraction de rayons-X et calculs de bandes électroniques

Cette étude a été initiée suite à la découverte de quelques chalcogénures de terres rares qui posséderaient des ondes de densité de charge dues aux états électroniques des chalcogénures, contrairement à la situation rencontrée habituellement, quand elles sont associées aux états électroniques des éléments de transition, comme Ta et Mo. Les distorsions structurales dues à l'onde de densité de charge ont été étudiées par diffraction de rayons-X sur un monocristal. Des calculs de structures de bande électronique – en collaboration étroite avec S. Lee et B. Foran de *Michigan State University* – ont ensuite aidé à rationaliser les structures trouvées par rayons-X (Van der Lee *et al.* (1997)).

La structure moyenne consiste en plans d'atomes de Se sur un réseau carré, alterné par des bicouches de DySe de type NaCl ; les plans de Se sont partiellement occupés. Les clichés de diffraction ont montrées que la structure modulée est vraisemblablement incommensurable par rapport à une maille unitaire qui est assez petite. La surstructure peut être en bonne approximation décrite dans 66 mailles unitaires (**3a** x **11b** x **2c**). Tandis que la résolution structurale et ensuite l'affinement des paramètres structuraux ont été effectués selon une approche (3+2)D, la visualisation des résultats a été faite dans cette grande maille. Un problème courant de ce type d'affinements pour des structures qui possèdent une modulation d'occupation de site est que les calculs aboutissent souvent à plusieurs solutions pour la répartition de l'atome sur les sites disponibles. Ceci était le cas pour la structure de $TaGe_{4/11}Te_2$ (Van der Lee *et al.* (1994)) et est encore plus marquant pour $DySe_{1.84}$. Quatre modèles ont émergé qui donnaient des facteurs de confiance comparables (Fig. X). On s'aperçoit que la modulation d'occupation de site est accompagnée d'une très forte modulation déplacive des atomes de Se. Ceci conduit à la formation des pairs Se-Se (distance de liaison de l'ordre de 2.4 angstrom). Une analyse plus détaillée de la structure montre que la modulation déplacive de la terre rare est fortement corrélée aux modulations déplacive et occupationnelles de l'anion dans le plan partiellement occupé. Un de quatre modèles (III) peut être exclu parce qu'il donne des distances Se-Se qui sont trop courtes. Les calculs de bandes et d'énergie ont ensuite démontré que le modèle II possède l'énergie la plus basse, mais qu'ils existent encore deux autres modèles avec

une énergie encore un petit peu plus basse. Ces modèles peuvent être interprétés comme soit une combinaison de modèle I et II, soit une extension de I et II.

Il est clair que les données cristallographiques toutes seules ne suffisent pas pour différencier les modèles différents, mais que d'autres moyens peuvent compléter l'étude d'une telle structure difficile.

2.3. Montpellier : réflectométrie innovatrice

Ma recherche à Montpellier s'est manifestée surtout autour de la réflectométrie. D'autres résultats issus de la diffraction de poudres sont parus dans la littérature suite à des collaborations avec différents groupes dans ce laboratoire (C. Guizard, A. Julbe, A. Ayrat, E. Prouzet). J'ai encadré la partie diffraction et réflectivité de rayons-X du travail de thèse de plusieurs étudiants dont doivent être nommés M. Klotz, L. Dalmazio, C. Bouzon, Ph. Baldet, S. Kallus et S. Roualdes. Le travail d'un étudiant stagiaire Erasmus J. Sykora, que j'ai eu le plaisir d'encadrer en 2000, mérite d'être mentionné à part : il va conduire à une publication dans une revue internationale.

La première étude montre comment et avec quelle précision la réflectométrie permet de déterminer la densité massique d'une couche d'une composition partiellement inconnue. Ensuite il est démontré que des anciennes méthodes issues de l'optique peuvent être très utiles en réflectométrie pour déterminer un profil de densité. Finalement les perspectives pour de futures études sont discutées.

2.3.1 Détermination de la densité massique des couches hybrides de composition partiellement inconnue

Cette étude est le résultat du travail de thèse de S. Roualdes et les problèmes rencontrés avec la détermination de la densité massique des couches hybrides de composition partiellement inconnue (Van der Lee *et al.* (2000a)). Ce paramètre est très important pour la caractérisation microstructurale des couches minces déposées par des procédés CVD (Dépôt chimique en phase vapeur) en fonction des conditions de plasma. Ceci était un des sujets de la thèse de S. Roualdes.

La réflectométrie de rayons-X permet de déterminer la densité électronique d'une couche mince. On peut ainsi calculer la densité massique à la condition que l'on connaît la composition chimique de la couche. Ceci n'est en général pas le cas pour des couches déposées par CVD. On sait normalement quels atomes sont déposés mais on ne connaît pas exactement leur proportion.

Le but de l'étude était de voir quelle information pourrait être déduite d'une courbe de réflectivité si la composition n'était que partiellement connue et si cette information serait encore utilisable. Autrement dit : il fallait déterminer les variations de densité massique et de composition qui donnent lieu à exactement la même courbe de réflectivité. Si ces variations sont relativement petites, l'information est utile.

L'approche choisie est de pas fitter des paramètres comme densité massique et composition atomique, mais plutôt l'indice complexe de réfraction. La partie réelle de l'indice est directement reliée à la densité électronique, tandis que la partie imaginaire permet de calculer le coefficient linéaire d'absorption. On peut ensuite dériver une relation entre le rapport de la partie réelle et la composition atomique. Les couches sont constituées de Si, C, O, and H. La proportion de H est fixé à 1.00, le nombre d'hydrogènes est estimé à entre 2 et 3 fois le nombre de carbon. En faisant varier la concentration d'O, on peut ensuite calculer la concentration de C de telle façon que la relation mentionnée ci-dessous est respectée. La connaissance des compositions permet de calculer l'intervalle des densités massiques qui donnent un fit identique aux données expérimentales. Les concentrations C et O ont été comparées avec les concentrations obtenues par spectroscopie rayons-X de photo-électrons. L'accord entre ces valeurs est bon, sauf pour les conditions les plus dures. La Fig. X montre ces concentrations C et O et l'intervalle de densité massique. On s'aperçoit que l'intervalle est assez petit ce qui veut dire que la réflectométrie de rayons-X permet de déterminer des densité massique même si la composition de la couche est mal connue.

2.3.2 Faisabilité expérimentale des méthodes de diffusion inverse sans phases pour la réflectométrie

Le problème commun de la diffraction et de la réflectométrie (Van der Lee (2000a)) est bien évidemment le manque des phases des ondes réfléchies. La connaissance de la phase appartenant à chaque intensité est indispensable afin de pouvoir reconstituer la densité électronique du système sous étude. Pour la diffraction la densité électronique d'un cristal peut être traduite en termes d'une répartition tridimensionnelle d'atomes dans la maille unitaire ; en revanche pour la réflectométrie il s'agit d'une densité électronique unidimensionnelle perpendiculairement à une surface ou interface.

L'approche la plus commode pour trouver les phases est celle de ‘trial-and-error’ (essai-et-faute) combinée avec des affinements moindres-carrées non-linéaires. Elle est en général assez fastidieuse sauf pour des cas très simples. En cristallographie on dispose depuis une trentaine d'années des méthodes extrêmement puissants (les fameux méthodes directes) pour dépasser l'étape de trial-and-error.

Il y a deux raisons fondamentales pour lesquelles on ne peut pas transmettre à la réflectométrie les méthodes développées en cristallographie pour trouver la densité électronique. La première raison est qu'un cristal est considéré comme infiniment grand, tandis qu'un système substrat-couche mince est fondamentalement semi-infini. Ceci se traduit en expérience par le fait que l'espace réciproque d'un cristal contient des taches de diffraction bien séparées, autrement dit par une distribution d'intensité discontinue. De l'autre côté, la distribution d'intensité réfléchie enregistrée par une expérience de réflectométrie est continu. C'est pour cette raison que les fameux méthodes directes de la cristallographie pour trouver les phases ne peuvent être appliquées en réflectométrie. La deuxième raison pour l'incompatibilité des méthodes en cristallographie et celles en réflectométrie est que l'approximation de Born (diffusion simple) n'est pas valable pour le régime des petits angles, proche de l'angle critique, là où les diffusions multiples sont très importantes. Cela veut dire que, une fois les phases trouvées, la densité électronique d'une couche mince ne peut être calculée – comme est le cas

pour la diffraction - par une simple transformation de Fourier inverse. Lié à ce problème est le fait que les phénomènes de réfraction aux interfaces jouent un rôle important proche de l'angle critique.

Les deux problèmes esquissés ci-dessus ont été résolus en théorie, le deuxième, nommé le problème inverse de diffusion, il y a déjà une quarantaine d'années. Klibanov and Sacks d'un côté (1992) et Clinton d'autre côté (1993) ont proposé une solution pour le premier problème. Elle est basé sur une méthode ancienne issue de l'optique : les relations de dispersion ou relations Kramer-Kronig. Ces relations relient la partie réelle et imaginaire d'une fonction de susceptibilité dont la fonction de réponse est causale. Traduit en termes de réflectométrie ceci veut dire que l'intensité mesurée prend la place de la susceptibilité et la fonction de réponse est remplacée par la densité électronique. La densité électronique est strictement zéro hors du système et elle est par conséquent causale. Il est facile à montrer que les relations Kramers-Kronig peuvent être transformées de telle façon qu'elles relient l'amplitude à la phase, appartenant à cette amplitude. L'amplitude, quant à elle, est directement reliée à l'intensité mesurée. En mesurant un jeu d'intensités complet on pourrait en principe aboutir au jeu de phases correspondant au moyen des relations de Kramers-Kronig et par conséquent à la densité électronique au moyen de la solution du problème inverse. Malheureusement il y a une complication, qui trouve son origine dans la théorie des fonctions complexes. Cette théorie est utilisée pour dériver les relations de Kramers-Kronig. La complication pose des contraintes sur les jeux d'intensités et phases qui peuvent être correctement reliés par les relations de Kramers-Kronig. En gros, ceci implique que pas n'importe quel profil de densité peut être trouvé par cette méthode, mais uniquement certaines classes de profils.

Je me suis assigné un triple but après avoir eu connaissance des publications de Klibanov and Sacks et Clinton et après avoir vérifié que ces théories n'étaient pas encore validées par une expérience depuis lors. Je voulais d'abord tester la faisabilité des méthodes en utilisant des données expérimentales. Beaucoup de théories en physique mathématique sont mal-posées ; ceci veut dire qu'elles sont intrinsèquement instables contre la propagation d'erreurs expérimentales ou même numériques. Il est coutume en physique mathématique de faire des expériences numériques en simulant des systèmes réels pour valider les théories dérivées. Ces 'expériences' ne sont pas toujours de réalité, surtout concernant la distribution d'erreurs expérimentales. La validation ultime d'une théorie est l'expérience de laboratoire. Deuxièmement il était intéressant de voir pour quels profils de densité électronique les relations de Kramers-Kronig étaient utilisable. Clinton en avait déjà dérivé en utilisant l'approximation de Born, mais il était plus opportun d'en trouver en utilisant la théorie dynamique, c'est à dire en tenant compte des multiples réflexions et de la réfraction. Finalement j'envisageais de tester toute la théorie en utilisant des systèmes réelles et de démontrer que cette méthode soit utile en donnant au moins un complément aux méthodes existantes. S'il était possible de valider et davantage de valoriser ces théories, on disposerait d'une méthode qui donne un profil de densité électronique ab-initio, c'est à dire un modèle sans aucun paramètre ajustable.

J'ai pu démontrer qu'il est vraiment faisable de faire traverser les données expérimentales enregistrées sur des systèmes substrat/couche mince issus de ce laboratoire les calculs successifs des relations Kramers-Kronig et ceux de la solution du problème inverse pour enfin aboutir à une densité électronique qui était tout à fait acceptable au point de vue physicochimique (Van der Lee (2000b)). La figure x montre une exemple d'une courbe de réflectivité enregistré sur une couche de carbon déposée sur un substrat de silicium (courbe pleine). En tirets est la courbe de simulation calculé à partir d'une modèle simple consistant d'un substrat et une couche mince. On s'aperçoit que le contraste expérimentale des franges est beaucoup plus fort que le contraste calculé.

Ensuite un profil de densité était calculé en utilisant les relations de Kramers-Kronig et la solution du problème inverse (courbe pleine en Fig. X). La réflectivité calculé à base de ce modèle est obligatoirement en accord parfait avec les données expérimentales. Ce modèle a servi de construire un modèle de deux couches qui donnait également un fit tout à fait acceptable (courbe en pointillés en Fig. X). Le modèle même est en pointillés en Fig. X. En bas de la figure X est montré la différence logarithmique entre les données expérimentales et calculées pour le modèle simple couche et le modèle double couche. Le modèle obtenu est physiquement tout à fait acceptable, vu l'adhérence réduite de telles couches au substrat.

En plus de la validation expérimentale des théories j'ai obtenu des formules phénoménologiques pour obtenir des classes de profils de densité qui sont ‘acceptables’ pour la méthode. Finalement une nouvelle méthode pour la déconvolution des données de la fonction instrumentale est présentée. La déconvolution sera indispensable si la couche devient plus épaisse.

2.3.3 Vers une vraie détermination *ab-initio* des profils de densité électronique par réflectométrie de rayons-X en incidence rasante.

Bien que la méthode présentée en § 2.3.2 soit utile dans un bon nombre de cas, de l'information préalable, notamment sur le profil de densité attendu, reste nécessaire. La vraie détermination *ab-initio* nécessite le mesure directe de la phase ou une dérivation plus rigoureuse des données expérimentales. Ceci se fait par un deuxième enregistrement, avec une couche de référence bien connue (Aktosun and Sacks (2000a,b)). L'ensemble des données permet, en théorie, d'obtenir un ou deux jeux de phases, qui peuvent être utilisé pour calculer un ou deux profils de densité. La théorie pour extraire la phase des amplitudes mesurées vient d'être développé, mais il est à prouver que cette théorie soit applicable en utilisant des données expérimentales. Il y a quelques expériences de neutrons qui montrent qu'une sous-théorie de la théorie générale peut être appliquée en utilisant des données expérimentales (Schreyer *et al.* (1999)).

C'est dans cette direction que dirige actuellement ma recherche. Il y a beaucoup de systèmes dont la réflectivité ne se modélise pas de façon simple, simplement parce que le profil de densité n'est pas constant à travers de la couche. Le développement d'une méthode *ab-initio* qui est exploitable au niveau du laboratoire et pas uniquement autour des grandes machines comme les sources neutron ou synchrotron sera certainement un pas avant dans la méthodologie de la réflectométrie. Il est l'intention que ce projet sera développé en collaboration avec des chercheurs à *l'Institut de Chimie des Surfaces et Interfaces* à Mulhouse. Les premiers enregistrement de test ont été fait et montrent que les couches déposés à Mulhouse ne sont pas très faciles à exploiter ; elles sont par conséquent idéales pour une approche *ab-initio*. Il est à noter que ce projet innovateur devrait s'appliquer à n'importe quel système. Il est à étudier si ceci est vraiment le cas.

Références

A. van der Lee, S. van Smaalen, G.A. Wiegers, and J.L. de Boer, *Phys. Rev. B* **43**, 9420 (1991)

- P. M. de Wolff, *Acta Crystallogr. A* **30**, 777 (1974).
- A. Janner and T. Janssen, *Phys. Rev. B* **15**, 643 (1977).
- A. van der Lee, R. van de Belt and G. A. Wiegers, *J. Alloys and Compounds* **178**, 57 (1992).
- V. Petřícek, A. van der Lee, and M. Evain, *Acta Crystallogr. A* **51**, 529 (1995).
- A. van der Lee, M. Evain, L. Monconduit, R. Brec, J. Rouxel, and V. Petřícek, *Acta Crystallogr. B* **50**, 119 (1994).
- S. Lee, P. Colombet, G. Ouvrard, and R. Brec, *Inorg. Chem.* **27**, 1291 (1988).
- A. van der Lee, M. Evain, L. Monconduit, R. Brec, and S. van Smaalen, *J. Phys.: Cond. Matter* **6**, 933 (1994)
- A. van der Lee, M. Evain, M. Mansuetto, L. Monconduit, R. Brec, and J. Rouxel, *J. Solid State Chem.* **111**, 75 (1994)
- A. van der Lee, M. Evain, L. Monconduit, R. Brec, and V. Petřícek, *Inorg. Chem.* **33**, 3032 (1994).
- M. Evain, L. Monconduit, A. van der Lee, R. Brec, and E. Canadell, *New J. Chem.* **18**, 215 (1994).
- M. Evain, A. van der Lee, L. Monconduit, and V. Petřícek, *Chem. Mater.* **6**, 1776 (1994).
- F. Boucher, V. Zhukov, and M. Evain, *Inorg. Chem.* **35**, 7649 (1996).
- A. van der Lee, L.M. Hoistad, M. Evain, B. Foran, and S. Lee, *Chem. Mater.* **9**, 218 (1997).
- M. V. Klibanov and P. E. Sacks, *J. Math. Phys.* **33**, 3813 (1992)
- W. L. Clinton, *Phys. Rev. B* **48**, 1 (1993).
- A. van der Lee, S. Roualdes, R. Berjoan, and J. Durand, Submitted to *Appl. Surf. Sci.* (2000).
- A. van der Lee, *Eur. Phys. J. B* **13**, 755 (2000).
- A. van der Lee, *Solid State Sciences* **2**, 257 (2000).
- T. Aktosun and P. E. Sacks, *Inverse Problems* **16**, 821 (2000).
- T. Aktosun and P. E. Sacks, *SIAM J. Appl. Math.* **60**, 1340 (2000).
- A. Schreyer, C. F. Majkrzak, N. F. Berk, H. Grüll, C. C. Han, *J. Chem. Phys. Sol.* **60**, 1045 (1999).

Determination of the Commensurately Modulated Structure of NbGe_{2/5}Te₂ from Twinned-Crystal Data

A. van der Lee,¹ M. Evain, M. Mansuetto,² L. Monconduit, R. Brec, and J. Rouxel

IMN, Laboratoire de Chimie des Solides, 2, Rue de la Houssinière, 44072 Nantes Cedex 03, France

Received October 27, 1993; in revised form February 4, 1994; accepted February 7, 1994

IN HONOR OF C. N. R. RAO ON HIS 60TH BIRTHDAY

The commensurate modulation of the NbGe_{2/5}Te₂ structure has been determined from X-ray diffraction data collected on a twinned crystal. The (3 + 1)D superspace group is $P2_1/n(0\beta\gamma)$, $\beta = 0.0$, $\gamma = 0.4$. The basic unit cell dimensions are $a = 6.4437(9)$, $b = 16.004(2)$, $c = 3.8936(4)$ Å, $\alpha = 119.10(1)^\circ$, $V = 350.85(7)$ Å³, and $Z = 4$. Final R factors are 0.051, 0.122, 0.187, and 0.110 for 742 main reflections, 1573 first-order superreflections, 927 second-order superreflections, and the combined set, respectively. Twinning is taken into account by an extra basic vector; the intensities of all reflections, overlapping as well as non-overlapping, are used in the final refinement. The twin volume ratio is refined to $\nu = 0.418(1)$. NbGe_{2/5}Te₂ is a layered compound consisting of [Te/Nb, Ge/Te] sandwiches with a close to orthorhombic basic structure modulated by strong monoclinic, commensurate occupational and displacive waves. Bond distances in the structure of NbGe_{2/5}Te₂ compare very well with those in the three- and seven-fold orthorhombic superstructures of NbGe_{1/3}Te₂ and NbGe_{3/7}Te₂, respectively. It is shown that all three structures are built from the same intrasandwich subunits, and that the stacking, and accordingly the 3D symmetry, is determined by the subunit geometry. The pinning of two sandwiches on each other is related to a few short intersandwich Te–Te contacts that in turn can be correlated to the electronic stabilization of the compound.

© 1994 Academic Press, Inc.

INTRODUCTION

Recent investigations in the phase diagram of M – A –Te ($M = \text{Nb}, \text{Ta}$; $A = \text{Si}, \text{Ge}$) have shown that $MA_x\text{Te}_2$ ($1/3 \leq x \leq 1/2$) compounds are characterized by a strong occupational modulation wave of both M and A occurring along with important displacive modulation waves of all atoms (1, 2). The structures are built from infinite two-dimensional [Te/ M , A /Te] sandwiches, separated by empty Van der Waals gaps.

Research on the $MA_x\text{Te}_2$ tieline of the M – A –Te phase diagram is of interest, because it allows subtle changes to be monitored in the electronic structure versus changes in the geometric structure quite easily. Since oxidation states of 3+ and 2+ can be assigned to M and A (3), respectively, the mean oxidation state of Te has to be $-(3+x)/2$. The latter oxidation state gives rise to an electronic transfer from Te p orbitals to M metal d -block bands (4). Fairly short intersandwich Te–Te contacts have been correlated to this electronic transfer.

The structural variation due to a variation of x is expressed in a variation of the magnitude of the modulation wave vector, since it can be shown that $\mathbf{q} = \gamma\mathbf{c}^* = x\mathbf{c}^*$ (1). x may take either rational values, leading to superstructures commensurate with the basic unit cell, or irrational values, yielding incommensurate structures with symmetry that cannot be described by an ordinary 3D space group. It should be noted that all structures are fully ordered, despite the use of (ir)rational values for x in $MA_x\text{Te}_2$. It was recently shown that (3 + 1)D superspace groups are suitable for a unified description of both commensurate and incommensurate structures in the $MA_x\text{Te}_2$ series (2).

Three different commensurate superstructures have been reported, viz. NbSi_{1/2}Te₂ (5); $MA_{1/3}\text{Te}_2$ with $M = \text{Nb}, A = \text{Ge}$ (6, 7), $M = \text{Nb}, A = \text{Si}$ (8), and $M = \text{Ta}, A = \text{Si}$ (3); and NbGe_{3/7}Te₂ (2). One incommensurate structure has been determined, viz. TaSi_{0.36}Te₂ (1). All compounds, except NbSi_{1/2}Te₂, share the same (super)space group, viz. $Pnma(00\gamma)s00$. Apart from structure determinations, other investigations have been made, including band structure calculations (4), Scanning Tunneling Microscopy (STM) and Atomic Force Microscopy (AFM) imaging (9), and Li- and Na-intercalation experiments (10).

The compound which is the subject of this paper, NbGe_{2/5}Te₂, is different from all known orthorhombic $MA_x\text{Te}_2$ compounds, since the modulation wave has a clear monoclinic symmetry, whereas the basic structure

¹ To whom correspondence should be addressed.

² On leave from Department of Chemistry, Northwestern University, Evanston, Illinois 60208-3113.

remains very close to orthorhombic. The nature of the monoclinic modulation in $\text{NbGe}_{2/5}\text{Te}_2$ will be discussed, along with the relation with the other phases in the $MA_x\text{Te}_2$ series.

EXPERIMENT

Numerous crystals of $\text{NbGe}_{2/5}\text{Te}_2$ were found in the batch that was obtained for the synthesis of $\text{NbGe}_{1/3}\text{Te}_2$ (7). A similar synthesis with the elements weighted in the proper ratios was performed (the heating scheme was several hours at 700 K, 2 days at 900 K, 2 days at 1100 K, 10 days at 1280 K, followed by quenching to air). SEM analysis, using CrGeTe_3 as internal standard for Ge, yielded the composition $\text{Nb}_{29}\text{Ge}_{12}\text{Te}_{60}$. Analysis by Weissenberg photographs showed a fairly complicated diffraction pattern in the b^* , c^* plane. However, a basic lattice consisting of strong spots could be identified with cell parameters very close to those of the $\text{NbGe}_{1/3}\text{Te}_2$ basic lattice. The metric symmetry of the basic unit cell is, within experimental error, orthorhombic. The weaker reflections could be indexed with two q vectors (Fig. 1),

$$\mathbf{q}_1 = \frac{2}{5} \mathbf{b}_o^* + \frac{1}{5} \mathbf{c}_o^* \quad [1]$$

$$\mathbf{q}_2 = -\frac{2}{5} \mathbf{b}_o^* + \frac{1}{5} \mathbf{c}_o^*. \quad [2]$$

Data collection of the main reflections and of the weaker satellite reflections (related to the main ones through Eqs. [1] and [2]) was performed on a SIEMENS-P4 diffractometer (see Table 1 for the recording conditions). The measured intensities were corrected for scale variation and Lorentz-polarization effects. A Gaussian absorption correction was applied using the ABSORB program from the XTAL system software (11). Symme-

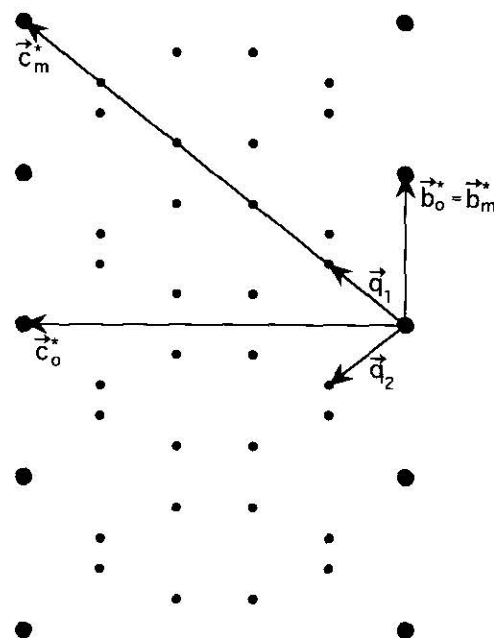


FIG. 1. Diffraction pattern of $\text{NbGe}_{2/5}\text{Te}_2$ in the b^* , c^* plane.

try-related reflections were averaged according to Laue symmetry $2/m11$ (vide infra), yielding an internal consistency factor based upon observed reflections of $R_i = 0.053$. A final number of 742 main reflections, 1573 first-order satellites, and 927 second-order reflections with intensities $I > 2.5\sigma(I)$ were available for the refinements.

SYMMETRY AND STRUCTURE REFINEMENT

The choice of two q vectors according to Eqs. [1] and [2] and of the basic lattice defined in Fig. 1 implies that the modulation in $\text{NbGe}_{2/5}\text{Te}_2$ is two dimensional and that the symmetry of the structure should be described by a (3 + 2)D orthorhombic superspace group. However, doubts arose on the proper symmetry of the structure because of the apparent absence of "mixed"-order satellite reflections $(h, k, l, \pm 1, \pm 1)$ or $(h, k, l, \pm 2, \pm 2)$, which may appear, for example, on the basic reciprocal axes in between the main spots. These mixed-order reflections could not be detected on long-exposure Weissenberg films or by a special search with the diffractometer on the appropriate spots in reciprocal space. Therefore, a twin model was considered with a twofold axis (twin element) along c_o^* in reciprocal space and along c in direct space. A similar model was used before by Gao *et al.* (12) to explain the complete absence of mixed-order reflections in the apparently 2D modulated structure of $\text{Bi}_2\text{Sr}_{2-x}\text{Ca}_x\text{CuO}_6$. The second q vector is related to the first q vector by the twin element; thus the modulation is no longer 2D, but is 1D. In addition, the symmetry is no longer orthorhombic, but has to be monoclinic. In princi-

TABLE 1
Crystal Data of $\text{NbGe}_{2/5}\text{Te}_2$ and Measurement Conditions

Formula weight (g)	377.15
Density (calc)	7.14
$F(000)$	631
Linear absorption coefficient	228.0 cm^{-1}
Maximum correction	9.31
Minimum correction	1.31
Crystal size	$<0.12 \times 0.006 \times 0.12 \text{ mm}^3$
Diffractometer	Siemens P4
Temperature	295 K
Radiation	$\text{MoK}\alpha$
Scan mode	$\omega/(2\Theta)$
Recording range	1.00–42.50°
$hklm$ range	$-12 < h < 12$ $-15 < k < 26$ $-1 < l < 7$ $-2 < m < 2$
Standard reflections	0–42, 060, 3–21 every 100 reflections

ple, one can proceed with the structure analysis without any axis transformation, since a monoclinic symmetry for the modulated structure may have a basic unit cell with orthorhombic metric symmetry. To demonstrate the monoclinic symmetry more clearly, we have chosen to transform the basic unit cell according to

$$\mathbf{a}_m^* = \mathbf{a}_o^* \quad [3]$$

$$\mathbf{b}_m^* = \mathbf{b}_o^* \quad [4]$$

$$\mathbf{c}_m^* = 2\mathbf{b}_o^* + \mathbf{c}_o^*. \quad [5]$$

With this transformation, the modulation wave vector lies along the \mathbf{c}_m^* axis ($\mathbf{q} = \frac{1}{5}\mathbf{c}_m^*$). As a final modification, we have taken \mathbf{q} to be twice as large, since the first-order satellites match the strongest satellites. The nonstandard setting of the monoclinic space group, i.e., a -axis unique, was retained to facilitate comparison with the already published structures in the MA_xTe_2 series.

It is noted that the twin lattice, i.e., the lattice corresponding to the intersection of the lattices of the two twin components, coincides with the basic lattice of the modulated structure. One can deduce from Fig. 1 that the twin index, i.e., the ratio between the volume of the primitive unit cell of the twin components and that of the twin lattice, is five. The twin index is in this case just equal to the ratio of the volumes of supercell and basic cell.

The systematic absences of the diffraction pattern pointed to the (3 + 1)D superspace groups $P2_1/n(0\beta\gamma)$ and $P2_1/n(0\beta\gamma)0s$ (both equivalent to No. 13.1 of Table 9.8.3.5 of IT, Vol. C (13)). A few clear violations of the extinction conditions of the latter made us choose the first setting as the correct one. This was later confirmed by the refinement results. The 3D space group of this commensurate superstructure is $P2_1/n$ (a -axis unique).

The refinement of the structure was performed using the Van Smaalen–Petříček formalism for twinned structures (14). Within this formalism an extra reciprocal basic vector is used for integer indexing of all diffraction spots originating from a twinned crystal. In this case five reciprocal basic vectors (\mathbf{a}_m^* , \mathbf{b}_m^* , \mathbf{c}_m^* , \mathbf{q}_1 , \mathbf{q}_2) are needed for integer indexing; the first three are used for the basic structure, the fourth describes the modulation, and the fifth takes into account the twinning. Using this basic set of reciprocal vectors, the matrix representation for the twin element T_{2z} is

$$T_{2z} = \begin{bmatrix} -1 & 0 & 0 & 0 & 0 \\ 0 & -1 & -4 & 0 & 0 \\ 0 & 0 & 1 & 0 & 0 \\ 0 & 0 & 0 & 0 & 1 \\ 0 & 0 & 0 & 1 & 0 \end{bmatrix}. \quad [6]$$

The expression for the structure factor becomes accordingly

$$F_{tw}^2(h, k, l, m_1, m_2) = (1 - \nu)F^2(h, k, l, m_1)\delta(m_2, 0) \quad [7] \\ + \nu F^2(\bar{h}, \bar{k} + 4\bar{l}, m_2)\delta(m_1, 0),$$

where ν is the twin volume fraction and δ the Kronecker delta function which is 1.00 if both arguments are equal and 0.00 otherwise. It is noted that with this formalism the intensities of all reflections, from the overlapping reflections of the twin lattice as well as from the isolated spots, are simultaneously taken into account.

Refinement of the structure proceeded as described before (2). It was assumed that the arrangement of the cations within the sandwiches is similar to that found in $MA_{1/3}Te_2$ and $MA_{3/7}Te_2$. From this assumption starting values for the Fourier amplitudes of the occupational modulation waves were calculated and found to be in coarse agreement with the relative magnitude of the first- and second-order reflections. The refinement of the displacive modulation parameters for Te proceeded without difficulties in contrast with those for Nb and Ge where large correlations between the different parameters hampered the convergence. The reason is that some of the parameters are redundant since not all cationic positions are occupied. For example, Nb(1) occupies three independent general positions in the supercell. The symmetry allows the refinement of five parameters for each of the coordinates, i.e., the mean, and two parameters (the sine and cosine amplitude) for both the first and the second harmonic. A simple rule of thumb was developed, the so-called maximum determinant rule (15), to choose exactly those parameters which give the fewer correlations in the refinement. With this choice, the refinement converged rapidly and a false minimum could be avoided. The minimum was found to be stable against sign reversal of arbitrarily chosen Fourier amplitudes, another known pitfall in the refinement of modulated structures. In addition, a refinement was performed using the structure factor expression for incommensurate structures, since an undetected offset of the commensurate determined value of γ can produce quite different intensities at the satellite positions. It was, however, found that the R values of the commensurate calculation are much better than those of the incommensurate calculation, so it is concluded that the value for γ is exactly equal to $\frac{1}{5}$.

The final R factors are $R = 0.051, 0.122, 0.187, 0.110$ and $wR = 0.052, 0.110, 0.181, 0.098$ for main reflections, first-order satellites, second-order reflections, and main reflections, respectively. The twin volume fraction refined to 0.418(1). The parameters of the occupational waves were refined, leading to a small drop in the R factors, but the changes from 1.00 and 0.00 occupancies

TABLE 2
Final Values of the Displacive Modulation Functions for the Structure of $\text{NbGe}_{25}\text{Te}_2$

ν	n	$A_{x,s,n}^\nu$	$A_{y,s,n}^\nu$	$A_{z,s,n}^\nu$	$A_{x,c,n}^\nu$	$A_{y,c,n}^\nu$	$A_{z,c,n}^\nu$
Nb(1)							
	0				0.3196(3)	0.2505(4)	-0.0377(9)
	1	0.0140(6)	0.0013(4)	0.067(1)	0.0	0.0	0.0
	2	0.055(6)	0.0006(5)	0.006(1)	0.0	0.0	0.0
Nb(2)							
	0				0.0316(4)	0.2493(3)	-0.0707(8)
	1	0.0	0.0	0.0	0.0	0.0	0.0
	2	0.0	0.0	0.0	-0.0003(7)	0.0017(4)	0.030(1)
Ge							
	0				0.4236(5)	0.2494(4)	0.258(1)
	1	0.0	0.0	0.0	0.0	0.0	0.0
	2	-0.0024(7)	0.011(5)	0.031(1)	0.0	0.0	0.0
Te(1)							
	0				0.6682(2)	0.1162(1)	0.7536(4)
	1	0.0034(3)	-0.0022(2)	0.0126(6)	0.0430(3)	-0.0004(2)	0.0009(6)
	2	-0.0011(3)	-0.0002(2)	-0.0239(5)	0.0172(4)	-0.0012(2)	0.0087(6)
Te(2)							
	0				0.1678(2)	0.1159(1)	0.2124(4)
	1	-0.0448(3)	0.0003(2)	0.0094(7)	0.0062(3)	0.0018(2)	0.0203(7)
	2	-0.0087(3)	0.0034(2)	0.0356(6)	-0.0139(4)	0.0008(2)	-0.0062(7)

Note. The Fourier amplitudes of the displacive waves have been defined as

$$\mathbf{r}^\nu(\bar{x}_4) = \sum_{n=0}^2 [\mathbf{u}_{s,n}^\nu \sin(2\pi n \bar{x}_4) + \mathbf{u}_{c,n}^\nu \cos(2\pi n \bar{x}_4)],$$

where ν counts the independent atoms in the basic unit cell. The argument of the modulation function has been defined as $x_4 = t + \mathbf{q} \cdot \mathbf{r}_{0,L} = t + \mathbf{q} \cdot (\mathbf{r}_0' + \mathbf{L})$, with t the global phase of the modulation wave ($t = 0$ is used in the present work), \mathbf{L} a basic structure lattice translation; and $\mathbf{u}_{s,n}^\nu = (A_{x,s,n}^\nu, A_{y,s,n}^\nu, A_{z,s,n}^\nu)$, $\mathbf{u}_{c,n}^\nu = (A_{x,c,n}^\nu, A_{y,c,n}^\nu, A_{z,c,n}^\nu)$. It is noted that the "mean" of the modulation functions is represented by $n = 0$, but this amplitude is only equal to the crystallographic mean in the case of Te.

were only very small. Several explanations can be offered for the rather high overall agreement factors. As for all modulated structures the intensities of the satellites for this compound are rather low compared to those of the main reflections and are accordingly measured with lower accuracy. Since 77% of the data consists of satellites, this will be reflected in the overall R factors. A second explanation is offered by the uncertainty in the absorption correction due to the twinned nature of the crystal. The absorption of X-rays through the crystal depends strongly on whether microcrystals of the two different orientations are dispersed throughout the crystal, or if there are only two domains. The important role of the absorption correction is reflected in the final residues in the difference Fourier maps which are mainly found near the Te atoms, the heaviest element in the compound. However, the model resulting from the refinements is completely trustworthy, since no anomalous bond distances are found and the model scales very well

with the other structures in the $MA_x\text{Te}_2$ series. Fourier amplitudes of the displacive modulation wave are compiled in Table 2, the (calculated) Fourier amplitudes for the occupational modulation wave in Table 3, and the final values of the temperature factors in Table 4. Lists of structure factors and tables of bond distances have been deposited.³

The scattering factors for neutral atoms and the anomalous dispersion correction were taken from "International Tables for X-Ray Crystallography" (16). The re-

³ See NAPS document No. 05112 for 28 pages of supplementary material. Order from ASIS/NAPS, Microfiche Publications, P.O. Box 3513, Grand Central Station, New York, NY 10163. Remit in advance \$4.00 for microfiche copy or for photocopy, \$7.75 up to 20 pages plus \$.30 for each additional page. All orders must be prepaid. Institutions and Organizations may order by purchase order. However, there is a billing and handling charge for this service of \$15. Foreign orders add \$4.50 for postage and handling, for the first 20 pages, and \$1.00 for additional 10 pages of material. \$1.50 for postage of any microfiche orders.

TABLE 3

Values for the Amplitudes of the Occupation Probability Modulation Waves in the Structure of $\text{NbGe}_{2/5}\text{Te}_2^a$

<i>n</i>	$P_{s,n}^v$	$P_{c,n}^v$
Nb(1)		
0		0.600000
1	-0.328786	-0.557481
2	-0.216347	-0.119618
Nb(2)		
0		0.400000
1	0.282527	0.582292
2	0.194181	0.152997
Ge		
0		0.400000
1	0.619499	0.187366
2	0.137006	-0.205777

^a The values have been calculated to give a fully ordered distribution of cations, i.e., a site is empty ($P = 0.00$) or occupied ($P = 1.00$), from the defining equation

$$P^v(\bar{x}_4) = \sum_{n=0}^2 [P_{s,n}^v \sin(2\pi n \bar{x}_4) + P_{c,n}^v \cos(2\pi n \bar{x}_4)]$$

(for the definition of the different symbols see the note to Table 2).

finements were performed in the full-matrix mode, using $w = 1/(\sigma^2(|F_{\text{obs}}|) + 0.01 |F_{\text{obs}}|^2)$ as weights. All structural calculations have been performed with the computing system JANA93 (17).

DISCUSSION

In the $MA_x\text{Te}_2$ structures there are two $[\text{Te}/M, A/\text{Te}]$ sandwiches per unit cell parallel to the \mathbf{a}, \mathbf{c} plane. Figure 2 shows a projection of one of the two sandwiches of $\text{NbGe}_{2/5}\text{Te}_2$ upon the plane $y = 0.25$. The Te sheets that make the sandwich are in an AA stacking mode. It is

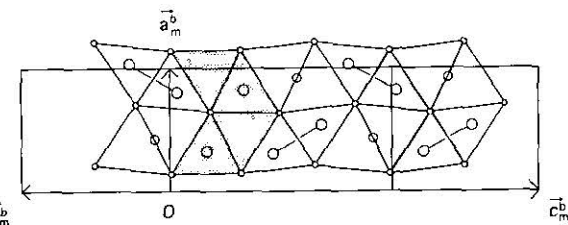


FIG. 2. Projection of one sandwich of the structure of $\text{NbGe}_{2/5}\text{Te}_2$ on the plane $y = 0.25$. Te atoms (smallest circles) form the approximate hexagonal net, Nb atoms (largest circles) are in the middle of Te triangles, and Ge atoms (medium circles) are halfway Te-Te contacts. The so-called fault is shaded.

noted that the $Pnma$ symmetry of $\text{NbGe}_{1/3}\text{Te}_2$ and $\text{NbGe}_{3/7}\text{Te}_2$ requires that atoms of the second Te sheet are exactly on top of the atoms of the first sheet. This is no longer required by the $P2_1/n$ symmetry of the structure of $\text{NbGe}_{2/5}\text{Te}_2$. Nevertheless, as can be seen from Fig. 2 and a closer inspection of the data in Table 2, the exact AA stacking mode is still present to a very good approximation. In addition, the deviations of the y coordinates of the cations from 0.25, which are identical to zero in $Pnma$ symmetry, are very small. These two observations imply that the m_y mirror plane, which is formally lost in going from $Pnma$ to $P2_1/n$, is still approximately present. The basic structure still has approximately $Pnma$ symmetry; the only significant deviation concerns the z coordinates of Te(1) and Te(2) which should sum up to 1.00 in $Pnma$ symmetry.

There are four Nb-Nb pairs, two lone Nb atoms, and four Ge atoms per sandwich per unit cell in the $\text{NbGe}_{2/5}\text{Te}_2$ structure. With the general formula of the commensurate structures in the $MA_x\text{Te}_2$ series, viz. $MA_{(1+n)/(3+2n)}\text{Te}_2$, $n = 0, 1, \dots, \infty$ (2), one can count $2(1+n) M-M$ pairs per sandwich per unit cell, two lone M atoms, and $2(1+n)A$ atoms. One peculiar feature of the $MA_x\text{Te}_2$ structures is the herringbone motif of $M-M$ pairs running in the infinite two-dimensional sheets. The lone M (Nb) atoms form bands (shaded in Fig. 2) that are perpendicular to the running direction of the modulation

TABLE 4
Final Values for the Thermal Parameters^a

	U_{11}	U_{22}	U_{33}	U_{12}	U_{13}	U_{23}
Nb(1)	0.0058(6)	0.0059(6)	0.013(1)	0.0001(9)	0.0017(7)	0.002(1)
Nb(2)	0.0054(7)	0.0047(8)	0.008(1)	0.002(1)	0.0008(7)	0.002(1)
Ge	0.010(1)	0.013(1)	0.015(1)	0.000(1)	0.000(1)	0.006(1)
Te(1)	0.0080(4)	0.0065(6)	0.0081(5)	0.0006(5)	0.0008(5)	0.0031(5)
Te(2)	0.0063(4)	0.0070(7)	0.0135(6)	0.0005(5)	0.0003(5)	0.0018(5)

^a Temperature parameters according to the Cruickshank notation. Standard deviations in parentheses.

TABLE 5
Main Interatomic Distances in the Structures of $\text{NbGe}_{(1+n)/(3+2n)}\text{Te}_2$ ($n = 0, 1, 2$)^a

Contact	$\langle d \rangle$	$\text{NbGe}_{1/3}\text{Te}_2$			$\text{NbGe}_{2/5}\text{Te}_2$			$\text{NbGe}_{3/7}\text{Te}_2$				
		$\sigma_{\langle d \rangle}$	d_{\min}	d_{\max}	$\langle d \rangle$	$\sigma_{\langle d \rangle}$	d_{\min}	d_{\max}	$\langle d \rangle$	$\sigma_{\langle d \rangle}$	d_{\min}	d_{\max}
Nb-Nb	2.920	0.000	2.920	2.920	2.903	0.024	2.886	2.920	2.887	0.066	2.818	2.945
Nb-Ge	2.818	0.040	2.736	2.858	2.811	0.031	2.754	2.842	2.801	0.032	2.756	2.847
Nb-Te	2.846	0.064	2.747	2.950	2.863	0.060	2.751	2.976	2.864	0.064	2.763	2.964
Ge-Te	2.768	0.026	2.745	2.790	2.777	0.030	2.735	2.820	2.770	0.032	2.728	2.800
Te-Te ^b	3.892	0.144	3.766	4.123	3.935	0.136	3.743	4.209	3.949	0.150	3.739	4.211
Te-Te ^c	3.818	0.242	3.338	4.121	3.818	0.244	3.316	4.137	3.823	0.246	3.306	4.102
Te-Te ^d	3.768	0.070	3.647	3.782	3.747	0.065	3.633	3.792	3.753	0.061	3.625	3.817

^a $\langle d \rangle$ is the mean of all closest contacts found in the structure, $\sigma_{\langle d \rangle}$ is the standard deviation of this mean; thus, it is not the usual crystallographic experimental standard deviation. d_{\min} and d_{\max} are the minimal and maximal distance, respectively, in each type of distance.

^b Te-Te contacts through the Van der Waals gap, i.e., joining two different sandwiches.

^c Te-Te contacts parallel through the sandwiches, i.e., within one Te sheet.

^d Te-Te contacts through a sandwich, i.e., joining the two Te sheets that form one sandwich.

wave. Since the density of these bands of lone M atoms diminishes upon increasing n , they will be referred to as "faults," although they appear strictly periodic. Another particular feature of $MA_x\text{Te}_2$ structures is the square coordination of A (Ge) by Te which is not found in any other chalcogenide. A (Ge) is not only in square coordination by Te, but also approximately by Nb. Distances compare very well between the three-fold superstructure of $\text{NbGe}_{1/3}\text{Te}_2$ ($n = 0$), the five-fold superstructure of $\text{NbGe}_{2/5}\text{Te}_2$ ($n = 1$), and the seven-fold superstructure of $\text{NbGe}_{3/7}\text{Te}_2$ ($n = 2$) (Table 5). In addition, the standard deviations of the mean for each type of distance, and the minimum and maximum of each type, are rather similar for the three superstructures. This implies that even the individual distances do not differ much. Both Nb-Nb as Nb-Ge distances are within bonding range. The in-plane Te-Te distances have a wide range, the smallest distances (3.32 Å) being found across the Nb-Nb bonds, and the largest (4.14 Å) in the Te squares surrounding the Ge atoms.

The second sandwich within the unit cell is identical to the first sandwich, but shifted to make an overall AA/BB stacking sequence. This is true for monoclinic $\text{NbGe}_{2/5}\text{Te}_2$ as well as for orthorhombic $\text{NbGe}_{1/3}\text{Te}_2$ and $\text{NbGe}_{3/7}\text{Te}_2$. It is recalled that the basic unit cell is orthorhombic in all three cases. Figure 3 gives the relation between the orthorhombic basic unit cell and the monoclinic supercell of $\text{NbGe}_{2/5}\text{Te}_2$. It is seen that a translation along one basic vector \mathbf{b}_o is accomplished by exactly two basic shifts along \mathbf{c}_o . This causes the cationic arrangement of the second sandwich to be in a different orientation with respect to that of the first sandwich compared to the case when the two basic shifts along \mathbf{c}_o are absent (i.e., when the superstructure has orthorhombic

metric symmetry). It should be noted that these two basic shifts along \mathbf{c}_o do not alter the AA/BB stacking sequence.

The question as to why the monoclinic superstructure is energetically more favorable than the hypothetical orthorhombic superstructure of $\text{NbGe}_{2/5}\text{Te}_2$ is difficult to answer. It was shown before (2) by the derivation of the possible 3D space group belonging to the superspace group $Pnma(00 n_1/n_2)s00$ that for $n_1 + n_2 = \text{odd}$, i.e., exactly for $\mathbf{q} = \frac{2}{3} \mathbf{c}^*$, a monoclinic 3D space group can be expected. One reason for the monoclinic symmetry occurrence might be the difference in relative orientation of the cationic arrangement in the two sandwiches for the monoclinic and orthorhombic variants.

Another possibility is that intersandwich Te-Te interactions cause the shift of one sandwich with respect to the other. It was shown before (2) that all structures in the $MA_x\text{Te}_2$ series, whether commensurate or incommensurate, can be thought to be built from three different subunits. In Fig. 4 a schematic representation is given for one sandwich for each of the three superstructures $n = 0$,

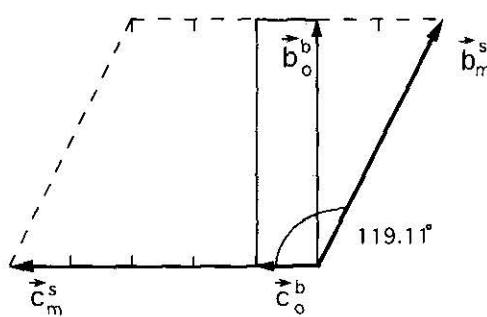


FIG. 3. Relation between the orthorhombic basic unit cell (cell axes \mathbf{a}_o^b , \mathbf{b}_o^b , \mathbf{c}_o^b) and the fivefold monoclinic supercell (cell axes \mathbf{a}_m^s , \mathbf{b}_m^s , \mathbf{c}_m^s).

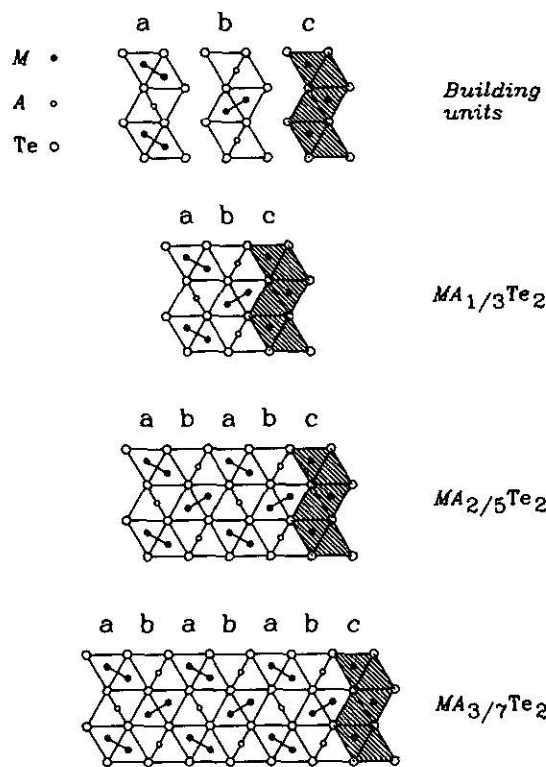


FIG. 4. Building units and structures of one sandwich of the $n = 0, 1, 2$ superstructures of $\text{MA}_{(1+n)/(3+2n)}\text{Te}_2$. The so-called fault is shaded.

1, 2. These subunits are fairly rigid, in view of the fact that the bond distances of like types for all three superstructures are rather similar (cf. Table 5). It can be easily imagined that these building blocks cannot stack in an arbitrary way if the top of each block is not flat, but buckled or puckered. In that case preferred orientations of one sheet with respect to the others will result. However, the Te sheets are nearly flat, except for two irregularities. Indeed, there are two Te atoms per sheet per unit cell⁴ that are protruded slightly *inward* by roughly 0.070 Å with respect to the Te sheet. One of these atoms was also clearly visible on AFM images of the structure (9). In addition, these two atoms, one on each side of the fault, form the *shortest* contacts between the two sandwiches (3.74–3.80 Å). These short intersandwich contacts have been related to the electronic transfer from Te *p* orbitals to *M d*-block bands (3, 4). It was shown that these short contacts are essential for raising one band per sandwich, with strong Te character, above the Fermi level to adjust the oxidation state of the Te atoms. When the oxidation states of *M* and *A* are assumed to be constant throughout the $\text{MA}_{(1+n)/(3+2n)}\text{Te}_2$ series, viz. 3+ and 2+ for *M* and *A*, respectively, one calculates a mean oxidation state of

$x = -(11 + 8n)/2(3 + 2n)$ for Te. In other words, 1 out of $2(3 + 2n)$ Te atoms has lost one electron. In principle, since there are exactly $2(3 + 2n)$ Te atoms per Te sheet per unit cell, only one intersandwich short Te–Te contact per Te sheet is required for the adjustment of the electron counting. Thus, the sandwich in itself is not stable, requiring short Te–Te contacts located on special positions of the Te sheets to stabilize the 3D structure. The special positions are determined by the intrasandwich geometry, and it is for that reason that the sandwiches are not stacked in an arbitrary way. Figure 5 shows the relative stacking of the two sandwiches, the special Te atoms, and the shortest intersandwich Te–Te contacts in relation with the faults.

Of course, the actual situation is more subtle: more than one intersandwich Te–Te contact per Te sheet was shown to be (slightly) bonding (3, 4), so the electron counting adjustment may be shared by several intersandwich Te–Te contacts. This is in accordance with other studies on tellurides that have shown Te anions to adopt a wide range of oxidation states between 1- and 2-, leading to a wide range of Te–Te distances (18). With regard to the monoclinic shift in $\text{NbGe}_{25}\text{Te}_2$, which is required to match the special positions of two adjacent Te sheets, it can be remarked that the shift is such that the *relative position* (counted along the *c* axis) of two faults in different sandwiches is exactly that found in the $\text{NbGe}_{1/3}\text{Te}_2$ three-fold superstructure, i.e., $\frac{2}{3} = (1 + \frac{1}{2})$ basic lattice translation along the *c* axis. For the seven-fold superstructure of $\text{NbGe}_{3/7}\text{Te}_2$ the spacing of the faults is wider, viz. $\frac{7}{3} = (3 + \frac{1}{2})$ basic lattice translation. As a more general rule, one can say that only spacings of $(k + \frac{1}{2})$, $k = \text{odd}$, will give the proper matching between two adjacent Te sheets needed to adjust the electron counting.

CONCLUDING REMARKS

$\text{NbGe}_{25}\text{Te}_2$ is a remarkable compound within the MA_xTe_2 series because of the monoclinic occupational and displacive modulation waves superimposed on an orthorhombic basic structure. Other compounds in the series have orthorhombic basic structures accompanied by orthorhombic modulation waves. The monoclinic symmetry of the modulation waves are related to a shift of exactly one basic lattice translation along \mathbf{c}_0 of one [Te/Nb, Ge/Te] sandwich with respect to another. A detailed analysis of bond distances and of the surface geometry of the Te sheets suggests that a sandwich can only be pinned upon another at special sites of the Te sheets, more precisely at a small number of dips in the surface. Those sites are the very ones responsible for the electronic stabilization of the structure. The dips can be made

⁴ For the orthorhombic structures these two atoms are related by an *a*-glide plane.

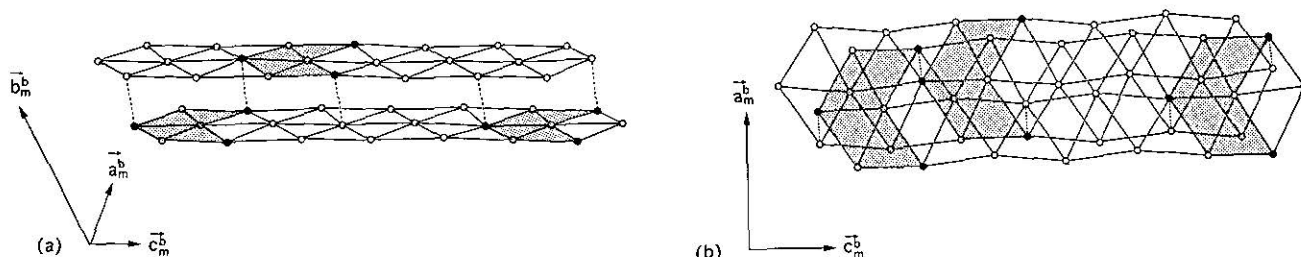


FIG. 5. Relative stacking of two consecutive sandwiches in the structure of $\text{NbGe}_{25}\text{Te}_2$. Shown are the two Te sheets that span the Van der Waals gap in side view (a) and in top view (b). The faults in the two sandwiches are shaded (cf. Fig. 2); closest intersandwich Te–Te contacts are indicated by hatched lines. Te atoms that are visible on AFM images are represented by small filled circles.

visible by AFM imaging (9), although their depth with respect to the otherwise flat Te sheets is only about 0.070 Å.

Of interest will be a further investigation of these dips in the surface of the Te sheets: would the electronic stabilization be absent if the dips were absent? Another question is how the pinning works in the very recently discovered incommensurate $\text{TaSi}_{0.414}\text{Te}_2$ compound with wave vector $\mathbf{q} = 0.414(1)\mathbf{c}^*$ (19). The magnitude of the wave vector of $\text{TaSi}_{0.414}\text{Te}_2$ is very close to that of $\text{NbGe}_{25}\text{Te}_2$, $\mathbf{q} = 0.400\mathbf{c}^*$, but in contrast with the latter compound, the former compound has orthorhombic symmetry both for its basic structure and for its modulation. The incommensurability of the $\text{TaSi}_{0.414}\text{Te}_2$ structure must be able to pin the second sandwich exactly at the right position for its electronic stabilization.

ACKNOWLEDGMENTS

The research of a.v.d.l. has been made possible by a Conseil Régional des Pays de la Loire grant and that of M.M. by NATO Grant (920049). Stimulating discussions with Dr. V. Petříček (Institute of Physics, Czech Academy of Sciences, Praha, Czech Republic) are gratefully acknowledged.

REFERENCES

1. A. van der Lee, M. Evain, L. Monconduit, R. Brec, J. Rouxel, and V. Petříček, *Acta Crystallogr. B*, **50**, 119 (1994).
2. A. van der Lee, M. Evain, L. Monconduit, R. Brec, and S. van Smaalen, *J. Phys.: Condens. Matter* **6**, 933 (1994).
3. M. Evain, L. Monconduit, A. van der Lee, R. Brec, J. Rouxel, and E. Canadell, *New J. Chem.* **18**, 215 (1994).
4. E. Canadell, L. Monconduit, M. Evain, R. Brec, J. Rouxel, and M.-H. Whangbo, *Inorg. Chem.* **32**, 10 (1993).
5. L. Monconduit, M. Evain, R. Brec, J. Rouxel, and E. Canadell, *C. R. Acad. Sci. Paris* **314**, 25 (1993).
6. J. Li and P. J. Carroll, *Mater. Res. Bull.* **27**, 1073 (1992).
7. L. Monconduit, M. Evain, F. Boucher, R. Brec, and J. Rouxel, *Z. Anorg. Allg. Chem.* **616**, 1 (1992).
8. J. Li, E. Badding, and F. J. DiSalvo, *J. Alloys Comp.* **184**, 257 (1992).
9. W. Liang, M.-H. Whangbo, M. Evain, L. Monconduit, R. Brec, H. Bengel, H. J. Cantow, and S. N. Magonov, accepted for publication, *Chem. Mater.* (1994).
10. L. Monconduit, P. Déniard, M. Evain, and R. Brec, to be published (1994).
11. S. R. Hall, H. D. Flack, and J. M. Stewart (Eds.), "Xtal3.2 Reference Manual," Universities of Western Australia, Geneva, and Maryland, 1992.
12. Y. Gao, P. Lee, J. Ye, P. Bush, V. Petříček and P. Coppens, *Physica C* **160**, 431 (1989).
13. A. J. C. Wilson (Ed.), "International Tables for Crystallography," Kluwer Academic Publishers, Dordrecht/Boston/London (1992).
14. S. van Smaalen and V. Petříček, *Acta Crystallogr. A* **48**, 610 (1992).
15. V. Petříček and A. van der Lee, in preparation (1994).
16. J. A. Ibers and W. C. Hamilton (Eds.), "International Tables for X-Ray Crystallography," Vol. IV. Kynoch, Birmingham, 1974.
17. V. Petříček, JANA93—Programs for Modulated and Composite Crystals, Institute of Physics, Praha, Czech Republic, 1993.
18. S. Jobic, R. Brec, and J. Rouxel, *J. Solid State Chem.* **96**, 169 (1992).
19. M. Evain, A. van der Lee, L. Monconduit, and V. Petříček, submitted for publication, *Chem. Mater.* (1994).

Modulated Structure of $\text{TaSi}_{0.414}\text{Te}_2$: Sandwich Stacking in the MA_xTe_2 ($\text{M} = \text{Nb}, \text{Ta}$; $\text{A} = \text{Si}, \text{Ge}$; $\frac{1}{3} \leq x \leq \frac{1}{2}$) Series

M. Evain,* A. van der Lee, and L. Monconduit

IMN, Laboratoire de Chimie des Solides, UMR CNRS No. 110, Université de Nantes, 2, rue de la Houssinière, 44072 Nantes Cedex 03, France

V. Petříček

Institute of Physics, Academy of Sciences of the Czech Republic, Na Slovance 2, 180 40 Praha 8, Czech Republic

Received March 31, 1994. Revised Manuscript Received June 6, 1994*

The complete structure of the incommensurate compound $\text{TaSi}_{0.414}\text{Te}_2$ has been determined by single-crystal X-ray diffraction. The $(3 + 1)\text{D}$ superspace group is $Pnma(00\gamma)s00$, $\gamma = 0.414(1)$, basic unit-cell dimensions $a = 6.318(1)$, $b = 14.031(2)$, $c = 3.8552(7)$ Å, $V = 341.8(1)$ Å³, and $Z = 4$. Refinement on 2989 reflections with $I \geq 2.5\sigma(I)$ converged to $R = 0.111$, $R = 0.054$ for 1100 main reflections and $R = 0.113, 0.164, 0.325$, and 0.527 for 1270 first-order, 311 second-order, 179 third-order, and 129 fourth- and sixth-order satellites, respectively. The structure can be considered as a succession of commensurate domains of the $\text{TaSi}_{3/7}\text{Te}_2$ and $\text{TaSi}_{2/5}\text{Te}_2$ structures. Although demonstrated as being incommensurate, the structure is compared to the closest, simple hypothetical commensurate structure, $\text{TaSi}_{5/12}\text{Te}_2$. A detailed analysis of the sandwich stacking in the MA_xTe_2 series, $\frac{1}{3} \leq x \leq \frac{1}{2}$, is performed. Stacking rules are established and a symmetry versus stacking relationship is discussed.

Introduction

Within the frame of a systematic study of the charge transfer processes in the MA_xTe_2 family of compounds ($\text{M} = \text{Nb}, \text{Ta}$; $\text{A} = \text{Si}, \text{Ge}$; $\frac{1}{3} \leq x \leq \frac{1}{2}$), several noteworthy features have already been found.^{1–11} MA_xTe_2 compounds have sandwich-like structures with the same intrasandwich basic unit cell, containing four face-sharing trigonal prisms of Te, a statistically occupied A-site in the center of the rectangular face common to two trigonal prisms, and two independent M sites in the centers of two trigonal prisms, whose occupancies sum up to exactly 1 (Figure 1).

The difference between the compounds stems from the setting-up of different x -dependent superstructures and from different sandwich stacking arrangements. For certain values of x the difference between a long-period

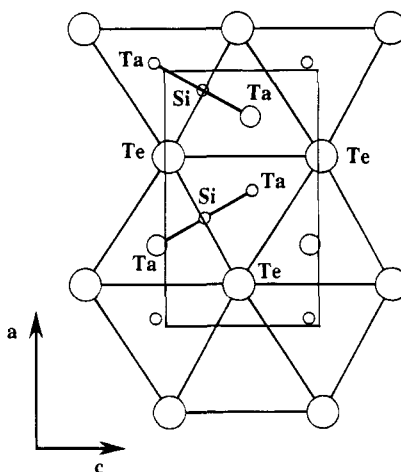


Figure 1. Projection of one sandwich of the basic unit cell of the $\text{TaSi}_{0.414}\text{Te}_2$ modulated structure. Te atoms form a hexagonal network; Ta atoms pairs and Si atoms are lone. The radius of the circles representing the atoms is proportional to their occupation probability.

superstructure and a true incommensurate phase cannot any longer be made. One of those phases, $\text{TaSi}_{0.414}\text{Te}_2$, is the subject of this paper.

The modulation primarily develops from a cationic ordering over the available sites within the sandwiches. Associated with the occupational modulation of M and A is a displacive modulation of all atoms.⁵ Most M atoms are bonded together to form M–M pairs. The remaining nonbonded M atoms form zigzag strips that demarcate the regions where M–M bonding takes place. Short Te–Te contacts (~3.3 Å, substantially shorter than the sum of the van der Waals radii 4.1 Å) are found for all x , within and parallel to the sandwiches just above and below the M–M bonds. These slightly

* To whom correspondence should be addressed.

Abstract published in *Advance ACS Abstracts*, July 15, 1994.

(1) Monconduit, L.; Evain, M.; Boucher, F.; Brec, R.; Rouxel, J. *Z. Anorg. Allg. Chem.* **1992**, *616*, 1–6.

(2) Monconduit, L.; Evain, M.; Brec, R.; Rouxel, J.; Canadell, E. C. *R. Acad. Sci. Paris* **1993**, *314*, 25–34.

(3) Li, J.; Carroll, P. J. *Mater. Res. Bull.* **1992**, *27*, 1073–1081.

(4) Li, J.; Badding, M. E.; DiSalvo, F. J. *J. Alloys Comp.* **1992**, *184*, 257–263.

(5) Van der Lee, A.; Evain, M.; Monconduit, L.; Brec, R.; Van Smaalen, S. *J. Phys.: Condens. Matter.* **1993**, *6*, 933–944.

(6) Canadell, E.; Monconduit, L.; Evain, M.; Brec, R.; Rouxel, J.; Whangbo, M.-H. *Inorg. Chem.* **1993**, *32*, 10–12.

(7) Van der Lee, A.; Evain, M.; Monconduit, L.; Brec, R.; Rouxel, J.; Petříček, V. *Acta Crystallogr.* **1994**, *B50*, 119–128.

(8) Evain, M.; Monconduit, L.; Van der Lee, A.; Brec, R.; Rouxel, J.; Canadell, E. *New J. Chem.* **1994**, *18*, 215–222.

(9) Van der Lee, A.; Evain, M.; Mansuetto, M.; Monconduit, L.; Brec, R.; Rouxel, J. *J. Solid State Chem.*, in press.

(10) Liang, W.; Whangbo, M.-H.; Evain, M.; Monconduit, L.; Brec, R.; Bengel, H.; Cantow, H.-J.; Magonov, S. N. *Chem. Mater.* **1994**, *6*, 678–685.

(11) Rouxel, J.; Evain, M. *Eur. J. Solid State Inorg. Chem.*, in press.

bonding contacts imply a charge transfer from the anions to the cations.^{6,8} In addition, considerable Te–Te interactions between the [Te/M, A/Te] sandwiches (with distances as short as 3.75 Å) occur in all compounds.^{10,11} In addition, there are the curious symmetry changes with x . For $x = \frac{1}{3}$,^{1,3,4,8} $x = \frac{3}{7}$,⁵ $x = 0.3602$,⁷ and $x = 0.414$ the complete modulated structure is orthorhombic, whereas for $x = \frac{1}{2}$ ² and $x = \frac{2}{5}$ ⁹ a monoclinic symmetry is found. The latter symmetries are not caused by slight distortions of the orthorhombic structure, but correspond to shifts of either the complete sandwich ($x = \frac{1}{2}$) or the cationic contents of a sandwich over one or more basic unit cells along the c -axis ($x = \frac{2}{5}$). Since the intrasandwich arrangement is—disregarding the actual length of the modulation wave length—equivalent in all cases ($\frac{1}{3} \leq x \leq \frac{1}{2}$), one expects differences in intersandwich bonding to be responsible for the formation of these different three dimensional structures.

To reveal what might cause the symmetry change from monoclinic to orthorhombic by changing the A content by only 4% (i.e., $x = 0.40$ and $x = 0.414$), we undertook the determination of the complete modulated structure of $TaSi_{0.414}Te_2$. The refinement procedure employs the principles of the superspace group formalism.¹² In addition a new technique for the modelling of displacive modulation functions is introduced and applied.¹³ The discussion will focus on the sandwich stacking of all known compounds of the MA_xTe_2 series in relation to their symmetry and the Te–Te short contact pattern.

Experimental Section

The compound $TaSi_{0.414}Te_2$ was prepared from a mixture of the elemental powders (Ta, Fluka 99.7%; Si, Aldrich 99%; Te, Fluka 99.7%) in the ratio Ta:Si:Te = 7:3:14. The mixture was ground and loaded into a quartz tube. The tube was evacuated to 10^{-2} Torr, sealed, and placed in a programmable furnace. The temperature of the furnace was raised from room temperature to 1250 K at 100 K/h, kept fixed for 10 days, and then cooled to ambient temperature at 100 K/h.

Small, very thin platelets with a metallic luster were found in the batch. A semiquantitative SEM analysis yielded a composition $Ta_{0.83}Si_{0.63}Te_2$. It should be noted that the proportions of Ta and Si are difficult to extract from the spectrum, because of the overlap of the Ta K-emission peak and the Si L-emission peak. The title composition $TaSi_{0.414}Te_2$ is therefore based on the refinement results and structural arguments.

Weissenberg films showed a primitive orthorhombic lattice of main reflections with $a \approx 6.3$, $b \approx 14.0$, and $c \approx 3.9$ Å, thus similar to that found in the other MA_xTe_2 compounds. In addition to the main spots, a sublattice of weaker spots could be identified corresponding to a 5-fold superstructure along the c axis ($\mathbf{q} = \frac{2}{5}\mathbf{c}^*$). The crystal was then mounted on an Enraf-Nonius CAD-4F diffractometer. By an accurate centering of some strong

Table 1. Crystal Data of $TaSi_{0.414}Te_2$ and Measurement Conditions

formula	$TaSi_{0.414}Te_2$
formula weight (amu)	447.79
density (calc)	8.761
$F(000)$	731
linear absorption coefficient	511.0 cm^{-1}
crystal size	$<0.09 \times 0.004 \times 0.09 \text{ cm}^3$
maximum correction	12.9
minimum correction	1.5
superspace group	$Pnma(00\gamma)s00$
basic unit cell	$a = 6.318(1)$ Å
	$b = 14.031(2)$ Å
	$c = 3.8552(7)$ Å
	$\text{vol} = 341.8(1)$ Å ³
modulation vector	$\mathbf{q} = 0.4144(10)\mathbf{c}^*$
diffractometer	CAD-4F
temperature	295 K
radiation	Mo K–L _{2,3}
scan mode	$\omega/(2\theta)$
<hr/>	
	h_{\min} h_{\max} k_{\min} k_{\max} l_{\min} l_{\max}
$hklmn$ range	main 0 10 -24 24 0 6
	1st order 0 8 -19 19 0 5
	2nd order 0 8 0 19 0 6
	3rd order 0 8 0 19 0 6
	4th order 0 8 0 19 0 7
	6th order 0 6 0 13 0 6
	standard reflections (2300), (2300), (3010) every hour

Table 2. Reflection Statistics^a

	N_1	N_2	$\langle I \rangle$	$\langle I/\sigma(I) \rangle$
main	1782	1100	100.0	14.7
1st order	1886	1270	41.4	13.9
2nd order	927	311	9.8	6.8
3rd order	823	179	5.3	4.7
4th order	739	103	11.1	7.1
6th order	199	26	6.4	5.3
all	6356	2989	56.1	12.6

^a N_1 is the total number of data collected, N_2 is the number of data with $I \geq 2.5\sigma(I)$. $\langle I \rangle$ and $\langle I/\sigma(I) \rangle$ are calculated for the N_2 data. The values in the column for $\langle I \rangle$ are normalized to 100.0 for the strongest reflection class. The internal R factor for averaging in Laue class mmm is 0.039: 1859 unique reflections are left for refinement.

first-order satellites, it was detected that the \mathbf{q} vector is actually incommensurate with the underlying main lattice. The final length of the \mathbf{q} vector was least-squares refined with the program U-FIT¹⁴ from the setting angles of 32 first-order satellite reflections: $\mathbf{q} = \gamma\mathbf{c}^* = 0.4144(10)\mathbf{c}^*$. It is noted that γ is equal to the rational value $\gamma' = \frac{5}{12}$ within 3 standard deviations.

Data collection of main reflections was subsequently performed, followed by that of satellite reflections up to the sixth order. Table 1 compiles the recording conditions; Table 2 contains some reflection statistics. The measured intensities were corrected for a small drift variation monitored by three reference reflections (<1%), for Lorentz and polarization effects, and for absorption using some programs of the XTAL system.¹⁵ The absorption correction is very sensitive to an accurate determination of the thickness of the platelet. It was optimized by repeating the final refinements with data sets obtained with slightly different thicknesses until a minimal R value was reached.

Symmetry-related reflections were averaged according to Laue symmetry mmm , because the superspace

(12) See for a technical treatment of superspace group theory, e.g., §9.8 in *International Tables for Crystallography* Vol. C; Wilson, A. J. C., Ed.; Kluwer Academic Publishers: Dordrecht, 1992. A more descriptive treatment is given by, e.g.: Janssen, T.; Janner, A. *Adv. Phys.* 1987, 36, 519–624.

(13) Petříček, V.; Van der Lee, A. *Acta Crystallogr.*, submitted.

(14) Evain, M. U-FIT: A cell parameter refinement program, 1992, Institut des Matériaux de Nantes, Nantes, France.

(15) Hall, S. R., Flack, H. D., Stewart, J. M., Eds. Xtal3.2 Reference Manual, 1992, Universities of Western Australia, Geneva, and Maryland.

group describing the modulated structure was assumed to be similar to that of $\text{TaSi}_{0.360}\text{Te}_2$.⁷ The systematic absent reflections found in the diffraction pattern were in accordance with this assumption. The nonlinear least-squares refinements (described in the next paragraph) were performed with the JANA93 computing system.¹⁶ The scattering factors for neutral atoms and the anomalous dispersion correction were taken from the International Tables for X-ray Crystallography.¹⁷ All refinements were based on $|F_{\text{obs}}|$ and performed in a full-matrix mode, using unit weights for all reflections.

Structure Refinement. The symmetry of incommensurately and long-period modulated structures is usually described by $(3 + n)\text{D}$ superspace groups¹² where n ($1 \leq n \leq 3$) gives the number of modulation wave vectors necessary to obtain an integer indexing of the diffraction pattern. In the present case $n = 1$; the satellite reflections along \mathbf{c}^* are indexed by an integer m in addition to the normal set of Miller indices (hkl) according to

$$\mathbf{H} = h\mathbf{a}^* + k\mathbf{b}^* + l\mathbf{c}^* + m\mathbf{q}$$

with \mathbf{H} the diffraction vector; \mathbf{a}^* , \mathbf{b}^* , and \mathbf{c}^* the reciprocal axes, and \mathbf{q} the modulation wave vector. The symmetry of the modulated structure of $\text{TaSi}_{0.414}\text{Te}_2$ is, like that of $\text{TaSi}_{0.360}\text{Te}_2$, described by the $(3 + 1)\text{D}$ superspace group $Pnma(00\gamma)s00$ with $\gamma = 0.414$. This can be deduced from the observed systematic extinctions for the reflections $(hklm)$.¹²

The determination and refinement of an incommensurately modulated structure is usually a two-step procedure. First, the “average” structure is refined using the main reflections $(hkl0)$ only, and second, the modulation is determined using the main reflections and the satellite reflections. The modulations of the atomic coordinates and/or the site occupancy probability are mostly described by Fourier series:

$$\begin{aligned} \mathbf{r}^\nu(\bar{x}_4) &= \mathbf{r}_0^\nu + \sum_{n=1}^{n_{\max}} (\mathbf{u}_{s,n}^\nu \sin(2\pi n \bar{x}_4) + \mathbf{u}_{c,n}^\nu \cos(2\pi n \bar{x}_4)) \\ \mathbf{P}^\nu(\bar{x}_4) &= \mathbf{P}_0^\nu + \sum_{n=1}^{n_{\max}} (\mathbf{P}_{s,n}^\nu \sin(2\pi n \bar{x}_4) + \mathbf{P}_{c,n}^\nu \cos(2\pi n \bar{x}_4)) \end{aligned}$$

where \mathbf{r}_0^ν and P_0^ν are the basic structure coordinate and the site occupancy probability, respectively, for atom ν . The number of harmonics in the refinement, n_{\max} , is usually equal to the highest order of the observed satellite reflections. The argument of the modulation function, \bar{x}_4 , is defined as follows: $\bar{x}_4 = t + \mathbf{q} \cdot \mathbf{r}_{0,\mathbf{L}}^\nu = t + \mathbf{q} \cdot (\mathbf{r}_0^\nu + \mathbf{L})$, with t the global phase of the modulation wave ($t = 0$ is used for the refinements in the present work), and \mathbf{L} a basic structure lattice translation. The goal of a modulated structure determination is to find the Fourier amplitudes $\mathbf{u}_{s,n}^\nu = (A_{x,s,n}^\nu A_{y,s,n}^\nu A_{z,s,n}^\nu)$, $\mathbf{u}_{c,n}^\nu = (A_{x,c,n}^\nu A_{y,c,n}^\nu A_{z,c,n}^\nu)$, and $P_{s,n}^\nu$ and $P_{c,n}^\nu$. We have shown before that the occupancy modulations is quite often better modeled by a crenel function than by a Fourier

(16) Petříček, V. JANA93: programs for modulated and composite crystals, 1993, Institute of Physics, Praha, Czech Republic.

(17) Cromer, D. T.; Waber, J. T. In *International Tables for X-ray Crystallography*; Ibers, J. A., Hamilton, W. C., Eds.; Kynoch Press: Birmingham, England, 1974; Vol. IV, pp 72–98. Cromer, D. T. *Ibid.* pp 149–150.

series.⁷ This function is defined by

$$\mathbf{P}^\nu(\bar{x}_4) = H(\bar{x}_4 - \bar{x}_{4,l}^\nu) - H(\bar{x}_4 - \bar{x}_{4,r}^\nu)$$

where $H(x) = 0$ if $x < 0$, and $H(x) = 1$ if $x > 0$; $\bar{x}_{4,l}^\nu = \bar{x}_{4,0}^\nu - \Delta^\nu/2$ and $\bar{x}_{4,r}^\nu = \bar{x}_{4,0}^\nu + \Delta^\nu/2$; Δ^ν , the width of the step, is just equal to the average occupation probability P_0^ν , and $\bar{x}_{4,0}^\nu$ represents the center of the step.

It is obvious that interatomic distances modulate as well and that there is, because of the incommensurability, an infinite number of such distances for each pair of atoms of the average structure. Therefore, the information concerning interatomic distances in a modulated structure is best presented by a plot of distance versus t in the interval [0;1]; in this way all distances present in the modulated structure are given at the same time (see Figures 3 and 4).

The refinements proceeded along the same lines as that for $\text{TaSi}_{0.360}\text{Te}_2$ with one major modification. Here we give only a brief summary and a short description of the modification; for details we refer to the paper on $\text{TaSi}_{0.360}\text{Te}_2$.⁷

The parameters of the average structure, keeping the Debye–Waller parameters isotropic, refined to a final R factor of 0.18 ($wR = 0.18$). The refinement of the modulated structure was initiated with low-order Fourier components for the modeling of the displacive modulation waves of all atoms and with step functions for the occupational modulation waves of the cations. Only one step function parameter was refined; the centers $\bar{x}_{4,0}^\nu$ of Ta(2) and Si were constrained to that of Ta(1) in such a way that the occupancy of the cationic sites of the basic unit cell would never lead to unrealistic short distances. The equation to fulfill this requirement is

$$\bar{x}_{4,0}^\nu = \bar{x}_{4,0}^{\text{Ta}(1)} + \gamma(z^\nu - z^{\text{Ta}(1)}) - 0.5 \quad \nu = \text{Ta}(2), \text{Si}(1)$$

Refinements performed in this way suffered from heavy correlations between Fourier amplitudes of different order. Moreover, the refinement of the displacive parameters of Si was very unstable, causing shifts to unreasonable values without any physical meaning.

This problem finds its origin in the occupational nature of the modulation. The displacive modulation functions are not properly defined for those intervals of the phase of the modulation where the occupational modulation functions are exactly zero. In other words, the distinct harmonics of the displacive modulation functions are no longer orthogonal but become linearly dependent. The obvious remedy for this problem is a reorthogonalization of the displacive modulation functions over the interval where the occupational modulation functions take the value one. The Fourier amplitudes $\mathbf{u}_{s,n}^{\nu,\text{ort}}$ and $\mathbf{u}_{c,n}^{\nu,\text{ort}}$ of the orthogonalized functions can be subsequently used in the least-squares matrix. The details of the implementation of this orthogonalization procedure will be described in a forthcoming paper.¹³

Using the new Fourier amplitudes, the majority of the heavy correlations vanished, and the Si position remained reasonably stable. The refinement results are compiled in Table 3. Table 3 also contains the Fourier amplitudes of the original functions corresponding to the new ones obtained from the refinement. The former are easier to manipulate than the latter, for instance

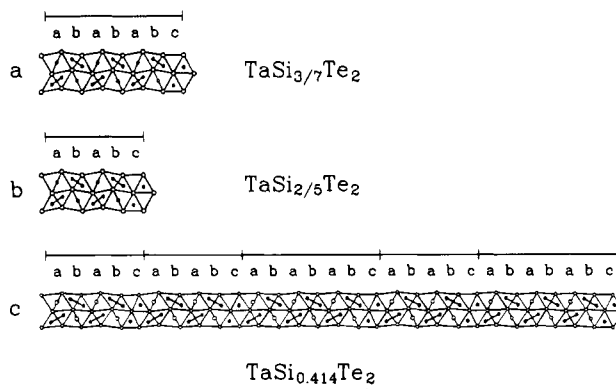


Figure 2. Ordering pattern of $[TaSi_{3/7}Te_2]$ (a) and $[TaSi_{2/5}Te_2]$ (b) motifs in one $[TaSi_{0.414}Te_2]$ sandwich (c) along the running direction of the modulation wave.

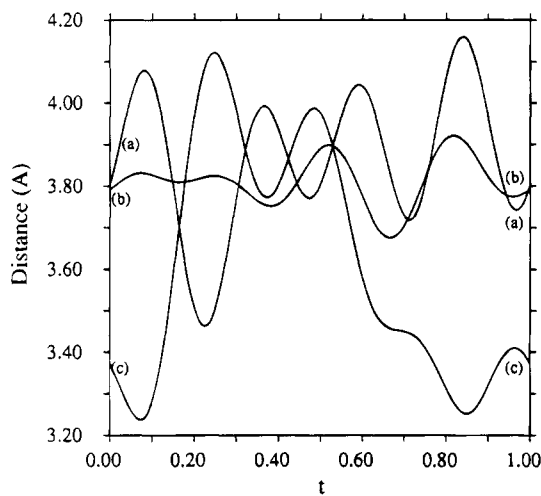


Figure 3. Te–Te distances (\AA) parallel to the $[TaSi_{0.414}Te_2]$ sandwich as a function of the phase t of the modulation wave:

	$\langle d \rangle$	d_{\min}	d_{\max}
(a)	3.868	3.462	4.159
(b)	3.811	3.675	3.922
(c)	3.605	3.237	4.121

for the calculation of atomic positions and bond distances. Note that the Fourier amplitudes of the non-orthogonalized functions sometimes take very large values, and that the “mean”, i.e. $\mathbf{u}_{c,0}''$, does not correspond to the average coordinates. They are just the zeroth-order term in the Fourier expansion.

In the Experimental Section it was already mentioned that the wave vector is, within 3 standard deviations, commensurate with the underlying basic lattice. To test the possible commensurability, we have performed refinements using the commensurate wave vector. Indeed, using the refinement results of Table 3 one finds a quasi-12-fold periodicity along the c -axis (*vide infra*). The 3D symmetry of this twelve-fold superstructure is $P2_1/m$. This is in perfect agreement with predictions in a previous paper⁵ that the n -glide plane that is present in $Pmna$ cannot be retained in an even-fold superstructure. The three possible symmetries for an n -fold (n even) superstructure of the parent superspace group $Pnma(00\gamma)s00$ are $P2_1/m$ for global phases $t_0 = 0$ ($\text{mod } 1/2n$), $P2_1ma$ for $t_0 = 1/4n$ ($\text{mod } 1/2n$), and Pm otherwise. To perform the refinement of this monoclinic superstructure the superspace group $P2_1/m(00\gamma)$ was chosen. For the commensurate case the same problems related to the orthogonalization of the displacive modu-

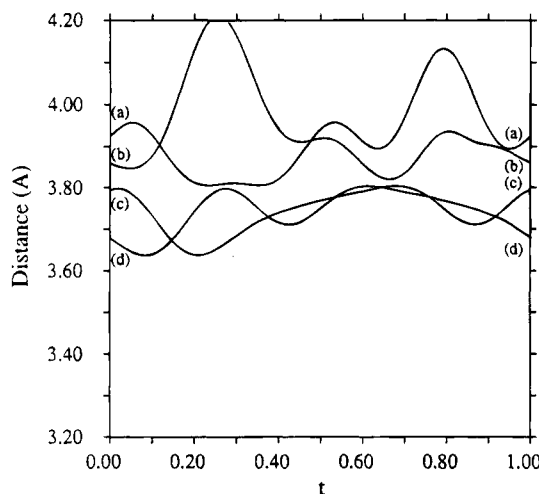


Figure 4. Te–Te distances (\AA) perpendicular to the $[TaSi_{0.414}Te_2]$ sandwiches as a function of the phase t of the modulation wave: (a) and (b) interlayer, (c) and (d) intralayer:

	$\langle d \rangle$	d_{\min}	d_{\max}
(a)	3.919	3.806	4.133
(b)	3.943	3.820	4.210
(c)	3.742	3.638	3.804
(d)	3.742	3.638	3.804

lation functions as for the incommensurate case occur, but now for discrete functions instead of continuous ones. A discrete version of the orthogonalization procedure was developed and applied in the least-squares refinement. Note that the number of atoms, and accordingly the number of parameters, is doubled compared to the incommensurate case. The final R factors for this commensurate model are significantly higher than the incommensurate model, especially if the extra number of variables is taken into account (Table 4). However, if the structure is truly incommensurate with γ close to the rational value $5/12$, a significant noncoherent overlap of especially the high-order satellite reflections is expected. This effect is not taken into account in the current approach and probably causes the large partial R factors for the high-order satellites. Thus, with the present crystallographic method it is not easy to decide between commensurateness and incommensurateness. However, complementary studies by means of AFM and STM imaging techniques do suggest an incommensurate modulation rather than a commensurate one.¹⁸ From a crystallographic point of view the two models do not differ much.

Discussion

Structural Features. The $TaSi_{0.414}Te_2$ structure derives from a hypothetical MoS_2 -type $TaTe_2$ structure, as do all MA_xTe_2 structures ($M = Nb, Ta; A = Si, Ge; 1/3 \leq x \leq 1/2$). The insertion of silicon atoms within the $[Te/Ta/Te]$ sandwich is concomitant with a pairing of some Ta cations, the number of pairs matching the number of silicon atoms introduced according to the formulation $(M_2)_xM_{1-2x}A_xTe_2$ ($1/3 \leq x \leq 1/2$).

It has been shown⁷ that the wave vector component $\gamma = 0.4144(10)$ is directly related to the A-atom content ($\gamma = x$), and thus the title formula $TaSi_{0.414}Te_2$. As

(18) Bengel, H.; Cantow, H.-J.; Magonov, S. N.; Monconduit, L.; Evain, M.; Liang, W.; Whangbo, M.-H. *Chem. Mater.*, in press.

Table 3. Final Values for the Amplitudes of the Displacive Modulation Functions^a

	<i>n</i>	$A_{x,s,n}^v$	$A_{y,s,n}^v$	$A_{z,s,n}^v$	$A_{x,c,n}^v$	$A_{y,c,n}^v$	$A_{z,c,n}^v$
Ta(1)	0				0.3163(8)	0.25	-0.047(3)
	1	-0.0075(5) -0.0438	0.0	-0.0270(8) 0.0850	0.0004(22) 0.0292	0.0	0.0391 -0.0429(3)
	2	0.006(2) 0.0291	0.0	-0.010(4) -0.0926	-0.0004(8) -0.0026	0.0	0.0034(9) 0.0041
	3	-0.002(2) -0.0057	0.0	0.009(3) 0.0249	-0.0007(10) -0.0042	0.0	0.0045(6) 0.0277
					0.020(2) -0.4616	0.25	-0.051(5) 0.0268
					-0.017(4) 0.0955	0.0	0.038(8) 0.3020
Ta(2)	0				-0.025(7) -0.0536	0.002(1) -0.0048	0.0
	1	-0.0015(8) 0.5517	0.0	0.020(3) 0.0955	0.0020(2) 0.0630	0.0	-0.012(1) 0.2706
	2	0.016(3) 0.3851	0.0	-0.007(2) -0.0886	0.0020(2) 0.0630	0.0	0.0026(4) 0.0821
	3	0.006(1) 0.0631	0.0		0.424(4) 0.4028	0.25	0.270(7) 0.2948
					0.034(7) 0.0456	-0.006(6) -0.0270	0.010(6) 0.0454
Si	0				0.1688(3) 0.1670(2)	0.1167(1) 0.11676(8)	0.4739(4) 0.4771(3)
	1	-0.005(5) -0.0033	0.0		0.0060(7) 0.0224(2)	-0.0014(2)	-0.0113(7)
Te	0				-0.0023(9) -0.0011(6)	-0.0019(6) 0.0050(7)	0.0012(3) 0.0004(4)
	1	0.0249(4)	0.0010(2)	0.0060(7)	0.0104(9)	0.0002(10)	0.0002(10)
	2	0.0085(6)	-0.0004(4)	-0.0023(9)			
	3	-0.0099(7)	0.0011(6)	-0.0028(1)			
	4	0.0048(9)	0.0002(10)		0.0088(8)	-0.0003(7)	-0.002(1)

^a The first line for each order for each atom, except for Te, gives the orthogonalized Fourier amplitudes $\mathbf{u}_{s,n}^{v,\text{ort}}$ and $\mathbf{u}_{c,n}^{v,\text{ort}}$ that result from the refinement; the second line gives the corresponding nonorthogonalized amplitudes. The latter can be used to calculate atomic coordinates and bond distances according to

$$\mathbf{r}^v(\bar{x}_4) = \sum_{n=0}^{n_{\max}} [\mathbf{u}_{s,n}^v \sin(2\pi n \bar{x}_4) + \mathbf{u}_{c,n}^v \cos(2\pi n \bar{x}_4)]$$

where *v* counts the independent atoms in the basic unit cell. The argument of the modulation function has been defined as follows: $\bar{x}_4 = t + \mathbf{q}\mathbf{r}_{0,L}^v = t + \mathbf{q}(\mathbf{r}_0^v + \mathbf{L})$, with *t* the global phase of the modulation wave (*t* = 0 is used in the present work), \mathbf{L} a basic structure lattice translation; and $\mathbf{u}_{s,n}^v = (A_{x,s,n}^v, A_{y,s,n}^v, A_{z,s,n}^v)$, $\mathbf{u}_{c,n}^v = (A_{x,c,n}^v, A_{y,c,n}^v, A_{z,c,n}^v)$. The occupational modulation functions are defined as

$$P^v(\bar{x}_4) = H(\bar{x}_4 - \bar{x}_{4,l}) - H(\bar{x}_4 - \bar{x}_{4,r})$$

where $H(x) = 0$ if $x < 0$ and $H(x) = 1$ if $x > 0$; $\bar{x}_{4,l}^v = \bar{x}_{4,0}^v - \Delta^v/2$ and $\bar{x}_{4,r}^v = \bar{x}_{4,0}^v + \Delta^v/2$; Δ^v the width of the step, is just equal to the average occupation probability and $\bar{x}_{4,0}^v$ represents the center of the step. As explained in the text, only $\bar{x}_{4,0}^{\text{Ta}(1)}$ was refined: $\bar{x}_{4,0}^{\text{Ta}(1)} = 0.868(8)$.

Table 4. Final Reliability Factors for the Incommensurate and the Commensurate Model^a

	<i>Pnma</i> (00γ)s00		<i>P2</i> ₁ /m(α0γ) α = 0;	
	γ = 0.4144	γ = 5/12	R	wR
main	0.054	0.055	0.062	0.062
1st order	0.113	0.149	0.144	0.182
2nd order	0.164	0.189	0.196	0.221
3rd order	0.325	0.412	0.318	0.385
4th, 6th order	0.527	0.599	0.401	0.456
overall	0.111	0.126	0.126	0.136

^a The numbers of unique reflections and independent parameters for the incommensurate model are 1859 and 74, respectively, and for the commensurate model 1989 and 140, respectively.

already stated, γ is close to the rational value $5/12$ from which one calculates the following formula $(\text{Ta}_2)_5\text{Ta}_2\text{Si}_5\text{Te}_{24}$. This last formula can be decomposed as a sum of two simpler terms: $(\text{Ta}_2)_3\text{TaSi}_3\text{Te}_{14}$ ($\text{TaSi}_{3/7}\text{Te}_2$) and $(\text{Ta}_2)_2\text{TaSi}_2\text{Te}_{10}$ ($\text{TaSi}_{2/5}\text{Te}_2$) that contain only one lone Ta per formula (i.e., one lone Ta ribbon per sandwich per unit cell). Therefore one expects the sandwich of the $\text{TaSi}_{0.414}\text{Te}_2$ structure to be, in a first approximation, a succession of $\text{TaSi}_{3/7}\text{Te}_2$ and $\text{TaSi}_{2/5}\text{Te}_2$ in-slab basic units. In Figure 2 two such building units (2a and 2b) are presented. In the same figure (2c), a fraction of the unit sequence of the real structure is also shown. One easily notices the regular succession of the two building units, except on the left-hand side of the picture where

two $\text{TaSi}_{2/5}\text{Te}_2$ units are consecutive. This is in agreement with the $\text{TaSi}_{0.414}\text{Te}_2$ formulation (that is, the wave vector component value $\gamma = 0.414$) that indicates that the structure is very close to that of $\text{TaSi}_{5/12}\text{Te}_2$ but richer in $\text{TaSi}_{2/5}\text{Te}_2$ units than in $\text{TaSi}_{3/7}\text{Te}_2$ structural motifs ($2/5 < \gamma < 5/12 < 3/7$).

In Figures 3 and 4, plots of Te–Te interatomic distances versus the $t = \bar{x}_4 - \bar{q}\bar{r}_0^v$ phase of the modulation wave are presented. The main features of such distance variations (d_{\min} , d_{\max} , and $\langle d \rangle$) are gathered in the figure captions. The most interesting distance is the Te–Te intraslab distance given in Figure 3c. That distance covers three different situations: (i) the Te–Te contacts above the Ta–Ta bonds (that is, the contacts forming an edge of the rectangular faces joining the two trigonal prisms containing the Ta atoms of the Ta–Ta pairs), (ii) the in-plane Te–Te edges on top of the Si atoms (that is, part of the rectangular faces encompassing the Si atoms), and (iii) the Te–Te edges at the limit between two prisms of the [TaTe₂] like ribbons (that is, between a prism with a lone Ta and an empty prism). According to the title formula, one expects the various probabilities for the distance to match the three different situations to be 0.414, 0.414, and 0.172, respectively. In the distance plot as a function of *t*, the probability of finding a distance is directly proportional to the interval on the *t* axis to which it corresponds. One easily notices the short in-

plane Te–Te contacts ($3.24 < d < 3.45 \text{ \AA}$; $t < 0.12$ and $t > 0.71$) of the first case. The average distance in this range (3.33 \AA) is in perfect agreement with the usual distance found in all MA_xTe_2 structures (for instance 3.35 \AA in $TaSi_{1/3}Te_2$).⁸ That distance, substantially shorter than the sum of the van der Waals radii (4.1 \AA) corresponds to bonding contacts.^{6,8} These are referenced as type I short contacts hereafter. On the same curve (c of Figure 3), the lengthening of the Te–Te contact ($3.70 < d < 4.12 \text{ \AA}$; $0.16 < t < 0.57$) coincides with the second situation, i.e., the surrounding of the Si atoms. Here again, the average distance, 3.92 \AA , is very similar to what is found in $TaSi_{1/3}Te_2$ (3.96 \AA). The remaining intervals, $0.12 < t < 0.16$ and $0.57 < t < 0.71$, give the distance range $3.45 < d < 3.70 \text{ \AA}$ ($d_{\text{avg}} = 3.51 \text{ \AA}$) for the last Te–Te contact type, within the $[TaTe_2]$ like ribbons. Again, it is in perfect agreement with the equivalent distance in $TaSi_{1/3}Te_2$ (3.54 \AA). The other distance fluctuations presented in Figures 3 and 4 are not easily interpretable. Let us just mention the shortest interlayer Te–Te contacts of 3.8 \AA (Figure 4a). Those contacts through the van der Waals gap (referenced as type II short contacts) are a constant of the MA_xTe_2 structures (3.84 \AA in $TaSi_{1/3}Te_2$) although their character gradually shift from antibonding when $x = 1/2$ to bonding when $x = 1/3$.¹¹ They are the signature of the sandwich–sandwich interaction and could be the clue to the understanding of the stacking rules in the MA_xTe_2 series, which we will now consider.

Stacking Rules in the MA_xTe_2 Series. To understand the stacking of the $[MA_xTe_2]$ layers, let us first analyze the cases of the end members of the series: $MA_{1/3}Te_2$ and $MA_{1/2}Te_2$. In Figure 5 (a and b) is presented in a schematic way the projection of one layer and of two layers, respectively, of such compounds. To untangle the projection view of the layer stacking, the Te atoms involved in type I or type II short contacts (vide supra) are separated out in Figure 5c. Type I contacts always occur in pairs, in an “eclipsed”, parallel arrangement (the $\text{Te}(I-II-I)$ units) or an “alternate”, parallel way (the $\text{Te}(I-I)$ units). A type II short contact always links the two pairs of a $\text{Te}(I-II-I)$ unit (thus the $\text{Te}(I-II-I)$ label). An alternative picture is that presented in Figure 5d where the metal atoms have been isolated. To the $\text{Te}(I-II-I)$ and the $\text{Te}(I-I)$ units correspond easily identifiable M_2 pair motifs labeled $M(I-II-I)$ and $M(I-I)$, respectively. Notice that, since the type II Te–Te short contacts are always linked with the $\text{Te}(I-II-I)$ units in a one to one correspondence, they are associated to the $M(I-II-I)$ motifs as well. Finally, in Figure 5e both the Te atoms, the M atoms, and the links already included in Figure 5c,d are drawn. It is worth noticing that each Te atom of a $\text{Te}(I-II-I)$ unit is just on top of an M atom (paired or unpaired) of the neighboring sandwich but that each Te atom of the $\text{Te}(I-I)$ group faces an empty prism of the adjacent sandwich. The type II Te–Te short contacts across the van der Waals gap always occur when there is a perfect matching between the type I Te–Te short contacts and the metals of the adjacent sandwich. This seems to be the requisite feature for a proper anchorage of one sandwich to another.

The various stacking features observed for the end members of the MA_xTe_2 series, that is, $MA_{1/3}Te_2$ and $MA_{1/2}Te_2$, apply to all members known so far, i.e., for

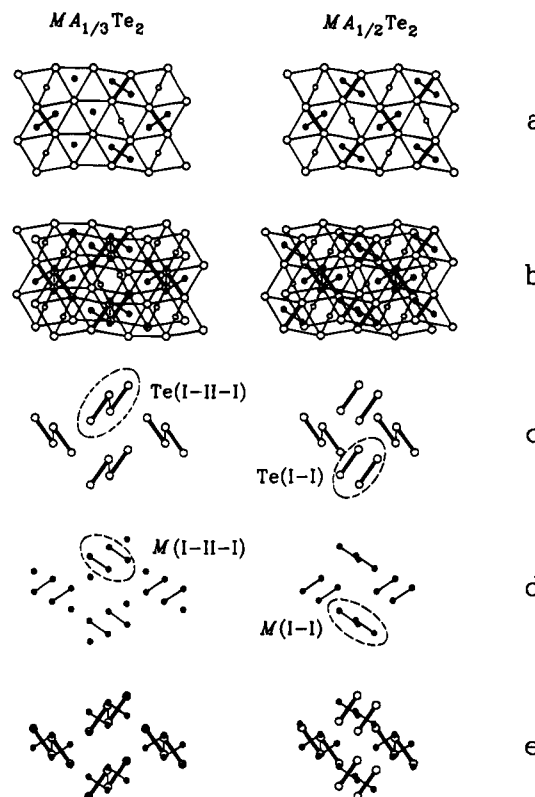


Figure 5. Stacking principles in the MA_xTe_2 series exemplified by the two end members of the family: $MA_{1/3}Te_2$ and $MA_{1/2}Te_2$. (a and b) projections of one and two MA_xTe_2 sandwiches, respectively; (c) type I (within the sandwiches, thick line) and type II (in between the sandwiches, thin line) short Te–Te contacts, isolated from (b), that occur in two different motifs: $\text{Te}(I-II-I)$ and $\text{Te}(I-I)$; (d) M atoms, isolated from (b), with M_2 pairs and lone M atoms. A one to one correspondence is made between the M_2 pairs pattern and the Te–Te short contacts in (c), thus the labelling of the M_2 pairs motifs: $M(I-II-I)$ and $M(I-I)$; (e) superposition of the (c) and (d) sandwich projection fragments showing the perfect matching between the Te atoms of the $\text{Te}(I-II-I)$ motifs and the M atoms of the neighbor sandwich and the absence of M atoms on top, or below, the Te atoms of the $\text{Te}(I-I)$ motifs.

MA_xTe_2 $x = 1/2, 3/7, 0.414, 2/5, 0.360$, and $1/3$ (the $4/11$ case is not taken into account since it differs in building units and slab pattern¹⁹). The fact that all type I Te–Te short contacts couple, in projection, in only two ways, either $\text{Te}(I-II-I)$ or $\text{Te}(I-I)$, was checked for each structure, irrespective of the value of γ of each phase (see Figure 6 for a schematic view of the alternate projection with the $M(I-II-I)$ and $M(I-I)$ motifs). From that analysis, a formula giving the number of $\text{Te}(I-II-I)$ and $\text{Te}(I-I)$ groups per MA_xTe_2 formula as a function of x is established:

$$n_{\text{Te}(I-II-I)} = (1 - x)/2 \quad n_{\text{Te}(I-I)} = (3x - 1)/2$$

An extended formulation can then be proposed for the MA_xTe_2 compounds: $(M_2)_x A_x [Te_2]_{(1-x)} [Te_2]_{(3x-1)} M_{1-2x} Te_{2(1-2x)}$ ($1/3 \leq x \leq 1/2$) where the different Te atoms refer to Te in the $\text{Te}(I-II-I)$ groups, Te in the $\text{Te}(I-I)$ motifs, and other Te not involved in the type I short contacts, respectively (the brackets denote type I short Te–Te contacts). This formula gives a good insight into the building principle of the structure. For instance, for x

(19) Van der Lee, A.; Evain, M.; Monconduit, L.; Brec, R.; Petříček, V. *Inorg. Chem.*, in press.

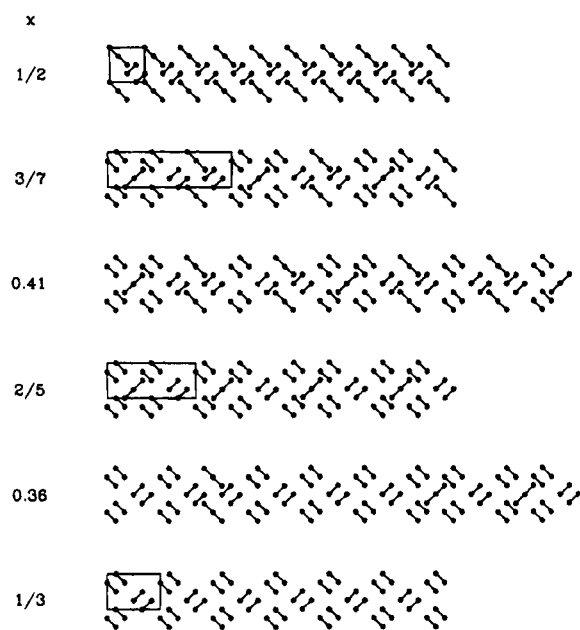


Figure 6. Stacking of two sandwiches as a function of x in the MA_xTe_2 series as a projection of the M_2 pairs. Boxes represent the superstructure unit cells for the commensurate cases. The representation is similar to that given in Figure 5d.

$= \frac{1}{2}$ it reduces to $(\text{M}_2)_{1/2}\text{A}_{1/2}[\text{Te}_2]_{1/2}[\text{Te}_2]_{1/2}\text{M}_0\text{Te}_0$. This gives useful information: (1) the wave vector component along the running direction is $\frac{1}{2}$, (2) there are no lone M atoms, (3) all Te atoms are engaged in type I short contacts, (4) the $\text{Te}(\text{I}-\text{II}-\text{I})$ and $\text{Te}(\text{I}-\text{I})$ motifs are in equal proportion, and (5) one quarter of the Te atoms participates in the type II intersandwich short contacts. Similarly, for $x = \frac{2}{5}$, one obtains $(\text{M}_2)_{2/5}\text{A}_{2/5}[\text{Te}_2]_{3/5}[\text{Te}_2]_{1/5}\text{M}_{1/5}\text{Te}_{2/5}$. This indicates for instance that 30% of the Te atoms are engaged in the type II short contacts through the van der Waals gap.

Since the $\text{Te}(\text{I}-\text{II}-\text{I})$ and $\text{Te}(\text{I}-\text{I})$ (or equivalently $\text{M}(\text{I}-\text{II}-\text{I})$ and $\text{M}(\text{I}-\text{I})$) patterns are the preferential motifs found in the MA_xTe_2 series, one can easily predict the positioning of one sandwich on top of the adjacent one and, consequently, the symmetry of the modulated structure. For instance, the monoclinic symmetry of $\text{MA}_{2/5}\text{Te}_2$ can be explained by considering the five possible stackings of two sandwiches in the $\text{MA}_{2/5}\text{Te}_2$ structure (see Figure 7). It is seen that in the usual $Pnma$ stacking (Figure 7a) the M pattern does not match the expected arrangement. By shifting the second slab over either one or four basic units in the c direction (Figure 7b), one obtains the experimental $\text{M}(\text{I}-\text{II}-\text{I})$ and $\text{M}(\text{I}-\text{I})$ arrangements.⁹ Shifting over either two or three basic units (Figure 7c) yields other, nonobserved $\text{M}(\text{I}-\text{II}-\text{I})$ and $\text{M}(\text{I}-\text{I})$ arrangements. Although the stacking rules give the relative position of two neighboring sandwiches, they cannot predict the final space group symmetries since they cannot differentiate between polytypes as we will now discuss.

Stacking and Symmetry. Let us consider again the $\text{MA}_{2/5}\text{Te}_2$ stacking example. Starting with one $[\text{MA}_{2/5}\text{Te}_2]$ layer, one has two possibilities for the positioning of the next sandwich (1 and 4 unit shifts in Figure 7). Since, at this stage, both solutions are equivalent, let us choose the one unit shift. For the third sandwich, one has again two possibilities. Now the choice is important since it will lead to two different monoclinic symmetries

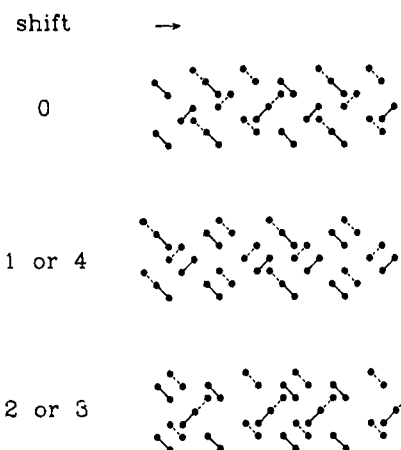


Figure 7. Stacking of two sandwiches in the $\text{MA}_{2/5}\text{Te}_2$ structure as a function of the basic unit shift of the second slab (arrow). The experimental $\text{M}(\text{I}-\text{II}-\text{I})$ and $\text{M}(\text{I}-\text{I})$ arrangements are obtained by a shift of either one or four basic units in the c direction, starting from the usual $Pnma$ stacking (zero shift).

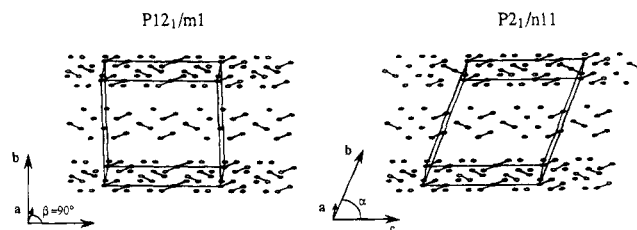


Figure 8. Schematic illustration of the two polytypes possible for the $\text{MA}_{2/5}\text{Te}_2$ compounds. The filled circles give the actual M atom positions; the open circles correspond to the projection of the middle plane M atoms onto the adjacent planes, perpendicularly to the planes. Such projections show the validity of the stacking rules for both polytypes, that is, the preferential formation of $\text{M}(\text{I}-\text{II}-\text{I})$ and $\text{M}(\text{I}-\text{I})$ arrangements.

as shown in a schematic way in Figure 8. A four-unit shift can be chosen which gives a monoclinic symmetry (space group $P12_1/m1$, $\alpha = \gamma = 90^\circ$ and $\beta \approx 90^\circ$), but with a pseudoorthorhombic lattice. On the other hand, a one-unit shift leads to a different monoclinic symmetry (space group $P2_1/n11$, $\beta = \gamma = 90^\circ$ and $\alpha \neq 90^\circ$), now with a monoclinic lattice. The latter case corresponds to the observed one. The structure turns out to be twinned, one domain corresponding to a shift of 1 unit of the second sandwich with respect to the first one, the other domain to a shift of 4 units.⁹ In Figure 8, a projection (open circle) of the middle sandwich, perpendicularly to the sandwich plane, onto the upper and lower sandwiches shows that the stacking rules are fulfilled (we only have $\text{M}(\text{I}-\text{II}-\text{I})$ and $\text{M}(\text{I}-\text{I})$ patterns) for the two polytypes.

Because of the similarity of the basic lattices of all MA_xTe_2 compounds, the only difference being the magnitude of the modulation wave vector, one expects one parent superspace group for all phases. Indeed, $Pnma(00\gamma)s00$ is found for $\gamma = \frac{1}{3}, 0.360, \frac{3}{7}$, and 0.414. The supercell symmetry of the phases $\gamma = \frac{1}{3}$ and $\gamma = \frac{3}{7}$ is $Pnma$. The supersymmetry of $\text{MA}_{2/5}\text{Te}_2$ ($\gamma = \frac{2}{5}$) would be characterized by $Pnma(00n_1/n_2)s00$ if its supercell symmetry would be $P12_1/m1$.⁵ In general, one can show that the supercell symmetry of phases with parent superspace group $Pnma(00n_1/n_2)s00$ is necessarily lower than $Pnma$, if $n_1 + n_2 = \text{even}$, e.g., $P12_1/m1$, but not $P2_1/n11$. Since the latter space group is the

correct space group of the observed $MA_{2/5}Te_2$ phase, its superspace group symmetry cannot be $Pnma(00n_1/n_2)s00$, but instead $P2_1/n(0\beta\gamma)$. Thus, $Pnma(00n_1/n_2)s00$ and $P2_1/n(0\beta\gamma)$ describe the symmetry of two polytypes.

A similar situation is encountered for the $NbSi_{1/2}Te_2$ structure. Indeed, in that structure the stacking rules are fulfilled but the 3D space group ($P112_1/c$, $\gamma \neq 90^\circ$) does not belong to the superspace group $Pnma(00n_1/n_2)s00$.^{2,20} Once again, a polytype is obtained, different from that observed for $NbGe_{2/5}Te_2$, that implies a different cation stacking mode, an (AA)(BB)(CC) mode instead of the (AA)(BB) mode which prevails in most MA_xTe_2 phases.

In conclusion, superspace group theory fails to unify the symmetries of all modulated phases of the homologous MA_xTe_2 series to one parent superspace group. The underlying reason is that it cannot take into account a possible polytypism.

Concluding Remarks

The determination of the complete modulated structure of $TaSi_{0.414}Te_2$ confirms the building principles of a sandwich of an incommensurate MA_xTe_2 structure,⁷ that is, the quasi periodic succession of two motifs that constitute the repeat unit of the two commensurate structure $MA_{(1+n)/(3+2n)}Te_2$ and $MA_{(1+(1+n))/(3+2(n+1))}Te_2$, $(1+n)/(3+2n) < x < (1+(1+n))/(3+2(n+1))$.

(20) Evain, M.; Monconduit, L.; Van der Lee, A., manuscript in preparation.

Previous studies^{9,19} on MA_xTe_2 compounds suggested the lone M atom ribbons (MTe₂ blocks or “faults”) to play a crucial role in the slab stacking through the establishment of short intersandwich Te–Te contacts. The current, thorough analysis of the stacking rules in the MA_xTe_2 series shows that the anchorage of one sandwich to another might actually be governed by the interaction between the M atoms of one sandwich and the Te atoms of the other sandwich, the faults being not a requisite to such an interaction as exemplified by the $MA_{1/2}Te_2$ structure which presents type II short Te–Te contacts although having no faults.²⁰

The question of the true nature of the intrasandwich type I and intersandwich type II Te–Te short contacts remains. Indeed, if their presence is well understood in the $MA_{1/3}Te_2$ phases and interpreted^{6,8} as slightly bonding interactions linked to a charge transfer from the cations to the anions according to the $M^{3+}A^{2+}_{1/3}Te^{1/6-}_2$ oxidation formulation, their role must be clarified in the $MA_{1/2}Te_2$ compounds since those phases are well characterized by the integral oxidation state formulation $M^{3+}A^{2+}_{1/2}Te^{2-}_2$. A new electronic structure study is under way.

Acknowledgment. The research of AvdL has been made possible by a grant from the C.N.R.S (Sciences Chimiques) and that of VP by the Grant 202/93/1154 from the Grant Agency of the Czech Republic.

Supplementary Material Available: Listing of thermal parameters (1 page); $hklm$ observed and calculated structure factors (11 pages). Ordering information is given on any current masthead page.

Resolution of the 66-Fold Superstructure of DySe_{1.84} by X-ray Diffraction and Second-Moment Scaled Hückel Calculations

A. van der Lee,[†] L. M. Hoistad, and M. Evain*

Institut des Matériaux de Nantes, UMR-CNRS 110, Laboratoire de Chimie des Solides, 2, rue de la Houssinière, B.P. 3229, 44322 Nantes Cedex 3, France

B. J. Foran and S. Lee*

Willard H. Dow Laboratories, Department of Chemistry, Ann Arbor, Michigan 48109-1055

Received May 29, 1996. Revised Manuscript Received September 17, 1996⁸

We report the superlattice of the modulated structure DySe_{1.84}. The modulation is of the charge density wave type, associated with electronic states on selenium atoms arranged in two-dimensional square nets. The complete modulated structure can be described in the superspace group formalism in a 3+2 dimensional space group $C_{cimm}^{Pm\bar{2},n}$. The basic cell observed by single-crystal X-ray diffraction is orthorhombic with $a = 3.9912(3)$ Å, $b = 3.9863(1)$ Å, and $c = 8.206(1)$ Å. The modulation wave vectors are $\mathbf{q}_1 = \alpha\mathbf{a}^* + \beta\mathbf{b}^* + \frac{1}{2}\mathbf{c}^*$ and $\mathbf{q}_2 = \alpha\mathbf{a}^* - \beta\mathbf{b}^* + \frac{1}{2}\mathbf{c}^*$, where $\alpha = 0.33338(16)$ and $\beta = 0.27284(6)$. Structure refinement based on first- and second-order satellites as well as main lattice reflections produced solutions in four different space groups that could not be differentiated on the basis of agreement factors. A best solution was sought by use of second-moment scaled, tight-binding band calculations. The lowest energy model found was similar to but not identical with two of those refined for X-ray data. This lowest energy structure can be rationalized by analysis of second-nearest-neighbor interactions within the selenium square nets.

Introduction

Crystalline structures with highly anisotropic bonding, i.e., low-dimensional materials, have been extensively studied in the past few decades.^{1–4} The interest has grown as materials in this class have been found to exhibit high- T_c superconductivity, charge density waves, and intercalation chemistry. For the rare-earth chalcogenides, charge density wave (CDW) modulations as well as site occupancy ordering lead to a range of modulated structures.^{5,6} In particular, these modulations can be attributed to the electronic structure of two-dimensional square-nets of selenium atoms. As these phases are insulators, the concept of the covalent bond can be used to account for localized valence electrons. However, the proximity of these structures to the metallic regime encourages a band theoretical treatment in discussions of the electronic structure.

CDWs have been studied extensively in the transition-metal chalcogenides where the CDW is associated with electronic states comprised mainly of transition-metal d orbitals; e.g., TaS₂^{7,8} and Mo₂S₃.⁹ The low-dimensional rare-earth chalcogenides are thus very

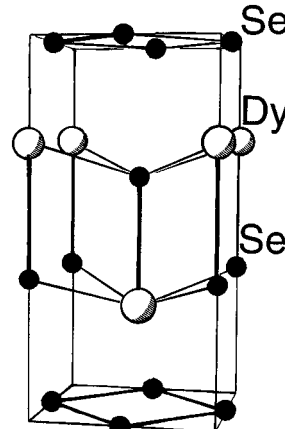


Figure 1. Unit cell of the average structure of Dy₁₁Se₂₀.

different in that there the CDW is associated with electronic states of the more anionic chalcogen atoms in the lattice. Thus while the metal atoms are subject to displacive modulations in the transition-metal CDW materials, in the rare-earth selenides, the CDW is observed as the displacement of the square sheet selenium atoms.

The average structure of the rare-earth dichalcogenides (Figure 1) was deduced from early studies, which also reported several differently sized superlattices.¹⁰ Recent X-ray determinations have allowed the resolution of the superlattice structure for a few of these

* To whom correspondence should be addressed.

[†] Current address: Laboratoire des Procédés et Matériaux Membranaires, UMR-CNRS 5635, Université de Montpellier II, Place E. Bataillon, 34095 Montpellier Cedex, France.

⁸ Abstract published in *Advance ACS Abstracts*, November 1, 1996.

(1) Wilson, J. A.; DiSalvo, F. J.; Mahajan, S. *Adv. Phys.* **1975**, 24, 117.

(2) Rouxel, J. Ed. *Crystal Chemistry and Properties of Quasi-One-Dimensional Structures*; Reidel: Dordrecht, 1986.

(3) Levy, F., Ed. *Electronic Structure and Electronic Transitions in Layered Materials*; Reidel: Dordrecht, 1986.

(4) Friend, R. H.; Yoffe, A. D. *Adv. Phys.* **1987**, 36, 1.

(5) Plambeck-Fischer, P.; Urland, W.; Abriel, W. Z. *Kristallogr.*

1987, 178, 182.

(6) Foran, B.; Lee, S.; Aronson, M. C. *Chem. Mater.* **1993**, 5, 974.

(7) Brouwer, R. *Ph.D. Thesis*, University of Groningen, The Netherlands, 1978.

(8) Yamamoto, A. *Phys. Rev. B* **1983**, 27, 7823.

(9) Schutte, W. J.; Disselborg, F. J.; De Boer, J. L. *Acta Crystallogr. B* **1993**, 49, 787.

(10) Wang, R.; Steinfink, H. *Inorg. Chem.* **1967**, 6, 1687.

Table 1. Crystal Data of Dy₁₁Se₂₀ and Conditions of the Data Collection

formula	Dy ₁₁ Se ₂₀
formula wt (amu)	306.05
density (calc)	7.830
<i>F</i> (000)	256
linear absorption coefficient (cm ⁻¹)	538.7
max correction	38.89
min correction	1.72
cryst size	<0.03 × 0.035 × 0.0025 cm ³
superspace group	<i>C</i> _{cmnl} ^{Pm21n}
basic unit cell	<i>a</i> = 3.9912(3) Å <i>b</i> = 3.9863(1) Å <i>c</i> = 8.206(1) Å vol = 130.56(3) Å ³
modulation vectors	$\mathbf{q}_1 = \alpha\mathbf{a}^* + \beta\mathbf{b}^* + \frac{1}{2}\mathbf{c}^*$ $\mathbf{q}_2 = \alpha\mathbf{a}^* - \beta\mathbf{b}^* + \frac{1}{2}\mathbf{c}^*$ $\alpha = 0.33338(16); \beta = 0.27284(6)$
diffractometer	CAD-4F
temp (K)	295 K
radiation	Mo K-L _{2,3}
scan mode	$\omega/(2\theta)$
<i>hklmn</i> range	<i>h</i> _{min} / <i>h</i> _{max}
main reflns	0/7
1st-order reflns	0/6
2nd-order reflns	0/6
std reflns	(020), (200), (011) every hour
	<i>k</i> _{min} / <i>k</i> _{max} <i>I</i> _{min} / <i>I</i> _{max} $\theta_{\text{min}}/\theta_{\text{max}}$
	-7/7 -14/14 1.5/40.0
	0/6 -13/13 1.5/35.0
	0/6 -12/12 1.5/30.0

phases with smaller, commensurate superlattice modulations, on the order of 2–10 times the subcell volume.^{5,6} However, the present work offers a study of a much larger superlattice ordering 66× the subcell volume. Some of the present authors previously reported X-ray evidence for an incommensurate superlattice in DySe_{1.84}, the same phase discussed in this article, though here it is referred to as Dy₁₁Se₂₀ (or even Dy_{65.3}Se₁₂₀). This superlattice was rationalized as due to a CDW state, based on analyses of the electronic structure as studied by extended Hückel band calculations. In particular, a calculated map of the Fermi surface showed nesting vectors matching the incommensurate wave vectors observed on precession X-ray diffraction photographs.⁶

To gain more insight into the structural distortions inherent in this phase, we now make a study of the complete modulated structure of Dy₁₁Se₂₀ by combining X-ray crystallography and semiempirical quantum mechanical theoretical methods. The symmetry of this two-dimensionally modulated structure can be conveniently described with a (3+2)*D* superspace group.^{11–13} To discriminate between the different alternative models that emerged from the structural refinements, we calculate the total energy using second-moment scaled Hückel theory.^{14–16} The second-moment scaling method has proven its viability for the rationalization of covalent systems, such as the Hume-Rothery electron concentration rules for transition-metal and noble-metal alloys and the late-transition-metal elemental structures.^{17–19}

Experimental Section

The synthesis and crystal growth of Dy₁₁Se₂₀ have been described elsewhere.⁶ Weissenberg and Buerger photographs confirmed the close to tetragonal symmetry of the basic cell,

Table 2. Reflection Statistics for Data Averaging in Super Space Group *C*_{cmnl}^{Pmmna}

	<i>N</i> ₁	<i>I</i>	<i>I</i> / <i>σ</i> (<i>I</i>)	<i>R</i> _{int}	<i>N</i> ₂
main	1411	606	27.0	0.019	434
1st order	1183	58	9.0	0.037	536
2nd order	334	16	4.9	0.053	226
all	2928	317	7.3	0.024	1196

^a *N*₁ and *N*₂ refer to reflections with *I* ≥ 2.5*σ*(*I*). *N*₁ is the number of data collected. The total numbers of data collected were 1799 (main), 2864 (1st order), 3125 (2nd order), and 7788 (all). *N*₂ is the number of independent reflections left after averaging. Averaging in other superspace groups (i.e., without using an inversion center), affected *R*_{int} only slightly, but the number of independent data increases drastically.

and clearly indicated the orthorhombic symmetry of the two modulation wave vectors $\mathbf{q}_1 = \alpha\mathbf{a}^* + \beta\mathbf{b}^* + \frac{1}{2}\mathbf{c}^*$ and $\mathbf{q}_2 = \alpha\mathbf{a}^* - \beta\mathbf{b}^* + \frac{1}{2}\mathbf{c}^*$. The same good-quality crystal used in the previous study was mounted on a CAD-4F diffractometer and the intensities of 80 first-order satellite reflections were carefully centered. A least-squares refinement of the 2θ values using the U-Fit program²⁰ yielded the values of the two a priori incommensurate parameters $\alpha = 0.33338(16)$ and $\beta = 0.27284(6)$. Subsequently three sets of data were collected: first for the main reflections, then the first-order satellite reflections, and finally second-order satellite reflections even though the latter had not been observed on the Buerger films. Table 1 lists the conditions of the data collection. The data were corrected for the scale variation, Lorentz-polarization effects, and absorption with the aid of several programs of the X-tal refinement package.²¹ The averaging of symmetry related reflections was done according to the point symmetry of the different possible space groups. The internal agreement factors for the averaging of the reflections (*I* ≥ 2.5*σ*(*I*)) were always between the values of 0.017 and 0.030. Some statistics regarding the different reflection classes are compiled in Table 2. The nonlinear least-squares refinements were performed using the JANA program²² in the full-matrix mode, with unit weights for all reflections. The scattering factors for neutral atoms and the anomalous dispersion correction were taken from International Tables for X-ray Crystallography.

(11) Janssen, T.; Janner, A. *Adv. Phys.* **1987**, *36*, 519.
(12) Janssen, T.; Janner, A.; Looyenga-Vos, A.; de Wolff, P. M. In *International Tables for Crystallography*; Kluwer Academic Publishers: Dordrecht, 1992; Vol. C, p 797.

(13) van Smaalen, S. *Cryst. Rev.* **1995**, *4*, 79.
(14) Pettifor, D. G.; Podloucky, R. *Phys. Rev. Lett.* **1984**, *53*, 1080.
(15) Burdett, J. K.; Lee, S. *J. Am. Chem. Soc.* **1985**, *107*, 3063.
(16) Lee, S.; Foran, B. *J. Am. Chem. Soc.* **1994**, *116*, 154.
(17) Hoistad, L. M.; Lee, S. *J. Am. Chem. Soc.* **1991**, *113*, 8216.
(18) Lee, S. *J. Am. Chem. Soc.* **1991**, *113*, 8216.
(19) Lee, S.; Rousseau, R.; Wells, C. *Phys. Rev. B* **1992**, *46*, 121.

(20) Evain, M. *U-FIT*: a cell parameter refinement program, Institut des Matériaux, Nantes, France, 1992.

(21) Hall, S. R.; Flack, H. D.; Stewart, J. M. *X-tal 3.2: Reference Manual*; Universities of Western Australia, Geneva, and Maryland, 1992.

(22) Petříček, V. *JANA93*: programs for modulated and composite crystals, Institute of Physics, Praha, Czech Republic, 1993.

Symmetry and Refinement

Average and Basic Structure. The average structure has already been determined by Foran and Lee using main reflections only.⁶ It is described in the tetragonal space group *P4/nmm* with three independent atoms, viz., Dy(1), Se(1), and Se(2) on the Wyckoff sites *2c* ($1/4, 1/4, 0.73$), *2c* ($1/4, 1/4, 0.37$), and *2a* ($1/4, 1/4, 0$), respectively. Dy(1) and Se(1) form a distorted NaCl-type framework between infinite two-dimensional square sheets formed by the Se(2) anions (Figure 1). The infinite Se(2) sheets are slightly depopulated. By using a sophisticated split model for Se(2) and anisotropic Debye–Waller parameters formally not allowed by the site symmetry, the authors obtained a final *R* factor of 0.020 (*wR* = 0.018). Although somewhat artificial, the model gives a clear indication of the displacive character of the modulation. The real modulation, however, can be determined only with the intensities of the satellite reflections. In addition, an eventual occupancy modulation in the Se(2) square sheets will only show up in the determination of the modulated structure.

Since the modulation wave vectors have orthorhombic symmetry, the basic structure is also necessarily orthorhombic, unlike the previously reported average structure. Note the difference between average and basic structure. The former is obtained by taking the average of all displacive and occupational deviations over one complete period of the modulation wave; experimentally it is determined by using only the main reflections in the refinement process. The basic structure, on the contrary, is obtained by setting all modulation amplitudes to zero. Thus, the modulated structure is equal to the sum of the basic structure plus the modulation.

The new measurements show that even the average structure is slightly orthorhombic, expressed in a small but significant length difference of the *a* and *b* axes, the angle γ remaining 90° (Table 1). These observations, along with the modulation wave vector components ($\pm\alpha, \pm\beta, 1/2$), lead to *Pmmn* or one of its subgroups as likely space group choices to describe the symmetry of both the average and basic structure. A refinement of the average structure parameters previously obtained by Foran and Lee in *Pmmn* yielded similar agreement factors (using the same $(\sin \theta/\lambda)_{max}$)⁶ but did not give significant deviations that were indicative of a clear orthorhombic distortion. We therefore conclude that the average structure is tetragonal within a very good approximation. The refinement results with isotropic Debye–Waller parameters were used as a starting point for the determination of the modulated structure in order to avoid bias in the refinement of the displacive modulation amplitudes. The *R* factor of this model was 0.106 (*wR* = 0.114).

Modulated Structure. Not only the basic cell parameters but also the modulation parameters ($\pm\alpha, \pm\beta, 1/2$) are slightly different from those previously reported. It should be noted that α , within 1 standard deviation, is equal to the rational value $1/3$ and that β , within 2 standard deviations, is equal to $3/11$. Thus, the modulated structure could be described in a unit cell with a tripled *a*-axis, an 11-fold *b*-axis, and a doubled *c*-axis using standard crystallographic techniques. However, it is advantageous to use the superspace formalism for the refinement and analysis of such a large superstructure. The superspace formalism for modulated struc-

tures naturally divides the analysis into an average and a modulated part.^{10,12} This division gives a smoother refinement process, often needing less independent parameters, and finally it also gives a direct link to the order parameters occurring in Landau theory.²³ In the present case the number of independent parameters can be reduced from 264 positional and 66 occupational parameters in a conventional supercell refinement to 33 positional and 5 occupational parameters (highest symmetry considered) using the superspace formalism.

Since there are two independent wave vectors \mathbf{q}_1 and \mathbf{q}_2 , each spot of the diffraction pattern can be indexed with five integers (h, k, l, m_1, m_2) . The symmetry of the structure is described with a (3+2)*D* superspace group. To analyze the systematic extinctions of the diffraction pattern, it is necessary to transform the basic unit cell in such a way that the symmetry-determined, rational components of the wavevector vanish. The required transformation is $\mathbf{a}' = \mathbf{a}$, $\mathbf{b}' = \mathbf{b}$, $\mathbf{c}' = 2\mathbf{c}$ which results in the new wavevector components $(\pm\alpha, \pm\beta, 0)$. The five reflection indexes transform accordingly to $H = h$, $K = k$, $L = 2l + m_1 + m_2$, $M_1 = m_1$, $M_2 = m_2$. The diffraction pattern now exhibits the general reflection condition $L + M_1 + M_2 = 2n$, corresponding to a centering translation vector of $(\mathbf{c} + \mathbf{a}_4 + \mathbf{a}_5)/2$, where \mathbf{a}_4 and \mathbf{a}_5 are the fourth and fifth unit vector respectively of the (3+2)*D* direct lattice. The reflection conditions corresponding to nonsymmorphic symmetry elements are $H + K = 2n$ and $H + K + M_1 + M_2 = 2n$ for $(HK0M_1M_2)$ reflections. However, the latter condition, is already implied by the first and the centering condition. These conditions enable us to write the symbol of the (3+2)*D* superspace group as $C_{c\bar{m}\bar{m}1}^{Pmmn}$. Here the symbol *Pmmn* in the upper line represents the 3*D* space group of the (external) basic structure, and the symbol *c̄m̄m̄1* in the bottom line the 2*D* space group that corresponds to the (internal) modulated part of the structure. The arrangement of the elements in the upper and lower lines is such that paired elements are on top of each other. The prefix *C* indicates the centering in internal space.

The matrix representation $\Gamma(R)$ of each (3+2)*D* symmetry operation *R* of the superspace group is determined by using $\Gamma_I(R)\sigma = \sigma\Gamma_E(R)$, where $\Gamma_E(R)$ is the (3 × 3) matrix representation corresponding to the rotational part of the (external) 3*D* symmetry operation of the basic structure, $\Gamma_I(R)$ is a (2 × 2) matrix acting on the fourth and fifth coordinate, and σ is a (2 × 3) matrix whose rows are formed by the components of the two modulation wave vector. The (5 × 5) matrix $\Gamma(R)$ is then constructed from $\Gamma_E(R)$ and $\Gamma_I(R)$ by

$$\Gamma(R) = \begin{pmatrix} \Gamma_E(R) & 0 \\ 0 & \Gamma_I(R) \end{pmatrix} \quad (1)$$

Table 3 lists all symmetry elements of $C_{c\bar{m}\bar{m}1}^{Pmmn}$, together with their associated external and internal translation vectors \mathbf{v}_E and \mathbf{v}_I . It should be noted that because of the centering condition there are two symmetry elements of each kind in the unit cell that are

(23) Pérez-Mato, J. M.; Madaragia, G.; Tello, M. *J. Phys. Rev. B* **1983**, *30*, 1534.

Table 3. Symmetry Elements of the Superspace Group $C_{\text{cmml}}^{\text{Pmmn}}$

$(E_L, 1 n_1, n_2, n_3, n_4, n_5)$	$(E_C, 1 0, 0, 1/2, 1/2, 1/2)$
$(2^x, \mathbf{m} 1/2, 0, 0, 0, 0)$	$(i, 2 0, 0, 0, 0, 0)$
$(m_x, \mathbf{m} 1/2, 0, 0, 0, 0)$	$(2^y, \mathbf{m} 0, 1/2, 0, 0, 0)$
$(2^z, \mathbf{m} 1/2, 0, 0, 0, 0)$	$(m_y, \mathbf{m} 0, 1/2, 0, 0, 0)$
$(m_z, \mathbf{m} 1/2, 0, 0, 0, 0)$	$(2^z, 2 1/2, 1/2, 0, 0, 0)$
$E_L = \begin{pmatrix} 1 & 0 & 0 \\ 0 & 1 & 0 \\ 0 & 0 & 1 \end{pmatrix}$	$E_C = \begin{pmatrix} 1 & 0 & 0 \\ 0 & 1 & 0 \\ 0 & 0 & 1 \end{pmatrix}$
$2^x = \begin{pmatrix} 1 & 0 & 0 \\ 0 & \bar{1} & 0 \\ 0 & 0 & \bar{1} \end{pmatrix}$	$2^y = \begin{pmatrix} \bar{1} & 0 & 0 \\ 0 & 1 & 0 \\ 0 & 0 & \bar{1} \end{pmatrix}$
$2^z = \begin{pmatrix} \bar{1} & 0 & 0 \\ 0 & \bar{1} & 0 \\ 0 & 0 & \bar{1} \end{pmatrix}$	$2^z = \begin{pmatrix} \bar{1} & 0 & 0 \\ 0 & \bar{1} & 0 \\ 0 & 0 & 1 \end{pmatrix}$
$m_x = \begin{pmatrix} \bar{1} & 0 & 0 \\ 0 & 1 & 0 \\ 0 & 0 & 1 \end{pmatrix}$	$m_y = \begin{pmatrix} 1 & 0 & 0 \\ 0 & \bar{1} & 0 \\ 0 & 0 & 1 \end{pmatrix}$
$m_z = \begin{pmatrix} 1 & 0 & 0 \\ 0 & 1 & 0 \\ 0 & 0 & \bar{1} \end{pmatrix}$	$m_z = \begin{pmatrix} 1 & 0 & 0 \\ 0 & 1 & 0 \\ 0 & 0 & \bar{1} \end{pmatrix}$
$1 = \begin{pmatrix} 1 & 0 \\ 0 & 1 \end{pmatrix}$	$2 = \begin{pmatrix} \bar{1} & 0 \\ 0 & \bar{1} \end{pmatrix}$
$2 = \begin{pmatrix} \bar{1} & 0 \\ 0 & \bar{1} \end{pmatrix}$	$m = \begin{pmatrix} 0 & 1 \\ 1 & 0 \end{pmatrix}$
$m = \begin{pmatrix} 0 & 1 \\ 1 & 0 \end{pmatrix}$	$\bar{m} = \begin{pmatrix} 0 & \bar{1} \\ \bar{1} & 0 \end{pmatrix}$

^aThe (3+2)D symmetry element is designated $(R_E, R_I|v_1, v_2, v_3, v_4, v_5)$, where R_E and R_I are represented by their respective symmetry symbols, (v_1, v_2, v_3) is the external translation vector \mathbf{v}_E , and (v_4, v_5) is the internal translation vector \mathbf{v}_I . All symmetry elements can be combined with the lattice translations E_L or the centering translation E_C . The element n_i , $i = 1-5$, assumes all integer values.

similar in the average structure but different in the modulated structure. Therefore care must be taken in placing the unit cell contents with respect to these two symmetry elements.

Displacive modulation functions for all atoms and an occupational one for Se(2) were considered. The modulation functions are expanded in a Fourier series:

$$\mathbf{r}^\nu(\bar{x}_4, \bar{x}_5) = \mathbf{r}_0^\nu + \sum_{\substack{n_1, n_2=0 \\ n_1=n_2 \neq 0}}^{\infty, \infty} \{ \mathbf{u}_{s, n_1, n_2}^\nu \sin[2\pi(n_1\bar{x}_4 + n_2\bar{x}_5)] + \mathbf{u}_{c, n_1, n_2}^\nu \cos[2\pi(n_1\bar{x}_4 + n_2\bar{x}_5)] \} \quad (2)$$

$$P^\nu(\bar{x}_4, \bar{x}_5) = P_0^\nu + \sum_{\substack{n_1, n_2=0 \\ n_1=n_2 \neq 0}}^{\infty, \infty} \{ P_{s, n_1, n_2}^\nu \sin[2\pi(n_1\bar{x}_4 + n_2\bar{x}_5)] + P_{c, n_1, n_2}^\nu \cos[2\pi(n_1\bar{x}_4 + n_2\bar{x}_5)] \} \quad (3)$$

where ν counts the independent atoms in the basic unit cell. The arguments of the modulation functions are defined as follows:

$$\bar{x}_4 = t_1 + \mathbf{q}_1 \cdot \mathbf{r}_{0,L}^\nu = t_1 + \mathbf{q}_1 \cdot (\mathbf{r}_0^\nu + \mathbf{L}) \quad (4)$$

$$\bar{x}_5 = t_2 + \mathbf{q}_2 \cdot \mathbf{r}_{0,L}^\nu = t_2 + \mathbf{q}_2 \cdot (\mathbf{r}_0^\nu + \mathbf{L}) \quad (5)$$

where t_1 and t_2 are the global phases of the modulation waves ($t_1 = t_2 = 0$ is used in the present work), \mathbf{L} is the basic structure lattice translations; $\mathbf{u}_{s, n_1, n_2}^\nu = (A_{x,s,n_1,n_2}^\nu, A_{y,s,n_1,n_2}^\nu, A_{z,s,n_1,n_2}^\nu)$ and $\mathbf{u}_{c, n_1, n_2}^\nu = (A_{x,c,n_1,n_2}^\nu, A_{y,c,n_1,n_2}^\nu, A_{z,c,n_1,n_2}^\nu)$. Only the waves $(n_1, n_2) = (1, 0), (0, 1), (2, 0), (0, 2), (1, 1)$, and $(1, -1)$ were taken into account, since only satellite reflections up to the second order have been observed.

All three independent atoms have the same site symmetry. The modulation functions have to be invariant under the generating symmetry elements, m_x and m_y . Table 4 lists the restrictions on the Fourier amplitudes that follow from this invariance condition. The subgroups of $C_{\text{cmml}}^{\text{Pmmn}}$ that were also considered in the refinements are $C_{\text{cmml}}^{\text{Pm}2_1n}$, $C_{\text{cmml}}^{\text{P}2_1mn}$, $C_{\text{cmml}}^{\text{Pmm}2}$, and $C_{\text{cmml}}^{\text{P}2_12_1^2}$. These subgroups have different symmetry restrictions since the atoms, in general, are on sites with lower symmetry.

The refinements proceeded as follows. The first-order Fourier amplitude of the occupancy wave of Se(2), $P_{c,1,0}^{\text{Se}(2)}$, was given a small but significant value, e.g., 0.10. All first-order Fourier amplitudes were then refined in 5–10 iteration cycles using only the intensities of first-order satellites. Other parameters were kept fixed. Next the obtained refinement minimum was tested against a reversal of the signs of arbitrarily chosen displacive Fourier amplitudes. The possibility of a lower R factor by using -0.10 as a starting value for $P_{c,1,0}^{\text{Se}(2)}$ was also verified. The most satisfactory solution was then used for further refinements. The basic structure parameters were refined using only the main reflections. This was followed by a combined refinement of all basic parameters and first-order Fourier amplitudes using main plus first-order satellite reflections. At the end of this stage the R factors were generally about 0.06 for the main reflections and 0.13 for the first-order satellites. Finally the second-order satellite reflections were added to the refinement process for the determination of all parameters, including the second-order Fourier amplitudes.

In the five tested models anisotropic Debye–Waller parameters for all atoms and an extinction parameter were refined. All the models gave comparable R factors, except the model in $C_{\text{cmml}}^{\text{P}2_1mn}$, where large correlations hampered a smooth convergence. To decide which models were preferable, interatomic distances in the **3a** \times **11b** \times **2c** supercell were calculated. The $C_{\text{cmml}}^{\text{P}2_1mn}$ model was then rejected because of unrealistically short Se(2)–Se(2) distances (<2.0 Å). Table 5 compiles the agreement factors of the remaining four models I–IV. Table 6 gives the refinement results of the best model, $C_{\text{cmml}}^{\text{P}2_1mn}$ (vide infra). Structure factor tables and refinement information of the other models may be obtained upon request from the authors.

Interpretation of the Occupancy Wave of Se(2). Figure 2 shows the occupancy modulation function of Se(2), found for space group $C_{\text{cmml}}^{\text{P}2_1mn}$, model II, plotted against the two phase parameters t_1 and t_2 . A steep minimum at $\sim(t_1, t_2) = (0.8, 0.1)$ is observed, whereas a similar steep maximum is absent. Minimal and maximal function values are slightly below 0.0 and above 1.0, respectively. These nonphysical occupancy values are obtained because the modulation functions were expanded only up to the second order. Other examples have shown that functions describing large occupational modulations are of the block wave type with amplitude 1.^{24,25} In other words, sites are empty or occupied. Limiting the Fourier expansion to a few harmonics

(24) van der Lee, A.; van Smaalen, S.; Wiegers, G. A.; de Boer, J. L. *Phys. Rev. B* **1991**, 43, 9420.

(25) van der Lee, A.; Monconduit, L.; Brec, R.; Rouxel, J.; Petříček, V. *Acta Crystallogr. B* **1994**, 50, 119.

Table 4. Symmetry Restrictions for Superspace Group

<i>m_x</i>	<i>m_y</i>	<i>z^z</i>	<i>mm2</i>
$P_{s,n1,0}^v = -P_{s,0,n1}^v$	$P_{s,n1,0}^v = P_{s,0,n1}^v$	$P_{s,n1,0}^v = -P_{s,0,n1}^v$	$P_{s,n1,0}^v = P_{s,0,n1}^v = 0$
$P_{c,n1,0}^v = P_{c,0,n1}^v$	$P_{c,n1,0}^v = P_{c,0,n1}^v$	$P_{c,n1,0}^v = P_{c,0,n1}^v$	$P_{c,n1,0}^v = P_{c,0,n1}^v$
$P_{s,nl,n1}^v = 0$	$P_{s,nl,n1}^v$	$P_{s,nl,n1}^v = 0$	$P_{s,nl,n1}^v = 0$
$P_{c,nl,n1}^v$	$P_{c,nl,n1}^v$	$P_{c,nl,n1}^v$	$P_{c,nl,n1}^v$
$P_{s,n1,-n1}^v$	$P_{s,n1,-n1}^v = 0$	$P_{s,n1,-n1}^v = 0$	$P_{s,n1,-n1}^v = 0$
$P_{c,nl,-n1}^v$	$P_{c,nl,-n1}^v$	$P_{c,nl,-n1}^v$	$P_{c,nl,-n1}^v$
$A_{x,s,n1,0}^v = A_{x,s,0,n1}^v$	$A_{x,s,n1,0}^v = A_{x,s,0,n1}^v$	$A_{x,s,n1,0}^v, A_{x,s,0,n1}^v$	$A_{x,s,n1,0}^v = A_{x,s,0,n1}^v$
$A_{x,c,n1,0}^v = -A_{x,c,0,n1}^v$	$A_{x,c,n1,0}^v = A_{x,c,0,n1}^v$	$A_{x,c,n1,0}^v = A_{x,c,0,n1}^v = 0$	$A_{x,c,n1,0}^v = A_{x,c,0,n1}^v = 0$
$A_{y,s,n1,0}^v = -A_{y,s,0,n1}^v$	$A_{y,s,n1,0}^v = -A_{y,s,0,n1}^v$	$A_{y,s,n1,0}^v, A_{y,s,0,n1}^v$	$A_{y,s,n1,0}^v = -A_{y,s,0,n1}^v$
$A_{y,c,n1,0}^v = A_{y,c,0,n1}^v$	$A_{y,c,n1,0}^v = -A_{y,c,0,n1}^v$	$A_{y,c,n1,0}^v = A_{y,c,0,n1}^v = 0$	$A_{y,c,n1,0}^v = A_{y,c,0,n1}^v = 0$
$A_{z,s,n1,0}^v = A_{z,s,0,n1}^v$	$A_{z,s,n1,0}^v = A_{z,s,0,n1}^v$	$A_{z,s,n1,0}^v = A_{z,s,0,n1}^v = 0$	$A_{z,s,n1,0}^v = A_{z,s,0,n1}^v = 0$
$A_{z,c,n1,0}^v = A_{z,c,0,n1}^v$	$A_{z,c,n1,0}^v = A_{z,c,0,n1}^v$	$A_{z,c,n1,0}^v, A_{z,c,0,n1}^v$	$A_{z,c,n1,0}^v = A_{z,c,0,n1}^v$
$A_{x,s,n1,1}^v$	$A_{x,s,n1,1}^v$	$A_{x,s,n1,1}^v$	$A_{x,s,n1,1}^v$
$A_{x,c,n1,1}^v = 0$	$A_{x,c,n1,1}^v$	$A_{x,c,n1,1}^v = 0$	$A_{x,c,n1,1}^v = 0$
$A_{y,s,n1,1}^v = 0$	$A_{y,s,n1,1}^v$	$A_{y,s,n1,1}^v$	$A_{y,s,n1,1}^v$
$A_{y,c,n1,1}^v$	$A_{y,c,n1,1}^v$	$A_{y,c,n1,1}^v = 0$	$A_{y,c,n1,1}^v = 0$
$A_{z,s,n1,1}^v = 0$	$A_{z,s,n1,1}^v$	$A_{z,s,n1,1}^v = 0$	$A_{z,s,n1,1}^v = 0$
$A_{z,c,n1,1}^v$	$A_{z,c,n1,1}^v$	$A_{z,c,n1,1}^v$	$A_{z,c,n1,1}^v$
$A_{x,s,n1,-n1}^v = 0$	$A_{x,s,n1,-n1}^v$	$A_{x,s,n1,-n1}^v$	$A_{x,s,n1,-n1}^v = 0$
$A_{x,c,n1,-n1}^v = 0$	$A_{x,c,n1,-n1}^v$	$A_{x,c,n1,-n1}^v = 0$	$A_{x,c,n1,-n1}^v = 0$
$A_{y,s,n1,-n1}^v$	$A_{y,s,n1,-n1}^v$	$A_{y,s,n1,-n1}^v$	$A_{y,s,n1,-n1}^v$
$A_{y,c,n1,-n1}^v$	$A_{y,c,n1,-n1}^v = 0$	$A_{y,c,n1,-n1}^v = 0$	$A_{y,c,n1,-n1}^v = 0$
$A_{z,s,n1,-n1}^v$	$A_{z,s,n1,-n1}^v$	$A_{z,s,n1,-n1}^v$	$A_{z,s,n1,-n1}^v$
$A_{z,c,n1,-n1}^v$	$A_{z,c,n1,-n1}^v$	$A_{z,c,n1,-n1}^v$	$A_{z,c,n1,-n1}^v$

Table 5. Final Agreement Factors for the Refinements of Models I–IV

	overall			main			first-order			second-order				
	<i>R</i>	<i>R_w</i>	<i>N_{ref}</i>	<i>R</i>	<i>R_w</i>	<i>N_{ref}</i>	<i>R</i>	<i>R_w</i>	<i>N_{ref}</i>	<i>R</i>	<i>R_w</i>	<i>N_{ref}</i>	<i>n_p</i>	<i>n_o</i>
I	0.068	0.063	1196	0.037	0.041	434	0.102	0.127	536	0.230	0.289	226	33	5
II	0.054	0.051	1606	0.037	0.039	758	0.088	0.109	601	0.190	0.245	247	60	8
III	0.059	0.055	2045	0.034	0.036	811	0.089	0.110	944	0.243	0.300	290	66	10
IV	0.059	0.057	1913	0.037	0.040	685	0.081	0.106	944	0.193	0.244	284	58	7

^a The definitions of the *R* factors are $R = \sum |F_{\text{obs}}| - |F_{\text{cal}}| / \sum |F_{\text{obs}}|$ and $wR = [\sum w(|F_{\text{obs}}| - |F_{\text{cal}}|)^2 / \sum w|F_{\text{obs}}|^2]^{1/2}$, with unit weights $w = 1$. *N_{ref}* is the number of reflections with $I \geq 2.5\sigma(I)$ for each reflection class that is used in the refinements. *n_p* is the number of positional parameters, and *n_o* is the number of occupational parameters. The models I–IV correspond to the superspace groups $C_{cm\bar{m}1}^{Pmn}, C_{cm\bar{m}1}^{Pm\bar{n}}, C_{cm\bar{m}2}^{Pm\bar{m}2}$, and $C_{cm\bar{m}2}^{P\bar{m}2\bar{m}2}$, respectively.

necessarily leads to the mathematical phenomena of “under-” and “overshoot”. We took $P(\text{Se}(2)) = 1/2$ as a cutoff criterion to decide whether a site is occupied or not; above this cutoff the site is regarded as occupied, below $1/2$ it is empty. In this way, mean occupancies close to the refined values were obtained.

In-Plane Se Distributions. Figure 3 illustrates the distorted square-nets of the four best solutions from the structure refinements in a $3\mathbf{a} \times 11\mathbf{b}$ planar cell. Shown are the Se(2) distributions projected onto the $z=0$ plane (there are only slight displacements out of this plane). The solid lines represent Se(2)–Se(2) distances between 2.1 and 2.5 Å and the dashed lines represent distances between 2.5 and 2.8 Å. The remainder of the structure, i.e., the distorted NaCl arrangement of Dy and Se(1) between the successive Se(2) sheets is discarded for the moment, since its modulation is much weaker than that of the Se(2) sheet.

The $C_{cm\bar{m}1}^{Pmn}$ (Figure 3a, hereafter model I) and the $C_{cm\bar{m}1}^{Pm\bar{n}}$ (Figure 3b, hereafter model II) solutions are quite similar: in both cases vacant Se(2) sites are grouped together in pairs. Vacancy pairs are not found in the other known rare-earth selenides. The essential difference between the two models are two 90° rotated

Se–Se pairs. Model III, superspace group $C_{cm\bar{m}1}^{P\bar{m}2_1\bar{m}1}$ (Figure 3c), is less attractive than the first two models, since it contains much shorter Se–Se distances of about 2.18 Å, to be compared with the 2.38 Å distances in models I and II. The latter correspond with $(\text{Se–Se})^{2-}$ pairs found in many other selenides. Another distinguishing feature is that the vacancy pairs of model I and II are absent. However, the single-vacancy sites of model III are similar to other patterns of rare-earth selenides. Model IV, superspace group $C_{cm\bar{m}1}^{P\bar{m}2_1\bar{m}2}$ (Figure 3d), is comparable with the models I and II regarding the shortest Se–Se distances and the occurrence of vacancy pairs. Using the criterium of the shortest Se–Se bond distances, model III is clearly an inferior model with bond distances less than 2.3 Å. Therefore, we have focused our following theoretical study on the three remaining models, I, II and IV.

Discussion Based on Crystallographic Data

The very strongly displacive modulation wave of the Se(2) atoms may be attributed to the contributions from these atoms to electronic states near the Fermi level which are most affected by the CDW. The in-plane ($a-b$) modulation is much stronger than the modulation

**Table 6. Final Refinement Results for Model II
(Superspace Group $C_{cmm1}^{Pm\bar{2}1n}$)^a**

atom ν	Dy	Se(1)	Se(2)
x	0.25(*)	0.25(*)	0.25(*)
y	0.25(*)	0.258(1)	0.760(3)
z	0.36355(4)	0.18402(7)	0.0007(6)
$A_{x,s,1,0}^v$	0.0028(6)	-0.0032(6)	-0.055(2)
$A_{y,s,1,0}^v$	0.0058(4)	-0.0044(9)	-0.043(2)
$A_{z,s,1,0}^v$	-0.0015(7)	-0.0002(5)	0.0015(5)
$A_{x,c,1,0}^v$	0.0057(7)	0.003(1)	0.013(6)
$A_{y,c,1,0}^v$	0.0003(10)	0.007(2)	0.002(6)
$A_{z,c,1,0}^v$	0.0065(2)	0.0039(1)	0.0022(6)
$A_{x,s,2,0}^v$	-0.0012(7)	-0.002(3)	-0.0004(30)
$A_{y,s,2,0}^v$	0.002(1)	0.008(2)	-0.010(3)
$A_{z,s,2,0}^v$	-0.0007(3)	0.0021(5)	0.0003(7)
$A_{x,c,2,0}^v$	0.0008(8)	0.012(2)	0.013(3)
$A_{y,c,2,0}^v$	0.004(1)	-0.0006(30)	-0.013(3)
$A_{z,c,2,0}^v$	0.0008(2)	0.0010(5)	0.0022(4)
$A_{x,s,1,1}^v$	0.0044(9)	-0.001(2)	-0.024(4)
$A_{z,s,1,1}^v$	-0.0004(5)	0.0008(6)	-0.0025(7)
$A_{y,c,1,1}^v$	0.003(2)	-0.002(3)	0.017(6)
$A_{z,c,1,1}^v$	-0.0022(2)	-0.0002(3)	0.0007(6)
$A_{x,s,-1,-1}^v$	0.0035(7)	-0.001(1)	-0.022(2)
$A_{y,c,-1,-1}^v$	-0.002(2)	-0.003(3)	0.013(4)
$A_{z,c,-1,-1}^v$	-0.0018(2)	-0.0001(3)	0.0024(5)
P_0^v	1.0000	1.00000	0.794(8)
$P_{s,1,0}^v$	0.0000	0.0000	-0.06(3)
$P_{c,1,0}^v$	0.0000	0.0000	-0.23(1)
$P_{s,2,0}^v$	0.0000	0.0000	-0.01(2)
$P_{c,2,0}^v$	0.0000	0.0000	-0.03(2)
$P_{s,1,1}^v$	0.0000	0.0000	-0.10(5)
$P_{c,1,1}^v$	0.0000	0.0000	-0.15(3)
$P_{c,1,-1}^v$	0.0000	0.0000	-0.10(2)

^a Standard deviation are within parentheses. The y -coordinate of Dy was kept fixed to define the origin along the b -axis.

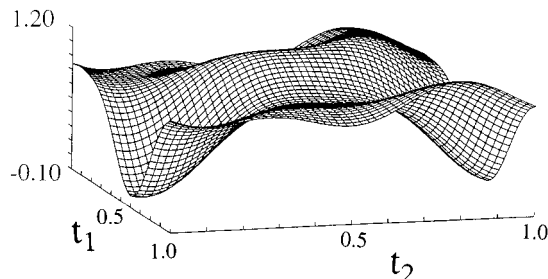


Figure 2. Occupational modulation wave of Se(2) for model II, superspace group $C_{cmm1}^{Pm\bar{2}1n}$ as a function of the two phase parameters t_1 and t_2 .

perpendicular to the $a-b$ plane. Although the average Se(2)-Se(2) distance is 2.833 Å, the real modulated structure shows Se(2)-Se(2) distances ranging from 2.37 to about 3.45 Å. The shortest distances, 2.375 and 2.382 Å, compare well with those found, e.g., in elemental Se (2.37 Å)²⁶ and A_2Se_3 ($A = K, Rb, Cs$; 2.36–2.38 Å).²⁷ Shortest distances in other rare-earth selenides are somewhat longer: 2.48 Å in La₁₀Se₁₉⁵ and 2.45 Å in LaSe₂.²⁸ Figure 4 shows a histogram of Se(2)-Se(2) distances in the square sheet. Distances primarily

cluster around 2.40 and 2.95 Å, although intermediate and longer distances are also present. The short distances represent Se_2^{2-} , whereas the longer distances are assigned to higher polyselenide ions Se_n^{m-} . We thus observe the effect of the CDW modulation as the formation of selenium–selenium bonds.

The in-plane modulation of Dy and Se(1) is in general a factor 5–10 times smaller than that of Se(2). The modulation in the c direction is greater for Dy than for both Se atoms, viz. about 0.053 Å. These displacements are nicely correlated to the Se(2)-Se(2) pair formation in the infinite square sheets. The Dy atoms projected onto the Se(2) sheets are approximately squarely coordinated by the Se(2) atoms, more precisely by the Se(2) sites whether occupied or not. If the projected Dy atom is close to a Se(2)-Se(2) pair, it tends to shift away from the infinite square sheet, thus toward the distorted NaCl layer. On the contrary, if the Se(2) atoms making up the square around Dy are not paired, the Dy atoms moves toward the Se(2) sheet, away from the NaCl layer. This type of correlation is reminiscent of that found in another two-dimensional occupationally modulated structure, $Ag_{0.6}NbS_2$,²⁴ in which S atoms (of NbSe₂ layers) move toward empty Ag sites in adjacent layers forming slightly puckered 2D honeycomb shaped lattices of Ag. The Se(1) displacive modulation is not directly linked to the occupational distribution of Se(2) since it is farther away from the infinite sheets.

The block wave character of the occupational modulation gives rise to either occupied or empty sites. The final model has 2 vacant sites out of every 11 sites in the square sheets, to be compared with, for instance, one vacancy out of every 10 sites in the case of $Ce_{10}Se_{19}$ and $Pr_{10}Se_{19}$.⁵ The observed Se deficiency may be the very reason for the orthorhombic symmetry of the modulated structure, since there is no tetragonal supercell compatible with a $Dy_{11}Se_{20}$ stoichiometry.

Much of the three model structures can be understood through the VSEPR (valence shell electron pair repulsion) rules.²⁹ In the VSEPR system of electron counting one may assign fixed numbers of valence electrons to particular coordination geometries. An isolated Se atom is assumed to have eight valence electrons. A selenium atom coordinated to only one other Se is assigned seven valence electrons, while a two-coordinate selenium atom has eight valence electrons if the coordination is linear and six valence electrons if bent. Thus an Se_2 dimer has two one-coordinate Se atoms and hence a total of 14 valence electrons. If we recall that a neutral Se atom has six valence electrons, we may denote such a Se_2 dimer as $[Se_2]^{2-}$ ($14 - 2 \times 6 = 2$).

We apply these VSEPR electron counting rules to the structure of $Dy_{11}Se_{20}$ in the following manner. First, let us assume that all Se-Se distances shown in Figure 3 correspond to Se-Se bonds; these correspond to all those made shorter by the charge density wave modulation. The defective square lattice is thus fragmented into molecular anionic selenium clusters. Following the VSEPR method of electron counting, to each of these clusters, we may assign a fixed number of electrons. In the case of model I for example the overall square lattice

(26) Donohue, J. *The Structure of the Elements*; Wiley: New York, 1974; p 317.

(27) Böttcher, P. *Z. Anorg. Allg. Chem.* **1977**, *432*, 167. Böttcher, P. *Ibid.* **1980**, *461*, 13.

(28) Bénazeth, S.; Carré, D.; Laruelle, P. *Acta Crystallogr. B* **1982**, *38*, 33.

(29) Cotton, F. A.; Wilkson, G. *Advanced Inorganic Chemistry*, 4th ed.; Wiley-Interscience: New York, 1980; p 196.

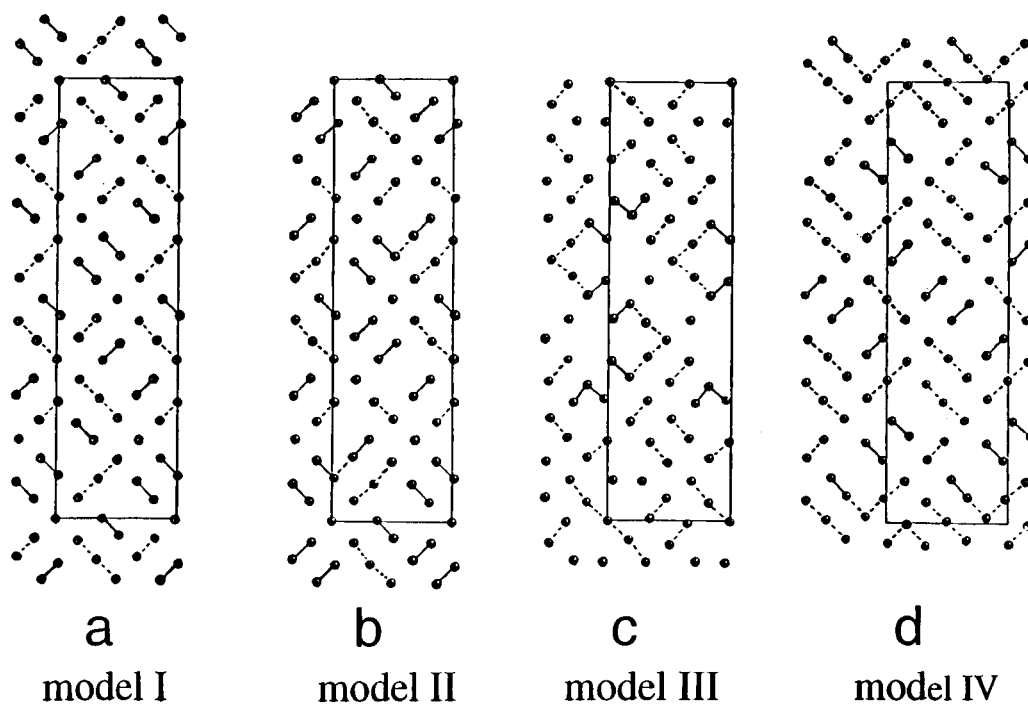


Figure 3. In-plane Se(2) distribution for the models of (a) $C_{cimnl}^{Pm2_1n}$, model I, (b) $C_{cimnl}^{Pm2_1n}$, model II, (c) $C_{cimnl}^{Pm2_1n}$, model III, and (d) $C_{cimnl}^{Pm2_1n}$, model IV. Solid lines represent Se(2)–Se(2) distances between 2.1 and 2.5 Å, dashed lines represent distances between 2.5 and 2.8 Å.

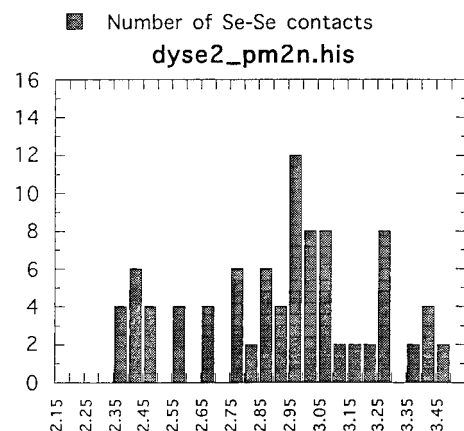


Figure 4. Number of Se(2)–Se(2) contacts in the $z = 0$ plane as a function of contact distance.

contains per unit cell 4 isolated Se^{2-} atoms, 16 Se_2^{2-} dimers, and 6 linear Se_3^{4-} trimers. Considering the full contents of the unit cell [for which the formula unit is $\text{Dy}_{132}\text{Se}_{240}$] the total charge of the Se atoms is -392 .³⁰ If each Dy atom assumes the oxidation state of +3, then we find a total positive charge of +396, which is within 1% of the calculated charge for the Se atoms given above.

This result is particularly important for the following reason. In the three models with chemically reasonable bond distances (models I, II, and IV) it turns out that in every case such electron counting results in an overall charge of -392 . This is true irrespective of whether we assume the minimum distance for a Se–Se bond is 2.8 Å or whether the minimum distance is 2.7 Å. We

(30) In arriving at this electron count, we have included the 132 Se atoms which do not form part of the defective square lattice shown in Figure 5. However, for these latter Se atoms, as they lie at a distance of 3.54 Å away from all other Se atoms, it is clear that by VSEPR that they should be considered Se^{2-} monomeric atoms.

therefore conclude that this agreement between the selenium lattice and the dysprosium oxidation state is not fortuitous. Indeed it should be noted that one possibility for the slight mismatch between the selenium and dysprosium charge is a slight nonstoichiometry in either selenium or dysprosium. Such a nonstoichiometry would be of a value too small to detect with X-ray crystallography. It would correspond to an approximate 1% change in Dy or Se composition. To emphasize this possibility we note that stoichiometries such as $\text{Dy}_{65.33}\text{Se}_{120}$ are plausible and provide perfect charge neutrality.

Calculational Method

For the energy we use the second moment scaled Hückel method where

$$E_{\text{TOT}} = \int_{E_F}^{-\infty} E \rho(E) dE + \gamma \int_{\infty}^{-\infty} E^2 \rho(E) dE$$

In this formula E_F is the Fermi level, $\rho(E)$ is the tight-binding density of states, and γ is a constant determinable from experimental equilibrium size. This is a minimal basis set calculation using Slater type orbitals with a single- ζ expansion, and the unweighted Wolfsberg–Helmholz approximation³² for off-diagonal matrix elements, i.e., $H_{ij} = K S_{ij}(H_{ii} + H_{jj})$. The parameters used to describe the energy and the shape of the basis orbitals for selenium are those optimized to account for the contracted s orbitals, as discussed in refs 16 and 31. Dysprosium atoms are assumed to donate three valence electrons to the selenium. The μ_2 -Hückel method has been previously applied to account for electron counting rules such as Wade's rules for electron-

(31) Hoffmann, R.; Shaik, S.; Scott, J. C.; Whangbo, M.-H.; Foshee, M. J. *J. Solid State Chem.* **1980**, 34, 263.

(32) Wolfsberg, M.; Helmholz, L. *J. Chem. Phys.* **1957**, 20, 83.

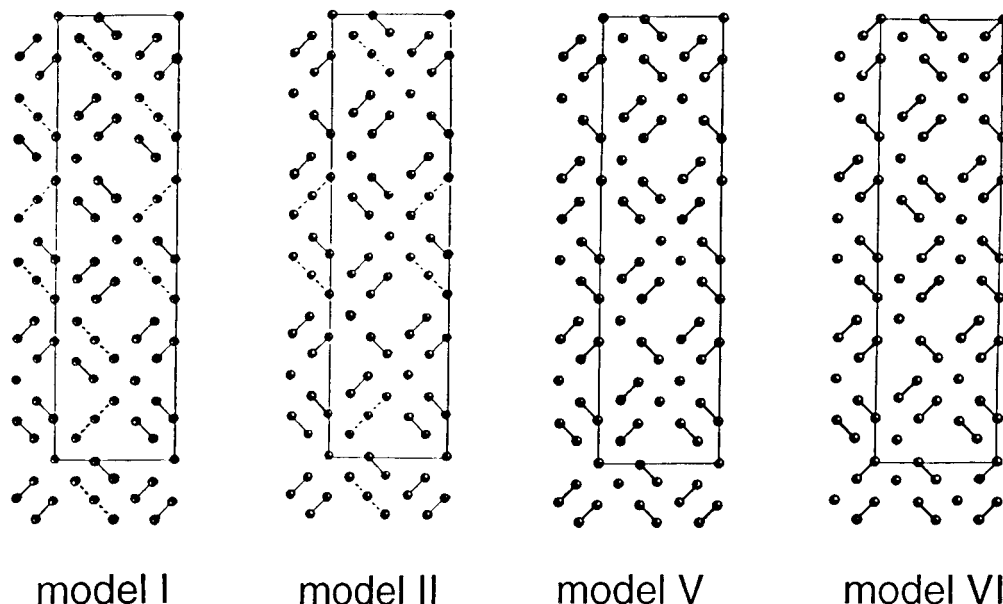


Figure 5. Idealized structures for calculation of second-moment scaled Hückel energies: (a) model I, (b) model II, (c) model V, and (d) model VI. Solid lines represent Se(2)–Se(2) distances between 2.1–2.5 Å, dashed lines represent distances between 2.5 and 2.8 Å.

deficient clusters, the Hume–Rothery rules for noble- and transition-metal alloys, and the octet rule of main-group compounds. We have further used this method to produce optimal energy structures for both solids and molecules that are in reasonable agreement with experiment. Systems studied include solids such as elemental boron, zinc, gallium, manganese, LaSe₂, La₁₀Se₁₉, and RbDy₃Se₈ and molecules such as boranes, carboranes, simple hydrocarbons, phosphorus–sulfur clusters, and transition-metal carbonyl clusters.^{16–19}

μ_2 -Hückel Results. We used the μ_2 -Hückel method to directly compare the energies of the three proposed models. In doing so some care must be taken. The precise location of the atoms are not known; therefore, any direct energetic comparison may result only in assessing the accuracy of bond lengths in a given model rather than an evaluation of the correctness of the overall distortion patterns. We therefore carried out a calculation on an idealized structure which minimizes errors due to incorrect bond lengths. Starting from the ideal square lattice, we allowed atoms either to shift a distance of 0.37 Å along the Se–Se bond directions or to stay in their ideal position. We then chose the patterns that most closely resembled the true structures of models I, II, and IV. The idealized structures of models I and II are shown in Figure 5. It may be seen that they are in reasonable agreement with the models from the X-ray determination. We found that the energies of models I, II, and IV are respectively –17 890.1, –17 891.5, and –17 888.0 eV. These results suggest that model II is the lowest energy structure.

This energy difference is in accord with our earlier work on smaller supercells in related rare-earth selenides. In these earlier studies we found that the energetically preferred structure was always one in which HOMO–LUMO (highest occupied and lowest unoccupied molecular orbitals) interactions between neighboring selenide fragments was maximized. This principle of maximal frontier overlap is a well-known general rule whenever interactions are strong and



Figure 6. Principle unfilled molecular orbitals, σ^* , found for the ions Se_3^{4-} and Se_2^{2-} .

covalent as is found in these systems.^{33,34} In the case of the rare-earth selenides, there are relatively few unfilled fragment orbitals. The principle of maximum overlap therefore reduces to one of minimization of all unoccupied-to-unoccupied orbital interactions. In models I, II and IV the principal unfilled molecular orbitals are the σ^* orbitals found in linear Se_3^{4-} and Se_2^{2-} clusters. These orbitals are illustrated in Figure 6. In model I for example it can be seen that there are pairs of linear Se_3^{4-} trimers that lie in a coaxial arrangement to one another (see Figures 3 and 5). As the LUMO orbitals on Se_3^{4-} are σ^* orbitals pointed along the axis of the Se_3^{4-} molecular axis, one finds that the coaxial Se_3^{4-} arrangement found in models I and IV lead to a LUMO–LUMO interaction rather than a pure LUMO–HOMO interaction. Such interactions are unfavorable. By contrast, in model II, all LUMOs are in direct overlap with neighboring HOMO orbitals. This fact is a significant factor in the stability of model II.

While the results of our theoretical calculations rule out models I and IV, these do not prove that model II is the correct crystallographic structure. One possible change in model II is to break the linear Se_3^{4-} trimers into a monomeric Se^{2-} and an Se_2^{2-} dimer. Similarly we can break the check-shaped Se_4^{4-} tetramers shown in Figure 3b into two Se_2^{2-} dimers. Such a change leaves all LUMOs pointed directly to HOMOs. Our calculations show that a model with such distortions allows a further stabilization of the energy of the system. Thus the lowest energy distortion patterns we

(33) Burdett, J. K. *Chemical Bonding in Solids*; Oxford Press: New York, 1955.

(34) Hoffmann, R. *Solids and Surfaces: A Chemist's View on Bonding in Extended Structures*; VCH Publishers, Inc.: New York, 1988.

have found are those of model V and VI shown in Figure 5. We find models V and VI have electronic energies respectively of $-17\ 892.86$ and $-17\ 892.92$ eV, 1.4 eV lower in μ_2 -Hückel energy than the model II structure. Model V is also a resultant structure if one replaces all the trimers of model I by monomer-plus-dimer combinations. Model V thus lies on a direct pathway between models I and II, while model VI involves a combination of elements from both models I and II. As models V and VI are rather close to the previous models, the crystallographic data are not by itself sufficient to resolve one way or another the validity of these models over the other models.

The principal difference between the lower energy theoretically generated models V and VI and the experimentally determined models I–IV are an absence of any linear Se_3^{4-} fragments in the former systems. As to our knowledge, there are no known linear Se_3^{4-} units in the selenide crystal chemistry literature, we believe that the energy difference may indeed be significant.

The present study has shown that a combination of advanced crystallographic analysis and second-moment scaled, tight-binding, band calculations is very useful in solving a complex modulated structure like $\text{DySe}_{1.84}$.

The X-ray analysis resulted in three different models with chemically reasonable bond distances and comparable agreement factors. These three models were, somewhat idealized, used as a starting point for the band calculations. The calculations suggested that the real structure should be somewhere between two of the proposed X-ray models. The lowest energy structure could be understood using simple HOMO–LUMO interaction arguments: the higher the interactions between neighboring selenide fragments throughout the structure, the lower the energy.

Acknowledgment. The research of A.v.d.L. has been made possible by a grant from the CNRS (Sciences Chimiques) and that of L.M.H. by a grant from the Conseil Général des Pays de la Loire. The work of B.J.F. and S.L. was supported by funds from the U.S. Petroleum Research Fund and NSF (DMR-9319196). In addition S.L. would like to thank the A.P. Sloan Foundation, the J.D. and C.T. MacArthur Foundation, and the Alexander von Humboldt Foundation for fellowships. We would also like to thank Prof. Jean Rouxel for his thoughtful comments.

CM960302T



ELSEVIER

Applied Surface Science 173 (2001) 115–121

applied
surface science

www.elsevier.nl/locate/apsusc

Mass density determination of thin organosilicon films by X-ray reflectometry

A. van der Lee^{a,*}, S. Roualdes^a, R. Berjoan^b, J. Durand^a

^a*Institut Européen des Membranes, UMR-CNRS 5635, Université de Montpellier II, cc 047, Place E. Bataillon, 34095 Montpellier Cedex 5, France*

^b*Institut de Science et de Génie des Matériaux et Procédés, CNRS, B.P. 5, Odeillo, 66125 Font-Romeu, France*

Received 15 April 2000; accepted 11 November 2000

Abstract

The mass density of thin organosilicon films deposited by chemical vapour deposition on silicon (0 0 1) surfaces has been determined by X-ray reflectometry. This method does not give a unique mass density value, but instead a bandwidth of possible values and compositions that are compatible with the experimental data if the layer thickness is not larger than about 350 nm. For thicker films thickness values obtained from ellipsometry data are used. The possible composition ranges are compared with data obtained by X-ray photo electron spectroscopy. © 2001 Elsevier Science B.V. All rights reserved.

PACS: 61.10.Kw; 68.55.Jk; 68.55.Nq

Keywords: Reflectometry; Mass density

1. Introduction

It has been recognized since long that plasma polymerization is a unique technique for preparing thin, uniform, and pinhole free polymeric films [1–4]. Unfunctionalized monomers that are not utilized in conventional polymer synthesis can be used in this polymerization process for the formation of highly cross-linked polymers. Organosilicon compounds are widely used as monomers in low-pressure plasma deposition due to their availability, liquid-state, volatility at room temperature, safe handling and low cost [5–8]. The structure of the thin films formed is very dependent on the more or less energetic character of

the plasma quantified using the composite parameter $\xi = V/FM$, where V is the input voltage, F the input gas flow rate, and M the molecular weight of the gas species in the plasma. Depending on whether ξ is high (hard plasma conditions) or low (soft plasma conditions), the structure of deposits can be, in fact, turned from SiO_2 -like inorganic dense coatings to silicone-like not very cross-linked polymers [9,10]. The mass density is a key structural factor to characterize the films as a function of plasma conditions. Previous studies [10,11] have shown that when ξ increases the plasma films density rises from a minimum value of 1.1–2.1 g cm^{−3} (SiO_2 density value) whatever the organosilicon monomer nature may be.

Thin film density can be determined by various techniques such as Rutherford backscattering, X-ray fluorescence, and forward-recoil spectrometry. The fastest and most precise method, however, is X-ray

* Corresponding author. Tel.: +33-467-14-9135;
fax: +33-467-14-9119.
E-mail address: avderlee@crit1.univ-montp2.fr (A. van der Lee).

reflectometry (XRR). Using this technique the mass densities of thin films can be determined at the condition that their composition is exactly known and that the film is homogeneous in depth, i.e. that there exists no mass density gradient across the thin film. Otherwise only the *electronic* density can be uniquely determined. The composition normally changes drastically as a function of plasma conditions; useful information on the silicon, carbon and oxygen content can be extracted from X-ray photo-electron spectroscopy (XPS) data. Using this complementary information the mass density can be in principle more accurately be determined. It is the purpose of this paper to show how precisely the mass density of thin films with partially unknown compositions can be determined by use of X-ray reflectometry. The bandwidth of the mass density and the composition are deduced for which the calculated reflectivity does not change and thus gives an equally good fit against the experimental data. It is shown in particular how the X-ray absorption by light elements such as silicon, carbon, and oxygen drastically influences the X-ray reflectivity, and how this can be used to get

information on density and composition. The results are complemented and compared with the results from ellipsometry and XPS.

2. Experiment and data reduction

Thin films were plasma polymerized by glow-discharge at 40 kHz in a home-made capacitively coupled parallel plate reactor previously reported [9,10]. In this study, the organosilicon monomer hexamethyldisiloxane (M2) supplied by Aldrich were used without any further purification. The varying operating parameters were the monomer partial pressure and the input power (controlled by peak to peak voltage value). Samples M2A to M2C (see Table 1) were prepared in a flow of 33×10^{-5} mol min $^{-1}$, M2D to M2F in 33×10^{-5} mol min $^{-1}$, and M2G to M2I in 1×10^{-5} mol min $^{-1}$. The input power was in each series 50, 75, and 100 V for M2A–M2C (M2D–M2F, M2G–M2I), respectively. The pressure in the reaction chamber was fixed at 40 Pa. The thin films were deposited on silicon (0 0 1) wafers. X-ray

Table 1
Numerical results of the XRR, XPS, and ellipsometry experiments^a

Sample	Thickness (nm)	ρ_e (eÅ $^{-3}$)	μ_l (nm $^{-1}$)	σ (nm)	c_O/c_{Si}	c_C/c_{Si} XPS	c_C/c_{Si} XRR	ρ_m (g cm $^{-3}$)
M2A	332	0.367	3.0	1.2/1.5	1.12	1.73	2.22–1.37 2.53–1.57	1.10–1.15 1.13–1.16
M2B	717	0.379	3.3	1.3/2.1	0.85	2.00	2.00–1.14 2.29–1.30	1.14–1.19 1.17–1.21
M2C	679	0.393	3.3	1.6/1.2	0.89	1.81	2.06–1.20 2.35–1.37	1.19–1.24 1.21–1.25
M2D	369	0.360	2.9	1.2/1.5	1.12	1.73	2.26–1.42 2.58–1.63	1.08–1.13 1.11–1.14
M2E	465	0.372	3.3	1.9/1.3	0.79	1.79	1.82–0.93 2.08–1.07	1.13–1.18 1.15–1.19
M2F	589	0.415	3.3	1.5/1.3	0.92	1.92	2.32–1.49 2.66–1.71	1.25–1.30 1.28–1.31
M2G	586	0.402	3.3	1.7/1.2	1.39	1.18	2.28–1.45 2.61–1.65	1.21–1.26 1.24–1.27
M2H	437	0.450	3.4	1.7/1.1	1.24	1.76	2.60–1.81 2.98–2.07	1.34–1.40 1.38–1.42
M2I	237	0.508	3.5	1.9/1.1	1.50	1.67	3.15–2.42 3.61–2.77	1.50–1.56 1.55–1.58

^aThe layer thickness values for samples M2H and M2I are from the XRR measurements themselves, the others from ellipsometry measurements. The column for the roughness σ contains two values for each entry two: the first one corresponds to the roughness of the air/film interface and the second one to that of the substrate/film interface. The columns for the XRR carbon concentration and the mass density contain also for each entry two lines: the upper one corresponds to the assumption $x_H = 3.0$ and the lower one to $x_H = 2.0$.

reflectivity measurements were performed with a Bruker-AXS D5000 diffractometer equipped with a special reflectivity stage and a graphite monochromator in the reflected beam. Cu-L_{3,2} X-rays ($\lambda = 0.154051$ and 0.15433 nm, respectively) were used for data collections on 11 thin organosilicon films prepared under different plasma conditions. Step times and widths were variable according to the intensity and the details found in the reflectivity curves. A number of rocking curves and detector scans were performed to evaluate the amount of diffuse scattering. Diffuse scattering as well as the detector dead current was subtracted from the raw data to get the true specular signal. Normalizing was in general done manually during the fit process in order to reproduce as well as possible the small intensity drop at the plateau of total external reflection just before the critical angle that is entirely due to absorption effects. All calculations were performed with the program IMD4.1 [17,18]. A Gaussian function simulating the instrumental resolution function was used to convolve the calculated reflectivity before being used in the fitting procedure against the experimental data. Ellipsometry measurements were performed using a Plasmos SD 2300 ellipsometer and a laser wavelength of 632.8 nm. XPS spectra were recorded with a Cameca Ribber SIA 200 electron spectrometer equipped with a double stage cylindrical mirror electron energy analyzer. The samples were analyzed without any initial ion bombardment.

3. Data analysis

Several reviews on X-ray and neutron reflectivity exist that cover the basics, data analysis, and/or applications [12–16]. Here only those aspects will be recalled that are relevant for the determination of mass densities. In addition it will be shown how the mass density is determined for samples with partially unknown composition.

The X-ray (or neutron) reflectance of a homogeneous thin layer on a homogeneous substrate is mathematically described by Airy's function:

$$R(k) = \frac{R_f + R_s e^{2ik_f d}}{1 + R_f R_s e^{2ik_f d}} e^{-2ikd}, \quad (1)$$

where R_f is the Fresnel reflectance of the thin film, and

R_s that of the substrate, respectively:

$$R_s = \frac{k_f - k_s}{k_f + k_s}, \quad (2)$$

$$R_f = \frac{k - k_f}{k + k_f}. \quad (3)$$

Here, d is the thickness of the thin film and k is the free space wave number: $k = k_0 \sin \theta = 2\pi \sin \theta / \lambda$ with θ the angle between the incident beam and the film surface, and λ the wavelength of the impinging radiation. Here, k_f and k_s are the wave numbers inside the film and the substrate, respectively: $k_f = n_f k$ and $k_s = n_s k$, where n_f and n_s are the refractive indices for X-rays for the film and the substrate, respectively. The measured reflectivity is given by the absolute square of Eq. (1). Eqs. (1) and (2) are usually modified to take into account the non-abrupt nature of the interfacial transitions. In this study a Debye–Waller type factor was used that corresponds to an error-type interfacial profile function [17,18].

The refractive index, n , is in general a complex quantity; its imaginary part includes the effects of absorption inside the material. It can be written, outside the absorption edges of the elements, as

$$\begin{aligned} n(z) &= 1.0 - \delta(z) + i\beta(z) \\ &= 1.0 - \frac{2\pi r_0}{k_0^2} N_A \rho_m(z) \frac{\sum c_j (Z_j + f'_j - if''_j)}{\sum c_j A_j} \\ &= 1 - \frac{2\pi r_0}{k_0^2} N_A \rho_m K, \end{aligned} \quad (4)$$

with r_0 the Thomson scattering length of the electron, N_A Avogadro's number, and ρ_m the mass density. The factor K incorporates the chemical information of the thin film: c_j is the number of species j in the chemical formula, and Z_j , A_j , f'_j , and f''_j the atomic number, atomic weight, real and imaginary dispersion correction factor, respectively. The sum runs over all elements in the chemical formula. The parameters $\delta(z)$ and $\beta(z)$ are the principal parameters to be determined by the X-ray reflectometry experiment. If it is assumed that the system consists of a substrate and a thin film with constant density, then $\delta(z)$ and $\beta(z)$ decouple to the constant factors δ_f , β_f , and δ_s , β_s for the film and the substrate, respectively. The factors δ_f and β_f can be directly related to the electron density ρ_e and the linear

absorption coefficient μ_l of the thin film, respectively.

$$\rho_e = \frac{\delta_f}{2\pi\lambda^2 r_0}, \quad (5)$$

$$\mu_l = \frac{4\pi\beta_f}{\lambda}. \quad (6)$$

Normally δ_f and β_f are determined by non-linear least-squares fitting of the absolute square of Eq. (1) against the experimental data. The factors δ_f and β_f can also be written in terms of the mass density and the chemical composition using Eq. (4):

$$\delta_f = \frac{2\pi r_0}{k_0^2} N_A \rho_m \frac{\sum c_j (Z_j + f'_j)}{\sum c_j A_j}, \quad (7)$$

$$\beta_f = \frac{2\pi r_0}{k_0^2} N_A \rho_m \frac{\sum c_j f''_j}{\sum c_j A_j}. \quad (8)$$

Dividing these two equations, one gets

$$\frac{\delta_f}{\beta_f} = \frac{\sum c_j (Z_j + f'_j)}{\sum c_j f''_j}. \quad (9)$$

Taking $c_{Si} = 1$, and supposing that the number of hydrogen atoms is x_H times the number of carbon atoms, one finally ends up with

$$c_C = \frac{\delta_f f''_O - \beta_f (Z_O + f'_O)}{\beta_f (Z_C + f'_C) + x_H \beta_f (Z_H + f'_H) - \delta_f f''_C} c_O \\ + \frac{\delta_f f''_{Si} - \beta_f (Z_{Si} + f'_{Si})}{\beta_f (Z_C + f'_C) + x_H \beta_f (Z_H + f'_H) - \delta_f f''_C}. \quad (10)$$

Thus, with the experimentally determined parameters δ_f and β_f , and for a given range of c_O values, the range of c_C values can be calculated that gives an identical fit to the experimental data. The Eq. (7) or (8) gives subsequently the corresponding range of mass density values.

It is noted that an approximate value of the film mass density can be calculated from the position of the critical angle by combining Snell's law and Eq. (4) with $K = 1/2$:

$$\rho_m \approx \frac{2\pi\theta_c^2}{\lambda^2 N_A r_0}. \quad (11)$$

This relation only holds for thin films containing merely light elements and few hydrogens.

4. Results and discussion

X-ray specular reflectivity data for some samples are given in Fig. 1 on a logarithmic scale for the complete curve and on a linear scale for the interval around the critical edges in Fig. 2. All samples, regardless of plasma conditions and/or film thickness, show surface roughness values of about 1.2–1.9 nm and substrate/film interface roughness values in approximately the same range. For some samples

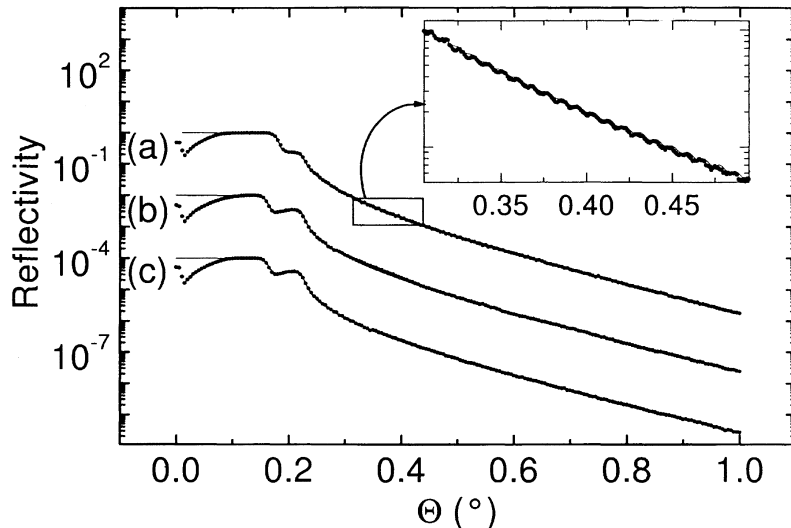


Fig. 1. X-ray reflectivity data (\bullet) and the best fit (solid line) for samples M2H (a), M2D (b), and M2A (c), respectively, on a logarithmic scale. The inset shows the narrowly-spaced interference fringes due to the 437 nm thick layer of sample M2H.

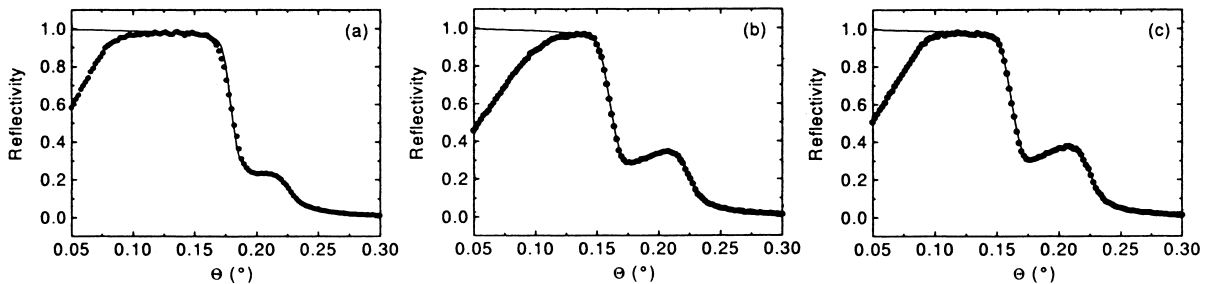


Fig. 2. X-ray reflectivity data (\bullet) and the best fit (solid line) of samples M2H (a), M2D (b), and M2A (c), respectively, on a linear scale around the critical angle.

the so-called Kiessig fringes are observed that are due to interference between waves scattered at the air/film interface and those at the film/substrate interface. The inset of Fig. 1 shows fringes that are due to a 437 nm thick film. These fringes can only be modeled by assuming a gaussian width of the resolution function of 0.004° instead of the usual 0.006° . This is quite exceptional in the present set-up owing to the very good quality of this particular sample (M2H). In order to explain why the fringes of the two other samples in Fig. 1 ((b) and (c)) are not resolved, although they are thinner — 369 (b) and 332 nm (c), respectively — than the sample of Fig. 1(a), the possible causes of the smoothening of the fringes should be discussed. The fringe contrast, which is normally a signature of the density difference between layer(s) and substrate is usually affected by instrumental and sample-dependent factors. Instrumental resolution factors are due to the collimation of the beam and the wavelength spread of the beam. They remain the same for all investigated samples. Sample-dependent factors that may smoothen out the fringe contrast include effects due to a finite curvature of the sample [19,20] and the lateral (in)homogeneity of the thin film [15,21]. They may vary from sample to sample. All effects together may be included in one Gaussian width parameter for a Gaussian resolution function, describing the smoothening of the Kiessig fringes due to sample and instrumental effects. The specifications of the reflectivity stage of the D5000 diffractometer are that thicknesses up to 350 nm can be measured. Apparently this upper limit can be pushed up a bit in the case of samples of very good quality.

The reflectivity in the vicinity of the critical angles is crucial for the determination of the mass density

(Fig. 2). It shows initially an increase before reaching a more or less constant value at the plateau of total external reflection. This increase is due to an increase of the effective width of the beam that is partly hidden behind the sample surface for grazing angles near to 0.0° . It is emphasized that there are two different critical angles, the first one corresponding to the electronic density within the film and the second one to that within the substrate. This particular system — having a film electronic density lower than the substrate density — can in fact be considered as a quasi-waveguide [22]. Waveguide modes are, however, not observed. The intensity on the plateau between the critical angles is mainly caused by the absorption within the thin film. It is noted that, although the scattering elements in the film (Si, O, C, and H) have very low photoabsorption cross sections, the absorption is very large, owing to the grazing incidence geometry of the experiment, making the pathlength through the film very large. Taking for example sample M2A (Fig. 2) we find at a grazing incidence angle of 0.2° and for a film thickness of 332 nm (Table 1) a single-scattering pathlength through the thin film of approximately 190 μm . This gives an intensity reduction to about $\exp(-\mu_l)l = 0.53$ times the value at the plateau of total external reflection. In reality the reduction is somewhat larger because of multiple scattering that is quite important around the critical angle.

Although the electronic density and the absorption coefficient are mainly determined from the reflectivity values in the vicinity of the critical angles (Fig. 2), the complete reflectivity curve (Fig. 1) should be considered in order to justify the assumption of a single homogeneous layer on top of a substrate. If this

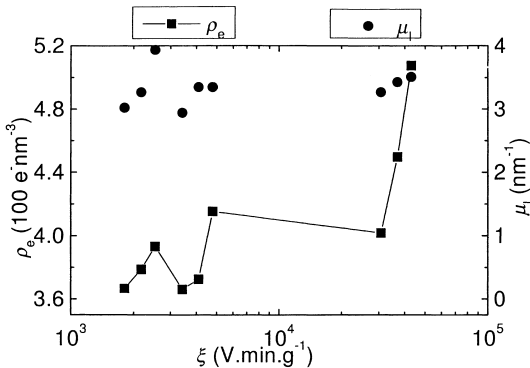


Fig. 3. Electronic density ρ_e and the linear absorption coefficient μ_l of the thin layer as a function of the plasma parameter ξ .

assumption is not justified the mass density cannot be calculated from the electronic density and the absorption coefficient using Eqs. (7)–(10). It is seen that the fits to Airy's function (Eq. (1)) are good, so the layers are homogeneous.

Fig. 3 presents the electronic density ρ_e and the linear absorption coefficient μ_l of the thin layer as a function of the plasma parameter ξ . It is seen that ρ_e is rather constant up to $\xi = 2 \times 10^4 \text{ V min g}^{-1}$, from where on it rapidly increases. The factor μ_l on the other hand slightly scatters without hardly displaying any obvious trend. There is however a subtle trend visible, for the ρ_e data as well as the μ_l data, which is worthwhile to notify. The data show for constant flow rate (M2A–M2C, M2D–M2F, M2G–M2I, see Section 2) an increase with increasing input power. This means that the radio-frequency power used in the plasma polymerization process is a more effective parameter to change the thin film internal structure than the monomer flow rate. Table 1 contains the exact values of ρ_e and μ_l , together with other fit, calculation, and experimental results.

The mass density bandwidth for each investigated sample that corresponds to the ρ_e and μ_l values in Fig. 3 is given in Fig. 4. It is assumed that c_O may vary between 0.5 and 2.0 and that x_H is in between 2.0 and 3.0. The oxygen and carbon concentrations as found from XPS are displayed as well in Fig. 4. Carbon concentration bandwidth values calculated with Eq. (10) are tabulated in Table 1. It is seen that the oxygen concentration tends to increase and the carbon concentration tends to decrease for the hardest plasma conditions (high ξ value). In the same time the mass

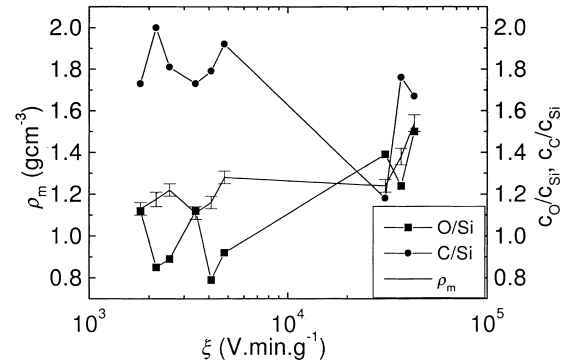


Fig. 4. Mass density bandwidth, c_O/c_{Si} , and c_C/c_{Si} concentrations as a function of the plasma parameter ξ .

density increases significantly for the two highest ξ values. This corresponds to an increased inorganic character of the thin films [9–11]. The carbon concentration remains however quite large. This is partially related to an increased carbon concentration due to air contamination at the topmost layer, partially to the presence of non-linked CH_3 and CH_2 fragments within the silica-type framework as is evidenced from XPS experiments on samples before and after Ar^+ sputtering. The mass density that is derived using the afore-mentioned assumptions has a bandwidth of about 0.06 g cm^{-3} ; the mass density calculated from Eq. (11) is in general about 0.10 g cm^{-3} higher than the upper limit in the afore-mentioned bandwidth of mass density values. This shows that the use of this formula is not justified because of the quite important hydrogen content of the thin films. The number of carbons per silicon has a bandwidth of one atom if the number of hydrogens per carbon can be rationalized. For the soft conditions the composition as deduced from the XRR results is in reasonably good agreement with the XPS results. For the hardest conditions (samples M2H and M2I) there is considerable disagreement. In order to fit the XRR data well, a rather large number of carbon atoms with at least two oxygen atoms has to be assumed. The origin of this disagreement is not very clear. The two discordant data points correspond exactly with the appearance of the non-linked CH_3 and CH_2 fragments in the structure, but it is not clear how this would alter the specularly scattered signal. It would have been possible that the interface structure for the very hard conditions was considerably changed leading to an

enhanced diffuse scattering. This was experimentally checked by performing detector and rocking curve scans around the critical angle. An enhanced diffuse scattering was, however, not observed: the diffuse scattering was estimated to be about 4% of the total signal at the second plateau of total external reflection. The data have been corrected for the angle-dependent diffuse scattering. Another possibility is that the assumption of a constant density profile across the film is no longer correct. In fact, XPS on samples produced under drastic plasma conditions before and after ionic bombardment has shown that the carbon density in the topmost layers is significantly enhanced compared to that within the bulk of the thin film. This non-constant density gradient could lead to subtle changes in the reflectivity curves, such that the use of the methods of the preceding sections are no longer valid. It is noted, however, that all curves are very well fitted using the assumption of a constant film density, but that this does not exclude that other density gradients are equally well compatible with the experimental data. A last possibility to explain the carbon content differences between the XRR and the XPS data is that the XPS investigated samples may ‘loose’ some of the carbon contamination in the topmost layers, because they are brought into ultra-high vacuum, whereas the samples for XRR are investigated under ambient conditions. Other techniques such as Rutherford backscattering may be used to quantify the chemical contents of the thin layer.

5. Conclusions

It has been shown how the mass density of thin films with partially unknown composition can be determined using high-quality XRR data. The method is principally based on the finite absorption of the X-rays inside the thin film. This absorption is enormously enhanced owing to the grazing incidence configuration of the experiment. It is noted that the present method can be used to determine with precision the composition of a thin film that contains only two elements. In this case the Kiessig fringes that give the thickness of the film must be well resolved. Otherwise the thickness must be determined by other means, e.g. ellipsometry. Conversely, the thickness of a thin film with known composition can be

determined, even if the Kiessig fringes are not visible anymore. This can be used for thickness values in between 350 and approximately 1000 nm. The aforementioned methods are best suited for thin films with a lower electronic density than that of the substrate. The organosilicon plasma polymerized thin films that were investigated in this study show a clear cross-over between an organic-like polymer at soft plasma conditions and a more silica-like framework structure deposited from a very energetic plasma.

References

- [1] A.T. Bell, Fundamentals of plasma chemistry, in: J.R. Hollan, A.T. Bell (Eds.), *Techniques and Applications of Plasma Chemistry*, Wiley, New York, 1974.
- [2] H. Yasuda, in: J. Vossen, W. Kern (Eds.), *Thin Film Processes*, New York, 1978, p. 361.
- [3] B. Chapman, *Glow Discharge Processes — Sputtering and Plasma Etching*, Wiley, New York, 1980, p. 149.
- [4] R. d'Agostino, *Plasma Deposition, Treatment, and Etching of Polymers*, Academic Press, New York, 1990.
- [5] N. Inagaki, A. Kishi, *J. Polym. Sci., Polym. Chem.* 21 (1983) 1847.
- [6] Y. Catherine, A. Zamouche, *Plasma Chem. Plasma Process.* 5 (1985) 353.
- [7] A.M. Wrobel, M.R. Wertheimer, *Plasma Deposition, Treatment, and Etching*, Academic Press, New York, 1990, p. 163.
- [8] S. Sahli, M.A. Djouadi, S. Hadj-Moussa, F. Mansour, M.S. Aida, *Mater. Chem. Phys.* 33 (1993) 106.
- [9] S. Roualdes, N. Hovnanian, A. van der Lee, R. Berjoan, J. Durand, *J. Non-cryst. Sol.* 248 (1999) 235.
- [10] S. Roualdes, A. van der Lee, R. Berjoan, J. Sanchez, J. Durand, *AIChE J.* 45 (1999) 1566.
- [11] S. Roualdes, N. Hovnanian, A. van der Lee, J. Sanchez, J. Durand, *J. Phys. IV France* 9 (1999) 1147.
- [12] X.L. Zhou, S.H. Chen, *Phys. Rep.* 257 (1995) 223.
- [13] J.R. Lu, E.M. Lee, R.K. Thomas, *Acta Cryst. A* 52 (1996) 11.
- [14] E. Chason, T.M. Mayer, *Crit. Rev. Sol. State Mat. Sci.* 22 (1997) 1.
- [15] M. Tolan, W. Press, *Z. Kristallogr* 13 (1998) 213.
- [16] M.R. Lovell, R.M. Robertson, *Curr. Opin. Colloid Interface Sci.* 4 (1999) 197.
- [17] D.L. Windt, *Comp. Phys.* 12 (1998) 360.
- [18] IMD4.1 fit program: <http://cletus.phys.columbia.edu/~windt/idl>.
- [19] M.A. Kumakhov, F.F. Komarov, *Phys. Rep.* 191 (1990) 289.
- [20] F. Bridou, *J. Phys. III France* 4 (1994) 1513.
- [21] S. Garoff, E.B. Sirota, S.K. Sinha, H.B. Stanley, *J. Chem. Phys.* 90 (1989) 7505.
- [22] S.I. Zheludeva, M.V. Kovalchuk, N.N. Novikova, A.N. Soshenov, N.E. Malysheva, N.N. Salashchenko, Yu. Ya. Platonov, A.D. Akhsakhalyan, *Cryst. Rep.* 40 (1995) 132.

Experimental feasibility of phaseless inverse scattering methods for specular reflectivity

A. van der Lee^aLaboratoire des Matériaux et Procédés Membranaires^b, 8 rue de l'École Normale, 34296 Montpellier Cedex 5, France

Received 19 May 1999

Abstract. The possibilities for calculating the X-ray or neutron scattering potential across a thin film from experimental specular reflectivity amplitude information alone and using full dynamical theory, *i.e.*, phaseless inverse scattering, are investigated and compared with traditional fitting methods. The feasibility of the method is demonstrated by one trivial and two non-trivial experimental examples. The usefulness, but also the limitations are outlined by the experiments and by numerical examples. The data reduction is treated in some detail and, in particular, a new method is proposed for deconvolving the experimental data from the instrumental smearing function.

PACS. 61.10.Kw X-ray reflectometry (surfaces, interfaces, films) – 68.35.Ct Interface structure and roughness – 68.55.Jk Structure and morphology; thickness

1 Introduction

The determination by specular neutron or X-ray reflectivity of the scattering potential (SP) $V(z)$ perpendicular to an interface has become a routine tool in surface and thin film science. Reflectivity data have been traditionally analyzed by trial-and-error and non-linear least squares fitting methods using Parrat's recursive reflectivity calculation method [1] to arrive at the final SP perpendicular to the surface. The dependency of these fitting methods on an *a priori* postulated model finds its origin in the fact that normally only the amplitudes of the reflected waves can be measured and not their phases. This is called the phase problem and has its equivalence in, *e.g.*, crystallography.

A second problem is that the SP is quite difficult to calculate from the complex reflection coefficient even if the phases were known, because of the dynamical nature of the reflectivity scattering process in the vicinity of the critical angle for total reflection. This is called the inverse scattering (IS) problem and does not have an analog in crystallography. In crystallography the Born approximation for scattering can be assumed to be valid so that the scattering density can be calculated by an inverse Fourier Transform from the complex scattering data. Both the phase problem and the IS problem are naturally circumvented if an *a priori* model is assumed that is adjusted by hand and/or by least-squares to get agreement with the experimental data. These fitting methods are, however, quite difficult to employ in the case of non-trivial

SP's, and need not give a unique solution. Hence the need arises for a more model-independent determination of the SP by specular reflectivity.

Several model-independent approaches have been proposed during the last years that aim to go beyond the Born approximation for specular reflectivity. They can be classified according to whether they are based on a fitting procedure or on an *ab initio* calculation using inverse scattering theory. Fitting procedures based on the distorted wave born approximation (DWBA) have been proposed by Sanyal *et al.* [2] and those based on an expansion of the SP in a basic set of functions by Pedersen and Hamley [3] and Berk and Majkrzak [4]. They have in common that the resulting SP need not be unique.

On the contrary, inverse scattering methods claim to solve the IS problem and to yield a unique SP at the condition that the phase is known by some means. The first proposals to measure indirectly the phase by performing one or two additional measurements on systems with magnetic reference layers were from de Haan *et al.* [5] and Majkrzak and Berk [5,6]. They have only recently found application [7,8]. Meanwhile, other methods have been proposed using non-magnetic reference layers that can also be employed in the X-ray case by either varying the wavelength across the absorption edge of one of the constituting elements [9,10] or by contrast variation using one or two different reference layers [11–13]. The contrast variation method for non-magnetic reference layers have not yet found applications.

Methods that do not use additional measurements and/or reference layers have been proposed by Klibanov and Sacks [14] and by Clinton [15]. These methods are called phaseless inverse scattering (PIS) methods, since

^a e-mail: avderlee@crit1.univ-montp2.fr^b UMR 5635 du CNRS

they calculate the SP from the experimental data without explicit phase information from elsewhere. Phase information is assumed to be implicitly present in the amplitude information and is extracted by mathematical means. The advantage of PIS methods is, of course, that the system to be studied is not disturbed by the presence of a reference layer and that the data collection can be performed, in general, in any laboratory equipped with a commercial or home-built diffractometer. Another advantage of PIS is that the mathematical data treatment is less laborious than that for two- or three measurement methods. The drawback is that some physical pre-information is required to judge the uniqueness of the result. It should be noted, however, that the methods proposed to determine the phase uniquely quite often give two alternative solutions as well, from which one has to be rejected on physical grounds as well [8, 11, 13]. A second disadvantage is that not every system is suitable for SP determination by PIS.

Although an experimental determination of the phase of the reflected waves by one of the methods mentioned before is preferable from a theoretical point of view, it is anyhow of interest to see in what circumstances PIS methods could be used to extract meaningful information from a reflectivity experiment. Clinton [15] envisioned PIS methods to play a complementary role to traditional modeling techniques, but to date it has not been shown how this is realized in practice.

The goal of this paper is to show in which experimental circumstances and for which kind of systems PIS might be useful for SP determination by specular reflectivity and to explore the experimental factors that influence the data reduction. In addition a new method is proposed for deconvolving the experimental data from the instrumental smearing function. This deconvolution method could not only be useful for phaseless inverse scattering but also for SP determination by more general inverse scattering methods using reference layers.

2 Data reduction and analysis

The PIS data reduction procedure is outlined in Figure 1 and is contrasted with the fitting methods that are either model-dependent or model-independent. The first step involves the reduction of the raw data $I(k)$, *viz.*, scaling, subtracting noise and eventual diffuse scattering, to get the (convolved) square of the reflection coefficient $r_{CV}(k)$. The intensity reduction due to geometric effects for angles below the critical angle [16] is simply ignored and all intensity data for angles below the angle at the plateau of total reflection where the intensity is maximum is set to 1.00. All subsequent data are scaled accordingly. No data smoothing is performed.

The second step involves the deconvolution of the experimental data r_{CV} . Deconvolution is not necessary if a fitting approach is used, whether it is model-dependent based on Parrat's recursive method or model-independent using a DWBA-approach or spline-functions, since then the reflectivity data are generated from the model and

subsequently convolved with the instrumental profile function IPF . The convolved data are compared with the experimental data, and the starting set of parameters is adjusted by least-squares analysis (Fig. 1b). If, however, an *ab initio* approach is sought using IS methods, deconvolution of the experimental data becomes indispensable if details in the reflectivity are smeared out by the IPF . Since the deconvolution of experimental reflectivity data is not well documented in literature, a new method is here proposed that appears to work well.

The instrumental profile function (IPF), which smears the experimental data, is determined by factors like slit width and height, beam divergence, wavelength spread and the presence of optical elements like monochromators and analyzers. The smearing operation is normally represented by the convolution integral:

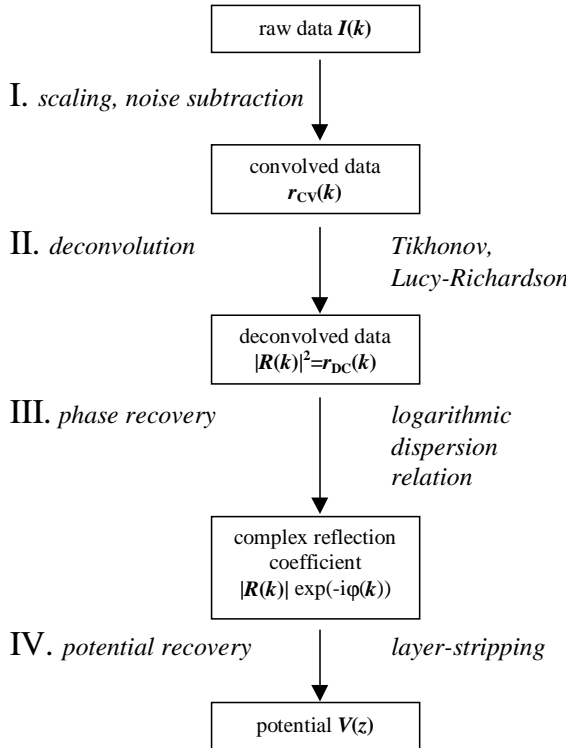
$$r_{CV}(k) = P[r_{DC}(k)] = \int_{-\infty}^{\infty} r_{DC}(k - \kappa) IPF(\kappa) d\kappa. \quad (1)$$

Here P is the convolution operator and $r_{DC}(k)$ is the non-convolved square of the reflection coefficient: $r_{DC}(k) = |R(k)|^2$. k (and κ) is the z -component of the incident wave vector: $k = 2\pi\sin\theta/\lambda$ with θ the angle between incident beam and the surface and λ the wavelength. It is noted that the momentum transfer q of the scattering process is equal to $q = 2k$. Appropriate treatments of instrumental profile functions for X-ray [16] and neutron reflectometers [17] can be found in the literature. Most often, a Gaussian smearing function is used.

Although the convolution operator P itself is straightforward to apply, the inverse operator P^{-1} is usually highly ill-conditioned [18]. Deconvolution techniques, which have a large tradition in especially astronomy, are either based on regularisation techniques that try to stabilize the inversion of large matrices, or on iterative techniques that convolve a test solution and compare it with the experimental data, then improve the test solution etc. For specular reflectivity data none of the existing methods appeared to be satisfactory alone. Instead, a combination of a technique based on zeroth-order Tikhonov regularisation [18] (TR) and the original Lucy-Richardson algorithm [19, 20] (LR) gave the best results.

First, two solutions r_{TR} and r_{LR} are calculated, based on TR and LR, respectively. The best TR-solution is selected by varying the regularisation parameter until a minimal figure of merit is found. The figure of merit is defined by $FOM = |\sum_{i=1}^{i=N/2} (r_{CV}(i) - P[r_{DC}(i)])|^2$, if N is the number of data. The LR-iteration is stopped when the relative change in the figure of merit is smaller than 10^{-4} . The sum is over the first half of the data points, because it was observed that the LR solution deteriorates at the end of the interval with increasing number of iterations. On the other hand, the TR solution appears to be very good in the second half of the interval, but not very stable for angles close to the critical angle, where the variation of the reflectivity is largest. There the calculated TR-solution $r_{TR}(i)$ quite often tends to get negative. Therefore, an optimal deconvolved $r_{DC}(i)$ is selected out

a) Model-independent calculation



b) Model-(in)dependent fitting

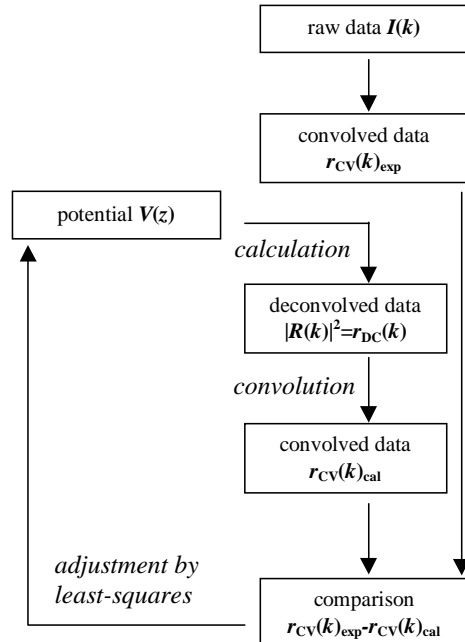


Fig. 1. Flow diagrams showing reflectivity data treatment for (a) PIS and (b) least-squares modeling.

of the TR and LR solutions $r_{TR}(i)$ and $r_{LR}(i)$, based on criteria like positiveness, smoothness and best individual figure of merit $IFOM(i) = (r(i) - P[r(i)])^2$. A solution is rejected when it is negative or when subsequent solutions $r(i)$ and $r(i + 1)$ differ by more than a factor 10. In the considered cases, subsequent data values of the theoretical non-convolved reflectivity curves never differed more than a factor 10 using reasonable (experimental) step sizes. These two criteria, the smoothness and positivity criterion were found to apply only to the TR solution. Next, the values of $IFOM_{TR}(i)$ and $IFOM_{LR}(i)$ are compared. If $IFOM_{TR}(i)$ is better, the TR-solution r_{TR} is selected; if $IFOM_{LR}(i)$ is better, the LR-solution r_{LR} is taken as the deconvolved signal r_{DC} . Finally, the complete deconvolved solution is scanned to see if there are no single or double TR-solution values within an otherwise continuous range of LR-solutions. This criterion is again based on smoothness, and has to be applied because of the non-uniqueness of the deconvolution operation P^{-1} . $IFOM_{TR}(i)$ might be smaller than $IFOM_{LR}(i)$ because of a second solution which happens to be better than the true solution, but this solution appears not to be smooth with the surrounding solutions. Such false TR-solutions are therefore interchanged by LR-solutions.

This deconvolution algorithm was tested on simulated data for two realistic cases, the first one being a 47 nm tungsten film on a Si substrate capped by a 5 nm layer Si layer with a 2 nm thick oxidized surface layer, the second one being a W/Si/W/SiO₂ multilayer with 13.0, 7.0,

13.5, and 9.0 nm thick individual layers, respectively, on a Si substrate, with 0.7, 0.7, 0.5, 0.5, and 0.5 nm as roughness parameters for the respective interfaces. It is noted that in all calculations and figures in this paper the scattering potential $V(z)$ is used, rather than the scattering length density $\rho(z)$. The relation between $V(z)$ and $\rho(z)$ is simple: $V(z) = 4\pi\rho(z)$. A Gaussian smearing function was used [16]:

$$IPF(\kappa) = \exp(-\kappa^2/2\sigma^2) \quad (2)$$

with σ equal to the half width at half maximum of the main beam. The algorithm was tested by going through the complete IS calculation (Fig. 1a).

Figure 2a shows the (neutron) reflectivity r_{CV} of the tungsten layer after convolving it with the IPF (upper curve), the original non-convolved reflectivity r_{TH} (middle curve), and the reconstructed deconvolved reflectivity r_{DC} (lower curve). The inset in the right upper corner shows that for large k -values the reconstructed curve is indistinguishable from the original curve. For k -values around the critical edge (left lower corner inset) some deviations are visible. Figure 2b shows the reconstructed (neutron) SP's from these three reflectivity curves, using the PIS method. It is seen that deconvolution is indispensable, since the reconstructed potential V_{CV} from the convolved data r_{CV} is heavily affected by the instrumental smearing. The reconstructed potential V_{DC} from the deconvolved data r_{DC} is quite close to the theoretical reconstructed potential,

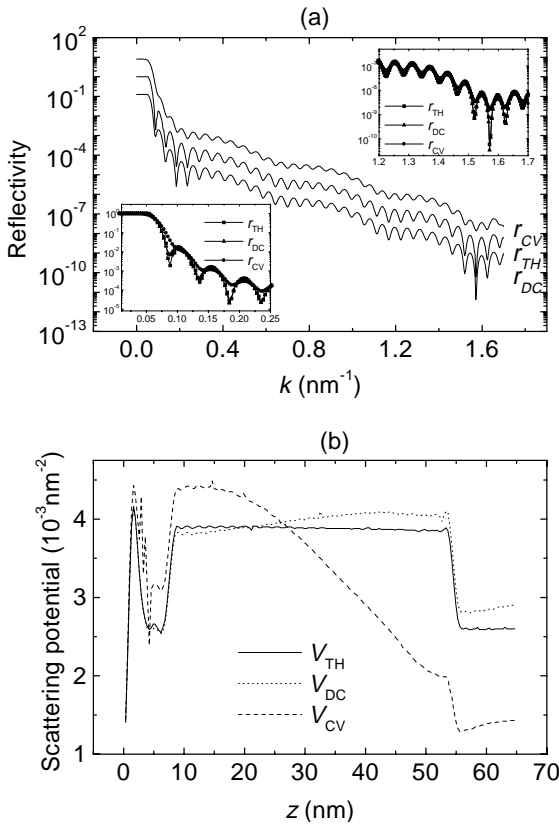


Fig. 2. (a) Calculated neutron reflectivity for a 47 nm thick tungsten layer on a silicon substrate, capped by a 5 nm thick Si layer with a 2 nm oxidized surface layer. Upper curve: convolved data; middle curve: theoretical unconvolved data; lower curve: deconvolved data. The two insets show some parts of the data interval in more detail. (b) Reconstruction of the SP using the data of (a).

except for a small deviation around the substrate/film interface. This is related to the not so perfect deconvolution around the critical edge. It is noted that the singularities of the thin film perpendicular structure, *viz.*, the jumps in the scattering potential, remain visible even after severe smearing. The thickness of the tungsten film can be determined with precision. This appears to be a generality of PIS methods for quite general SP's: the reflection amplitudes alone (without phases) contain sufficiently enough information to determine the location and amplitude of singularities in the SP [21]. This was strictly speaking only proved for unconvolved signals, but seems to apply as well to the convolved signal.

Figures 3a and 3b show the reflectivity curves and the reconstructed scattering potentials for the multilayer. Here, instrumental smearing is less severe, because of the thinner layers compared to those of the tungsten example. The reconstructed potential using the deconvolved data r_{DC} coincides nearly completely with V_{TH} , also for z -values within the substrate, since deconvolution is now fairly good in the neighborhood of the critical edge. The reconstruction itself, even the theoretical one, V_{TH} , is on the other hand less good than that of the tungsten

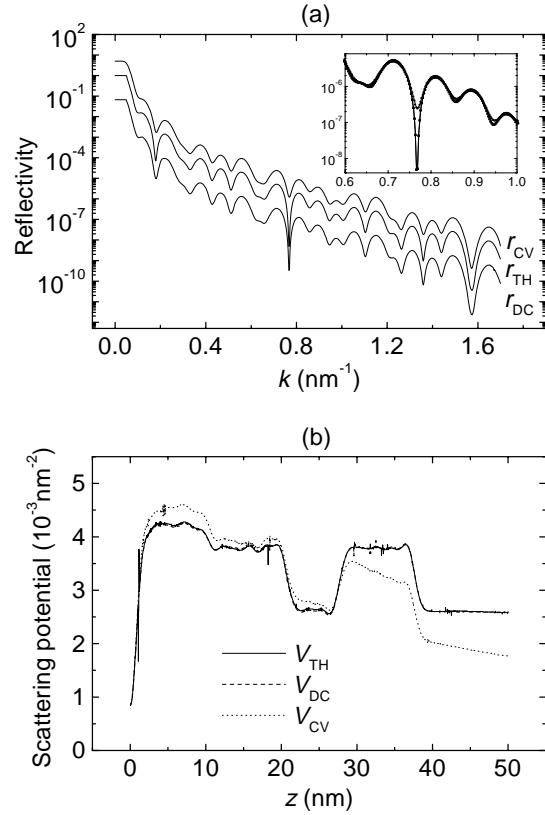


Fig. 3. (a) Calculated neutron reflectivity for a W/Si/W/SiO₂ multilayer on a silicon substrate. Upper curve: convolved data; middle curve: theoretical unconvolved data; lower curve: deconvolved data. The inset show a part of the data interval in more detail. (b) Reconstruction of the SP using the data of (a).

example, indicating that the maximum value k_{\max} have been taken too small.

The third step in the data analysis (Fig. 1a) concerns the determination of the phase $\arg(R(k))$, either by means of independent data from a second and sometimes from a third measurement, or, in certain cases, mathematically by means of a logarithmic dispersion relation. Here the form proposed by Klibanov and Sacks [14] was used:

$$\arg(R(k)) = -\pi + \frac{1}{2\pi} \int_{-1}^1 \log \left[\frac{r(k)r(1/\kappa)}{r(k+\kappa)r(1/\kappa)} \right] \frac{d\kappa}{\kappa}. \quad (3)$$

The data r are the experimental reflectivity data points r_i (if necessary desmeared) interpolated by cubic B-splines to get a quasi-continuous reflectivity function. This interpolation is necessary because the integrand of the integral in equation (3) requires data at points k_i that have not been measured. The interpolation does not give problems at the condition that the step Δk_i is not too large. This means in practice that in order to correctly describe an interference fringe Δk_i should be taken to be about one tenth of the period of the fringe. It is also advisable to take a small step in the vicinity of the critical edge, since

there the reflectivity changes drastically. The singularity of the integrand of equation (3) at $\kappa = 0$ is dealt with in the way described by Klibanov and Sacks [14]. Data required beyond the experimental cut-off are estimated by the asymptotic form $r(k) \sim (V_0/k^2)^2$, in which the constant V_0 itself is estimated from the last part of the experimental data interval. The exact value of V_0 is not very critical, at the condition that the data have been measured sufficiently far. The integration itself is performed by the extended trapezoidal rule. More sophisticated quadrature algorithms do not improve the accuracy of the final result. Results obtained by using equation (3) will be discussed further in the following section.

Finally, the SP can be calculated using the values of $|R(k)|$ and $\arg(R(k))$. Different methods have been proposed [22–24], all of which are inherently unstable for “large potentials” [25]. In this paper Sack’s layer-stripping method was used, which is believed to be more stable than the other methods [23]. The instability of this last inversion step can be considered to be the most serious obstacle for the use of IS methods in general, since it implies that SP’s of thin films larger than about 20 nm for X-rays or about 100 nm for neutrons, cannot be determined anymore, if silicon is assumed to be the substrate. These numbers depend of course on the exact scattering power of the elements that constitute the film. Some work is being performed, however, to find alternative ways to analyze the inherent instability of inverse scattering [26] based on Lyapunov exponents. This may yield new ways to shift the outset of instability to larger potentials.

3 Phaseless inverse scattering

The phase obtained by equation (3) is unique if two conditions are fulfilled. The first one supposes that the potential should have a leading jump at $z = 0$. If not, and in practical applications this is never the case due to the finite roughness of the air/film interface, the potential tends to ‘drift away’ from the $z = 0$ position. This translational invariance is not a serious problem, since the potential can easily be shifted back to the zero position, eventually by applying in a second run an appropriate phase change of the form $\exp(-ikl)$ to the obtained complex reflection coefficient, if l is the required shift of the potential. The second condition to obtain a unique phase is that the (analytically extended) complex reflection coefficient should have no zero’s in the upper half plane of the complex plane (UHP). Clinton derived several relations, using the Born approximation, for multilayers in terms of the SP’s of the constituting layers that yield those systems with a reflection coefficient without zero’s in the UHP, and that give thus a unique phase using equation (3) [15]. For real systems, however, a dynamical calculation has to be used, and then it appears that the thickness of the constituting layers and the roughness of the interfaces are intervening parameters that determine the number of zero’s.

A program was developed, using the downhill simplex method, to determine the number and position of the zeros of the complex reflection coefficient in the UHP calculated

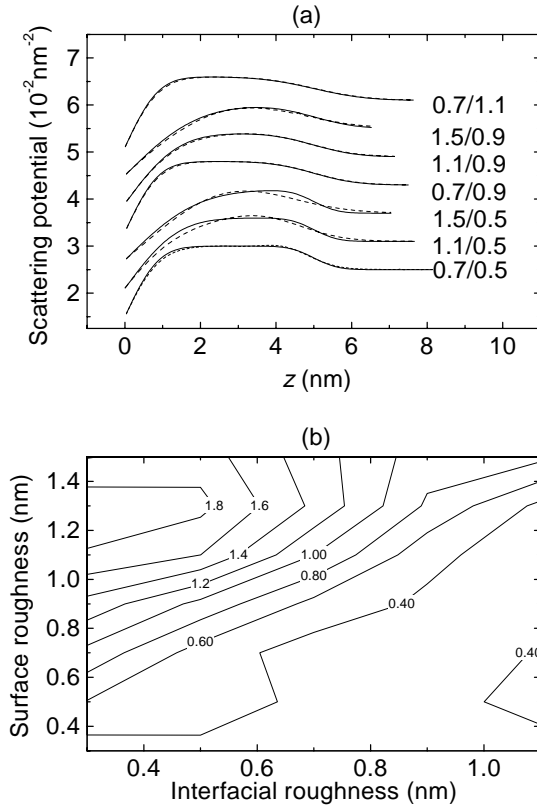


Fig. 4. (a) Reconstructions (dashed curves) of typical X-ray SP’s (full curves). The numbers shown are the values for the surface and interfacial roughness, respectively. (b) shows the relative percentual error of the reconstruction as a function of the interfacial roughness (x -axis) and the surface roughness (y -axis).

by Parrat’s recursive algorithm [1] for many different multilayer systems in the X-ray and neutron SP range. Then the SP was reconstructed using the procedures of Figure 1a to see the effects of the positions (k_x, ik_y) of the eventual zeros. The following trends were observed.

Firstly it appeared that the influence of the zero’s introduced by the presence of interfacial roughness is most often negligible, if their values are not higher than about 1.0 nm. The zero’s are normally located not too far from the real axis at values $k_x > 1.0 \text{ nm}^{-1}$ (and at $k_x < -1.0 \text{ nm}^{-1}$), well beyond the critical edge k_c . In fact, the presence of moderate interface roughness quite often helps to improve the characteristics of the potential reconstruction of for example a thin film system, compared to that of the hypothetical system without interfacial roughness. The latter systems show quite often termination ripples around the sharp edges of the potential jumps due to finite wave transfer. This is naturally absent for multilayer systems with moderate interfacial roughness. Figure 4a shows several SP reconstructions as a function of the interfacial roughness for a thin film on a substrate system. Figure 4b shows the relative percentual error of the reconstructions of 4a (and others) as a function of the surface and the interfacial roughness. The reconstruction

gets worse if either the two roughness parameters are very different and/or one of the values is larger than 1.0 nm.

The second observation is that Clinton's relation for a single layer on a substrate is in first approximation correct, but need to be adapted for the influence of the film thickness. It was found that for a single film with constant SP V_f on a substrate with constant SP V_s there are no zero's in the UHP if $V_f > V_s$, regardless the thickness d of the film. This first relation is in accord with Clinton's findings. If however $(\Delta V_f / \Delta V_s) > 1$ where ΔV_f and ΔV_s are the heights of the two steps in V , respectively, and if $V_f < V_s$, there is a critical thickness d_{crit} beyond which phaseless inversion is no longer possible: $d > d_{\text{crit}} \approx \sqrt{1/V_s}(\Delta V_f / \Delta V_s)$. This phenomenological formula does not give exactly the critical thickness beyond which zero's appear in the UHP. For SP's in the X-ray range it is quite accurate, but for SP in the neutron range the formula tends to overestimate the real critical thickness. Tests with d -values below the phenomenological critical thickness, but above the real critical thickness, thus for systems with (usually) two zero's in the UHP, showed that phaseless inversion yields a completely satisfactory result. This is because the zeros are located very close to the real axis. The zeros thus have a very small imaginary part, rendering the phase correction important only for a few data points. The phenomenological formula thus accurately estimates the possible systems for phaseless inversion for either neutrons or X-rays. It is noted that the critical thickness is generally larger for neutrons than for X-rays for the same chemical system.

Clinton also derived a relation for multilayers: the largest jump in the scattering potential must be larger than the sum of the absolute values of all other jumps in order to be able to apply phaseless inverse scattering methods. Extensive simulations using the full dynamical theory have shown that this statement is remarkably correct, except for the important addition already found for the single-layer system. This means *in concreto* that the SP of a single layer within the multi-layer system must not be less than one half of the SP of all other layers. If it is larger than one half, but smaller than the SP of another layer, then its thickness must not exceed the critical thickness given by the phenomenological formula.

4 Experimental feasibility

It is shown now how PIS methods can be used, in conjunction with traditional fitting methods, to determine a non-trivial SP compatible with the experimental data. Three cases will be presented. The first one could be considered trivial, because the SP can be found with ease using traditional fitting methods. The two other examples are less evident to analyze using Parrat's recursive relations.

The first thin film was deposited by plasma enhanced chemical vapor deposition (PECVD) from diethoxydimethylsilane (DEDMS), resulting in an amorphous layer with $\text{SiO}_x\text{C}_y\text{H}_z$ composition [27]. The second film was a nominal 10 nm thick carbon layer obtained by

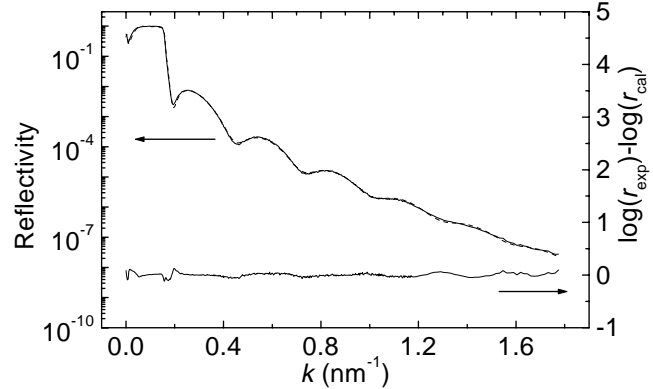


Fig. 5. Experimental X-ray reflectivity (full curve, left axis) from a DEDMS thin layer on a Si substrate and the reflectivity from the fitted single-layer model (dashed curve, left axis) and the corresponding difference curve (right axis). The parameters of the one-layer model are $\rho_{\text{layer1}} = 0.0176 \text{ nm}^{-2}$, $\rho_{\text{substrate}} = 0.0248 \text{ nm}^{-2}$, $d_{\text{layer1}} = 11.0 \text{ nm}$, $\sigma_{\text{air/layer1}} = 0.64 \text{ nm}$, $\sigma_{\text{layer1/substrate}} = 0.96 \text{ nm}$.

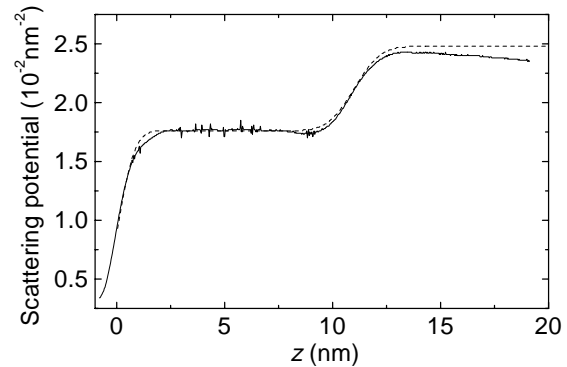


Fig. 6. SP of DEDMS film on a Si substrate determined by fitting using Parrat's scheme (dashed line), and by the PIS-method (full line).

cathodic sputtering, and the third one an approximately 14 nm thick C_4F_8 layer also obtained by PECVD from a 50%/50% $\text{C}_4\text{F}_8/\text{Ar}$ plasma. All three thin films were deposited on clean (001) Si wafer surfaces.

X-ray reflectivity data were recorded using a commercial BRUKER D5000 diffractometer equipped with a reflectivity stage and a secondary graphite monochromator. The data were collected using $\text{Cu}-L_{3,2}$ X-rays ($\lambda = 0.154051 \text{ nm}$ and $\lambda = 0.15433 \text{ nm}$, respectively) up to $k = 1.77 \text{ nm}^{-1}$, $k = 1.22 \text{ nm}^{-1}$ and $k = 2.30 \text{ nm}^{-1}$, for the DEDMS, carbon and the C_4F_8 film, respectively. Step sizes and counting times were variable, according to the intensity in a certain interval. The reflectivity intensity was recorded over 6 to 7 decades. Deconvolution of the data appeared not to be necessary, since the investigated films are rather thin.

Figure 5 presents the experimental data from the DEDMS-film along with the simulated data from a single-layer model fit using Parrat's recursive relations [1]. It is

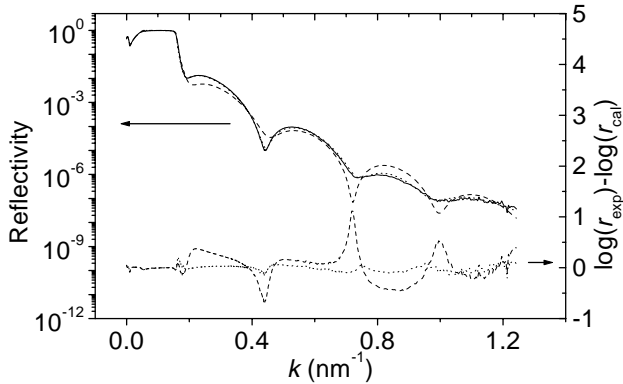


Fig. 7. Experimental X-ray reflectivity curve (full line, left axis) of a thin carbon film on a Si substrate and the difference curves (right axis) of the one-layer (dashed) and the two-layer (dotted) fit. The parameters of the one-layer model are $\rho_{\text{layer}1} = 0.0202 \text{ nm}^{-2}$, $\rho_{\text{substrate}} = 0.0248 \text{ nm}^{-2}$, $d_{\text{layer}1} = 11.2 \text{ nm}$, $\sigma_{\text{air}/\text{layer}1} = 1.37 \text{ nm}$, $\sigma_{\text{layer}1/\text{substrate}} = 0.76 \text{ nm}$. The parameters of the two-layer model are $\rho_{\text{layer}1} = 0.0229 \text{ nm}^{-2}$, $\rho_{\text{layer}2} = 0.0169 \text{ nm}^{-2}$, $\rho_{\text{substrate}} = 0.0248 \text{ nm}^{-2}$, $d_{\text{layer}1} = 7.7 \text{ nm}$, $d_{\text{layer}2} = 3.5 \text{ nm}$, $\sigma_{\text{air}/\text{layer}1} = 1.74 \text{ nm}$, $\sigma_{\text{layer}1/\text{layer}2} = 1.20 \text{ nm}$, $\sigma_{\text{layer}1/\text{substrate}} = 0.88 \text{ nm}$.

seen that the agreement between the curves is excellent, the reliability index being $R = 0.0078$. To prove that the *ab initio* determination of this trivial SP is also possible, the PIS calculations (Fig. 1a) using the experimental data were carried out. Figure 6 shows a good concordance between the PIS SP and the one-layer model from Parrat's fit. This trivial example demonstrates that PIS can be readily applied using experimental data collected with laboratory equipment. It appears that neither experimental noise, nor absorption for such a light-element system distorts the extracted PS. It is noted that the IS theory applied in this paper is intended for systems without absorption. This condition is normally fulfilled for neutron SP's, but X-ray SP's have normally an imaginary part. Finally it is verified experimentally that moderate interfacial roughness can be very well modeled.

The second example is not so trivial, in the sense that fitting using Parrat's recursive relations is not straightforward. The experimental reflectivity curve of the carbon film is shown in Figure 7 (full line). First a fit was tried using Parrat's recursive relations on the hypothesis that the layer is homogeneous (dashed line). The difference data $\log(r(k)_{\text{exp}}) - \log(r(k)_{\text{cal}})$ (lower part of Fig. 7, dashed line), on the same scale as the difference data in Figure 5 give the impression that the fit is only on the average correct. Taking into account the mean SP value resulting from the single-layer model fit, it could be anticipated that PIS methods could be useful to detect the deviations from the mean. Hence the SP was calculated following the PIS scheme of Figure 1a. Figure 8a shows the resulting SP as a dotted line. An density depleted region at the substrate/film interface results. A second fit using Parrat's scheme was tried with a two-layer model, that parametrized approximately the dotted curve of

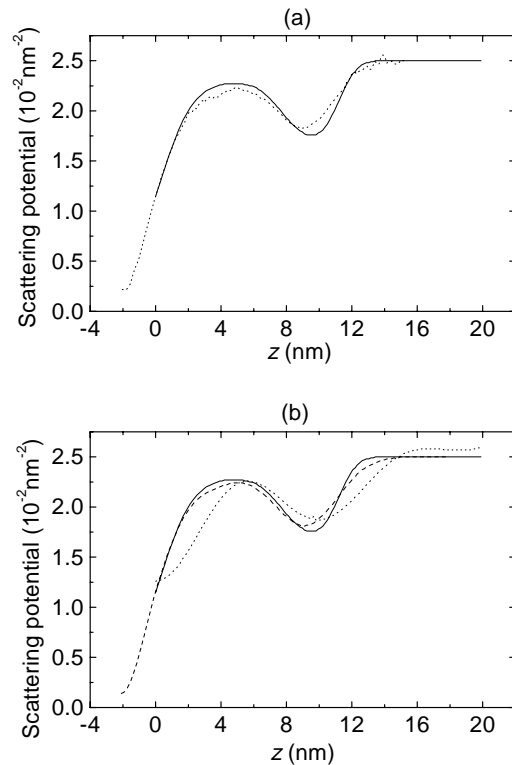


Fig. 8. (a) SP of carbon film on a Si substrate determined by fitting using Parrat's scheme (full line), and by the PIS-method (dotted line). (b) SP of carbon film determined by fitting using Parrat's scheme (full line), by the PIS-method using the complex reflection coefficient from Parrat's scheme at the experimental resolution (dashed line) and at a lower resolution $k = 0.400 \text{ nm}^{-1}$ (dotted line).

Figure 8a. The resulting difference data are given as the dotted line in the lower part of Figure 7 at the same scale as the difference data of the one-layer model. The overall reliability indices are $R = 0.0659$ and $R = 0.0133$ for the one-layer model and two-layer model, respectively. The full curve in Figure 8a represents the two-layer model.

Since it is not known whether the real unknown complex reflection coefficient has zero's in the UHP and – more important – what their eventual influence is on the PIS determined SP, some further calculations were done. The UHP zero's of the complex reflection coefficient corresponding to the final two-layer model SP were calculated. There are indeed zero's in the UHP that find their origin in the rather large interfacial roughness. The first zero has a quite low real part ($\text{Re}(k_0), \text{Im}(k_0)$) = (0.44, 0.011). The critical k_c vector of the substrate is $k_c = 0.158 \text{ nm}^{-1}$. If in turn this complex reflection coefficient is used for a PIS calculation, thus with neglecting the zero's, the dashed curve in Figure 8b results. The full curve represents again the two-layer SP that comes out of Parrat's fit; the dotted curve is the PIS SP calculated using the data at a much lower k -cutoff, *viz.*, at $k = 0.400 \text{ nm}^{-1}$, thus just below the first zero in the UHP. It is noted that the dashed curve of Figure 8b is quite close to the dotted curve of Figure 8a

and that the general features of the curve are similar to that of the full curve. In other words: the PIS SP represents the zero-order approximation to the real SP.

By calculating the PIS SP an idea has been obtained how the SP could deviate from the single-layer model. Even the low-resolution data show up the reduced density layer at the substrate/film interface. It cannot be rigorously proved that the obtained SP is unique. That is only possible by an experimental determination of the phase. The full and dashed profile in Figure 8b give the same reflectivity amplitude, because the presence of UHP-zero's does not affect the amplitude. The final SP is anyhow better compatible with the experimental data than the original one-layer model, a result which should have been obtained with less ease by trial-and-error and/or least-squares fitting.

The third example, the nominally 14 nm thick C_4F_8 film, shows less deviations from the single layer model. Figure 9 (full curve) gives the experimental data along with the reflectivity resulting from the fit using a single-layer model (dashed curve). One could content oneself with this model, but one could also look for the reasons of the significant deviations between the two curves. It is noted that these deviations are truly significant when the experimental errors from counting statistics are taken into account. This error is maximum, about 4.5%, at the end of the experimental curve in Figure 9. Since the parameters of the single-layer model are in agreement with a SP that could be extracted by PIS, such a calculation was tried, resulting in the full curve of Figure 10. The dashed line in the same figure represents the single-layer model. It is seen that the PIS SP exhibits a slight, increasing density across the film. This density gradient is quite difficult to model with a limited number of layers in Parrat's recursive calculation method. Therefore Sanyal's model-independent fitting method was tried [2], taking the single-layer model (without roughness) as the unperturbed SP in the distorted wave born approximation. The thin layer was taken to be 16 nm and divided into 24 slices of equal thickness. The 24 points from the fit are very close to the (full) curve from the PIS calculation (Fig. 10). The reflectivity using this 24-layer model is in excellent agreement with the experimental data (Fig. 9, dotted curves).

Several comments can be made in comparing the *ab initio* PIS approach and Sanyal's model-independent fitting approach. Sanyal's method was found to be quite sensitive on the thickness of the thin layer to be modeled. Moreover, it is a perturbation method for which an unperturbed system has to be presumed that originates from a model-dependent fitting method. PIS is, on the other hand, really model-independent and uses no fitting whatsoever. Sanyal's method, however, does not suffer from the instability problems for larger potentials. In addition, it is not limited to potentials that fulfill the conditions of the phenomenological formula. It is seen that the PIS SP tends to level off for large z -values. This is a sign of the outset of instability. Both methods are in conclusion very sensitive to small deviations from an otherwise constant SP.

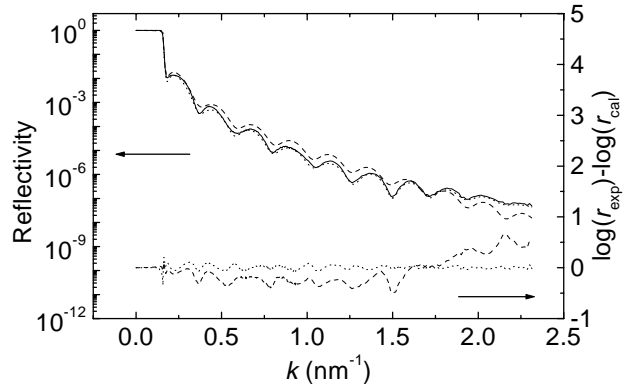


Fig. 9. Experimental reflectivity (full curve), together with their simulations calculated from the model resulting from Sanyal's fitting method (dotted) and from the one-layer model (dashed). The corresponding difference curves are shown in the lower part of the figure.

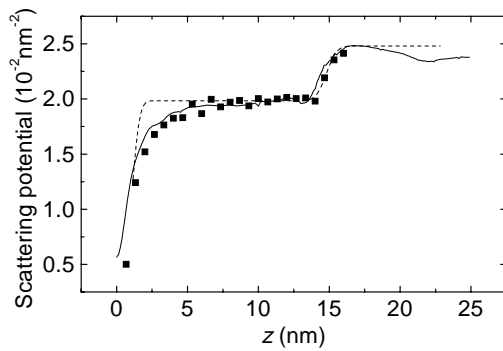


Fig. 10. SP of C_4F_8 film on a Si substrate determined by PIS (full line), by Sanyal's method (squares) and by classical fitting using Parrat's recursive relations (dashed line).

5 Concluding remarks

A new method to determine the scattering potential from specular reflectivity data using full dynamical theory, *viz.*, phaseless inverse scattering, has been tested on its experimental feasibility. The method has been previously described in literature, but has never been applied using experimental data. The phase extraction and the layer-stripping algorithms are stable against experimental noise, but fail for large potentials, even if the data are noise-free. It is shown for which systems PIS methods can extract a meaningful SP. When used with caution, PIS could provide valuable information complementary to traditional fitting methods, like those based on Parrat's recursive relations. PIS can detect deviations from multilayer-like models which are hard to find using the traditional fitting methods. PIS yields about the same information as Sanyal's method, but is intrinsically model-independent. However, the method gives, like Sanyal's and Parrat's method, rarely a unique SP, because of the lack of some fundamental *a priori* knowledge. Instead, more general IS methods have to be used to obtain a real unique SP, which

however require more laborious experiments that can quite often only be performed using a synchrotron or neutron source. Therefore, PIS could play an important role at a laboratory scale, when the possibility does not exist, for whatever reason, to perform more than one measurement or to change the system to be studied by the deposition of one or more reference layers.

S. Roualdes, D. Cot and H. Lecacheux (LMPM-Montpellier) are thanked for providing the DEDMS, carbon and C₄F₈ deposits, respectively.

References

1. L.G. Parrat, Phys. Rev. **95**, 359 (1954).
2. M.K. Sanyal, J.K. Basu, A. Datta, S. Banerjee, Europhys. Lett. **36**, 265 (1996).
3. J.S. Pedersen, I.W. Hamley, J. Appl. Cryst. **27**, 36 (1994).
4. N.F. Berk, C.F. Majkrzak, Phys. Rev. B **51**, 11296 (1995).
5. V.O. de Haan, A.A. van Well, S. Adenwalla, G.P. Felcher, Phys. Rev. B **52**, 10831 (1995).
6. C.F. Majkrzak, N.F. Berk, Phys. Rev. B **52**, 10827 (1995).
7. C.F. Majkrzak, N.F. Berk, J. Duna, S.K. Satija, A. Karim, J. Pedulla, R.D. Deslattes, Physica B (Utrecht) **241-243**, 1101 (1998).
8. A. Schreyer, C.F. Majkrzak, N.F. Berk, H. Grüll, C.C. Han, J. Chem. Phys. Sol. **60**, 1045 (1999).
9. M.K. Sanyal, S.K. Sinha, A. Gibaud, K.G. Huang, B.L. Carvalho, M. Rafailovich, J. Sokolov, X. Zhao, W. Zhao, Europhys. Lett. **21**, 691 (1993).
10. S. Banerjee, Y.J. Park, D.R. Lee, Y.H. Jeong, K.-B. Lee, S.B. Yoon, H.M. Choi, J.-C. Park, J.S. Roh, M.K. Sanyal, Appl. Surf. Sci. **136**, 41 (1998).
11. C.F. Majkrzak, N.F. Berk, Phys. Rev. B **58**, 15416 (1998).
12. T. Aktosun, P.E. Sacks, Inverse Pr. **14**, 211 (1998).
13. T. Aktosun, P.E. Sacks, Appl. Math. Rep. No. AM99-03, Iowa State University (1999).
14. M.V. Klibanov, P.E. Sacks, J. Math. Phys. **33**, 3813 (1992).
15. W.L. Clinton, Phys. Rev. B **48**, 1 (1993).
16. A. Gibaud, G. Vignaud, S.K. Sinha, Acta Cryst. A **49**, 642 (1993).
17. W. Bouwman, J.S. Pedersen, J. Appl. Cryst. **29**, 152 (1996).
18. A. Tikhonov, V. Arsenine, *Méthodes de résolution de problèmes mal posés* (MIR, Moscou, 1976).
19. W.H. Richardson, J. Opt. Soc. Am. **62**, 55 (1972).
20. L.B. Lucy, Astron. J. **79**, 745 (1974).
21. P.E. Sacks, J. Math. Phys. **38**, 3497 (1997).
22. T.M. Roberts, Physica B (Utrecht) **173**, 157 (1991).
23. P.E. Sacks, Wave Motion **18**, 21 (1993).
24. R. Lipperheide, G. Reiss, H. Leeb, H. Fiedeldey, S.A. Sofianos, Phys. Rev. B **51**, 11032 (1995).
25. H.J.S. Dorren, E.J. Muyzert, R.K. Snieder, Inverse Pr. **10**, 865 (1994).
26. H.J.S. Dorren (preprint, 1999).
27. S. Roualdes, A. van der Lee, R. Berjoan, J. Sanchez, J. Durand, AIChE J. **45**, 1566 (1999).